

Design and experimental analysis of an active and passive camber morphing system for rotor blades

Zahoor, Y.

DOI

[10.4233/uuid:4b421d5b-7e62-47dd-bb19-f3cb7c1bed5e](https://doi.org/10.4233/uuid:4b421d5b-7e62-47dd-bb19-f3cb7c1bed5e)

Publication date

2022

Document Version

Final published version

Citation (APA)

Zahoor, Y. (2022). *Design and experimental analysis of an active and passive camber morphing system for rotor blades*. [Dissertation (TU Delft), Delft University of Technology].
<https://doi.org/10.4233/uuid:4b421d5b-7e62-47dd-bb19-f3cb7c1bed5e>

Important note

To cite this publication, please use the final published version (if applicable).
Please check the document version above.

Copyright

Other than for strictly personal use, it is not permitted to download, forward or distribute the text or part of it, without the consent of the author(s) and/or copyright holder(s), unless the work is under an open content license such as Creative Commons.

Takedown policy

Please contact us and provide details if you believe this document breaches copyrights.
We will remove access to the work immediately and investigate your claim.

**DESIGN AND EXPERIMENTAL ANALYSIS OF AN
ACTIVE AND PASSIVE CAMBER MORPHING SYSTEM
FOR ROTOR BLADES**

DESIGN AND EXPERIMENTAL ANALYSIS OF AN ACTIVE AND PASSIVE CAMBER MORPHING SYSTEM FOR ROTOR BLADES

Dissertation

for the purpose of obtaining the degree of doctor
at Delft University of Technology,
by the authority of the Rector Magnificus Prof.dr.ir. T.H.J.J. van der Hagen
chair of the Board for Doctorates,
to be defended publicly on
Monday 24 January 2022 at 10:00 o'clock

by

Yasir ZAHOOR

Master of Science in Aerospace Engineering,
Delft University of Technology, the Netherlands
born in Wah Cantt, Pakistan

This dissertation has been approved by the promotor

Composition of doctoral committee:

Rector Magnificus	chairperson
Dr.ir. R. De Breuker	Delft University of Technology, promotor
Prof.dr.ir. M. Voskuijl	Faculty of Military Sciences Den Helder, copromotor
Dr. J. Sodja	Delft University of Technology, copromotor

Independent members:

Prof.dr. C. Kassapoglou	Delft University of Technology
Prof.dr.ir. C.J. Simao Ferreira	Delft University of Technology
Prof.dr. S. Ricci	Politecnico di Milano, Italy
Dr. B.K.S Woods	University of Bristol, UK
Prof.dr.ir. R. Benedictus	Delft University of Technology, reserve member



Keywords: camber morphing, passive system, active system, experimental analysis

Printed by: Ipskamp Printing

Front & Back: Designed by Muhammad Waail Asif

Copyright © 2022 by Y. Zahoor

ISBN 978-94-6421-630-1

An electronic version of this dissertation is available at
<http://repository.tudelft.nl/>.

*Dedicated to Abu, Ami, my sister Nazma,
my beloved wife Momena,
and my son Rayyan*

CONTENTS

Summary	xi
Nomenclature	xiii
1 Introduction	1
1.1 Background	2
1.2 Rotorcraft Specific Morphing Complexities	3
1.3 Research Goal and Objectives	5
1.4 Project Overview	5
1.5 Dissertation Overview	6
2 Recent Progress in active and Passive Morphing in Rotorcraft	9
2.1 Morphing Strategies	10
2.2 Active Morphing in Rotorcraft	11
2.3 Passive Morphing	15
2.4 Summary	17
3 Camber Morphing Flap Characterization	23
3.1 Design Approach	24
3.1.1 Design Considerations	25
3.2 Analysis Methodology	26
3.2.1 CFD Studies	29
3.3 Design Study of Morphing Skin	31
3.3.1 Effect of Material Thickness	32
3.3.2 Effect of Material and Layup	33
3.3.3 Effect of Trailing Edge Morphing Length	36
3.4 Summary	37
4 Active Morphing System design	41
4.1 Actuation System Requirements	42
4.2 Actuator Considerations	43
4.3 Actuator Selection	44
4.3.1 Selection Procedure for APA	46
4.4 Actuation Mechanism Design	48
4.5 Summary	50

5	Passive Morphing System Design	53
5.1	Significance of Passive Morphing	54
5.2	Design Methodology	55
5.2.1	Proposed Concept for Passive Morphing	56
5.2.2	Design Parameters	58
5.3	Mathematical Formulation	59
5.3.1	Scope and Assumptions	59
5.3.2	Elastic Load Estimation	59
	Simple Cantilever Beam Case	61
	Simplified Trailing-Edge Shape Case	62
5.3.3	Aerodynamic Load Estimation	66
5.3.4	Estimation of Geometric Parameters	68
5.3.5	Force Equilibrium	68
	Problem Setup	71
5.4	Working Principle of Passive Concept	73
5.5	Summary	75
6	Experimental Setup	79
6.1	Introduction	80
6.2	Design and Manufacturing of the Demonstrators	80
6.2.1	Design and Manufacturing of Morphing Flap	80
6.2.2	Wind Tunnel Test Demonstrator	83
6.2.3	Whirl Tower Test Demonstrators	84
	Active System Demonstrator	84
	Passive System Demonstrator	84
6.3	Test Setup and Objectives	88
6.3.1	Wind Tunnel Test	88
6.3.2	Whirl Tower Test	89
	Active System Test	90
	Passive System Test	91
6.4	Summary	92
7	Results and Validation	97
7.1	Wind Tunnel Testing	98
7.1.1	Quasi-Static Testing	98
7.1.2	Dynamic Testing	102
7.2	Active System Whirl Tower Testing	103
7.2.1	Quasi-Static Testing	105
7.2.2	Dynamic Testing	106
7.3	Passive System Whirl Tower Testing	113
7.4	Summary	121

8 Conclusions and Recommendations	123
8.1 Conclusions	124
8.1.1 Morphing Skin	125
8.1.2 Active Camber Morphing System	125
8.1.3 Passive Camber Morphing System	126
8.2 Recommendations for Future Work	127
Acknowledgements	131

SUMMARY

Modern helicopters are equipped with rotor blades with exposed linkages, swashplates, and mechanical components. While such rotor blades have proved to be highly reliable, they are the leading cause to generate noise and vibration. In addition, the drag due to exposed linkages and hinges affects the helicopter performance. To overcome these issues and improve flight quality, researchers have worked on various techniques. One promising way to mitigate noise and vibration and replace the conventional control mechanism of the rotor blade is to use a trailing edge flap. Additionally, having a morphing trailing edge flap brings the opportunity to enhance rotor performance with even better flow quality over the rotor blade surface and is potentially lightweight. Consequently, the actuation of a morphing flap at higher frequencies helps to mitigate noise and vibration. However, morphing solutions are generally hard to implement even for fixed-wing aircraft because of the conflicting requirements of flexibility, strength, and weight. For rotorcraft, the concept to the physical realization of morphing solutions is even more challenging due to the complex loading environments, smaller blade volumes, and centrifugal forces. This is the first issue that the author tries to address with the present dissertation, i.e., to design, develop and do a feasibility study of an active trailing edge camber morphing system for rotorcraft.

The second important factor related to the rotor blades considered in the present research work comes in the form of the apparent centrifugal forces, which are considerably higher as compared to the lift force on the blade. In the variable speed rotorcraft, the RPM can be varied to change the centrifugal forces. Such a capability can be utilized to deflect a trailing edge morphing flap resulting in a potential increase in the pilot control authority and a decrease in the power required. In this way, no external energy source is required to morph the trailing edge morphing flap. The second main objective of the present dissertation is to develop a novel concept that enables the trailing edge flap deflection by variations in rotor RPM within a specified range.

Keeping in view the requirements mentioned above, the research work presented in this dissertation is dedicated to design, develop, and test the active and passive morphing systems based on the camber morphing concept that utilizes conventional materials for morphing skin. The skin characterization is carried out before the design and development of the demonstrators for both the active and the passive systems. Numerical analysis with one-way fluid-structure interaction is performed to study the behaviour of the skin under realistic aerodynamic loading experienced by a rotor blade. It is shown that with an appropriate selection of material and skin thickness, a trailing edge morphing flap can be designed, especially with carbon fibre prepreg material which shows more weight savings than isotropic materials like aluminium.

In the active concept, off-the-shelf piezoelectric actuators are used to actuate the flap made out of composite material at 1/revolution till 3/revolution. The selection procedure of these actuators and the mechanical design is explained to show the working and

limitations of these actuators with respect to the active concept. Similarly, a novel passive concept is envisaged to exploit the performance benefits of variable RPM rotorcraft with a morphing flap. In this system, changes in rotor RPM change the apparent centrifugal force experienced by the blade. The flap actuation is carried out by a reduction of 10% RPM in rotor speed. To investigate the behaviour of both concepts under centrifugal load, test demonstrators are developed and experimentally analyzed in a whirl tower setup showing a promising outcome. In addition, a wind tunnel demonstrator is developed and tested to study the morphed shapes under the aerodynamic loads. This way, the presentation dissertation helps to provide both active and passive means of actuating a morphing flap which can be further enhanced and analyzed for full-scale rotor applications.

NOMENCLATURE

Abbreviations

<i>APA</i>	Amplified Piezoelectric Actuator
<i>AR</i>	Aspect Ratio
<i>BEM</i>	Blade Element Momentum
<i>BVI</i>	Blade Vortex Interaction
<i>CAD</i>	Computer-Aided Design
<i>CFD</i>	Computational Fluid Dynamics
<i>CG</i>	Center of Gravity
<i>CLT</i>	Classical Laminate Theory
<i>COR</i>	Centre of Rotation
<i>DAQ</i>	Data Acquisition
<i>DIC</i>	Digital Image Correlation
<i>DOF</i>	Degrees of Freedom
<i>DT</i>	Displacement Transducer
<i>EMC</i>	Elastomeric Matrix Composite
<i>FBD</i>	Free-Body Diagram
<i>FEA</i>	Finite Element Analysis
<i>FEM</i>	Finite Element Model
<i>FishBAC</i>	Fish Bone Active Camber
<i>FP</i>	Fixed Point
<i>FRF</i>	Frequency Response Function
<i>FSI</i>	Fluid-Structure Interaction
<i>FVM</i>	Finite Volume Method
<i>HHC</i>	Higher Harmonic Control

<i>HOPLITE</i>	Helicopter Conceptual Design and Performance Analysis Tool
<i>IBC</i>	Individual Blade Control
<i>KS</i>	Kolmogorov–Smirnov
<i>MAV</i>	Micro Air Vehicle
<i>MBB</i>	Messerschmitt-Bölkow-Blohm
<i>MFC</i>	Macro-Fiber Composite
<i>OEM</i>	Original Equipment Manufacturer
<i>PDE</i>	Python Development Environment
<i>PZT</i>	Lead Zirconate Titanate
<i>RANS</i>	Reynolds-Averaged Navier Stokes
<i>RPM</i>	Revolution per Minute
<i>SA</i>	Spallart Allmaras
<i>SABRE</i>	Shape Adaptive Blade for Rotorcraft Efficiency
<i>TRIC</i>	Translation Induced Camber Morphing
<i>TRL</i>	Technology Readiness Level
<i>UD</i>	Unidirectional
<i>VSR</i>	Variable Speed Rotor

Greek Symbols

α	Angle of attack	rad
β	Flap deflection	rad
λ	Rotor inflow ratio	–
ω	Rotor blade rotational speed	rad/sec
ρ	Air density	kgm ⁻³
θ_0	Collective rotor blade pitch angle	rad
φ	Angle of the inclined surface of the spanwise shaft	rad

Roman Symbols

C_d	2D drag coefficient	–
C_h	Hinge moment coefficient	–

C_{l_α}	Lift curve slope of the rotor blade's airfoil	–
C_l	2D lift coefficient	–
C_m	2D moment coefficient	–
CF	Centrifugal force	N
E_b	Bending modulus of elasticity of the skin	Nm^{-2}
F	Applied blocked force	N
F_{max}	Maximum blocked force	N
F_{Net}	Net force	N
F_r	Reaction force of endstop	N
F_s	Spring force	N
F_v	Vertical force of constraint	N
H	Flap Hinge Moment	Nm
I	Area moment of inertia	m^4
j	Number of coordinate points	–
K_s	Required spring stiffness	Nmm^{-1}
k_f	Correction factor	–
m	Mass experiencing CF within rotor blade	kg
pL	preload	N
R	Rotor blade radius	m
r	Distance of mass m from COR	m
RF	Reaction Force	N
s_j	Comulative sum	–
SI	Similarity index	–
V	Supplied voltage	V
v	Flow velocity	ms^{-1}
V_{max}	Maximum permissible voltage	V
X	Stroke at supplied voltage	mm
x_s	Spanwise movement of the bottom skin	mm
x_t	Chordwise movement of the bottom skin	mm
X_{max}	Maximum stroke	mm

1

INTRODUCTION

The thing is, helicopters are different from planes. An aeroplane, by its nature, wants to fly, and if not interfered with, too strongly, by unusual events or by a deliberately incompetent pilot, it will fly. A helicopter does not want to fly. It is maintained in the air by a variety of forces and controls working in opposition to each other, and if there is any disturbance in this delicate balance, the helicopter stops flying; immediately and disastrously. There is no such thing as a gliding helicopter.

Harry Reasoner

1.1. BACKGROUND

Morphing is a term that has stemmed from the Greek word Metamorphosis, which means to change form/shape or simply transformation. Keeping an aircraft in perspective, this definition of morphing principally stays the same. Consequently, the shape changes are primarily associated with the wing of an aircraft or the blade of a rotorcraft. The idea of a "smooth" shape change arises from the much-needed requirement of drag reduction and improved flow quality, leading to performance benefits. Secondly, aircraft are generally designed with reference to a single condition (the design point), individuated as the best match among all the possible missions it is envisaged to run [1]. The potential disadvantage of the so-called compromised design point can be negated by having adaptive wings. A classic example of such wings is the F-111 Mission Adaptive Wings (MAW), which proposed the use of adaptive leading and trailing edge surfaces to provide ideal wing shapes for selected flight conditions. Therefore, a wing that morphs has the potential of increasing the efficiency and maneuverability of an aircraft [2]. However, morphing can also introduce benefits that are rotorcraft specific, including primary flight control and mitigating noise and vibration [3–5]. In addition, centrifugal force operated morphing concepts have also been explored in the past that are only possible in rotorcraft [6].

Considering the potential benefits mentioned in the preceding paragraph, morphing still remains far from mainstream aviation. This is because the design of a morphing wing has to address conflicting requirements. On one hand, the wing structure needs to be compliant to allow configuration changes. On the other hand, it has to be sufficiently rigid to limit aeroelastic instabilities and carry the loads. These contradictory requirements, along with the weight considerations, become the critical design inputs, as represented by Campanile [7] in Fig. 1.1. The weight factor is important as in the case of F-111, the mechanical design resulted in severe weight penalties and increase of the overall system complexity which almost completely negated the attained aerodynamic benefits [1]. The need to fulfill conflicting requirements urged the researchers to explore novel materials for skins and unconventional actuation techniques, giving rise to several new morphing-based concepts [2].

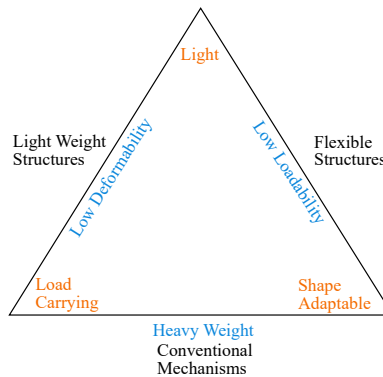


Figure 1.1: Morphing requirements [7].

In aeronautics, designing a morphing solution and implementing it in a wing structure is requirement-driven. These requirements are specific to a particular type of aircraft or rotorcraft and enforce necessary changes in one or more of the following components associated with the wing/blade [1].

- a. Structural skeleton.
- b. Actuator system.
- c. Skin.
- d. Sensor system.
- e. Control system.

While keeping the above-referred components in mind, it is also important to consider the number of changes associated with a specific morphing concept along with the level of complexities involved in its realization. Each morphing concept comes with its own set of performance benefits and limitations. Nevertheless, in the author's opinion, effective morphing solutions can be investigated, which are requirement-specific and mission-driven and do not necessarily rely on smart materials and unorthodox actuation systems. The author believes that the conventional materials, structures, and actuators can still be used to introduce smooth shape changes in the wing of an aircraft or blade of a rotorcraft by careful considerations of requirements, design parameters, and desired objectives. This way, a relatively less complex solution offering the morphing benefits can be realized.

1.2. ROTORCRAFT SPECIFIC MORPHING COMPLEXITIES

While considering morphing solutions for rotorcraft, there are additional challenges involved, which can be observed in Fig. 1.2. Even in the case of hover, different rotor blade sections encounter different flow conditions, including Mach number, flow velocity, Reynold's number, and angle of attack. This results in a linear variation of Mach numbers over the rotor radius as shown in Fig. 1.2 (a). In the case of the forward flight, the aerodynamic environment becomes even more complicated, and the Mach number at the blade sections also becomes a function of forward flight speed and blade azimuth position as shown in Fig. 1.2 (b). Besides, the flow velocities also depend on the inflow through the rotor disk and the flapping motion of the rotor blades in forward flight. Therefore, the distribution of the angle of attack over the rotor disk and associated blade loading is even more complex. Consequently, the morphing challenges are often more demanding for a rotorcraft than for a fixed-wing aircraft.

There are two additional factors that make morphing prospects even more difficult for rotorcraft. The first one is the presence of large centrifugal forces. Rotor blades are subjected to centrifugal forces that are an order of magnitude higher than the aerodynamic forces. A morphing system should therefore be designed keeping in view the effect of these forces. The second factor is the space constraint. Since rotor blades are mostly slender, the limitations of volume further reduce the choice of morphing solutions.

Due to the additional challenges particular to rotorcraft, the design, physical realization, and testing of a morphing concept have remained limited as compared to fixed-wing aircraft [8]. This can be visualized by looking at the number of concepts developed

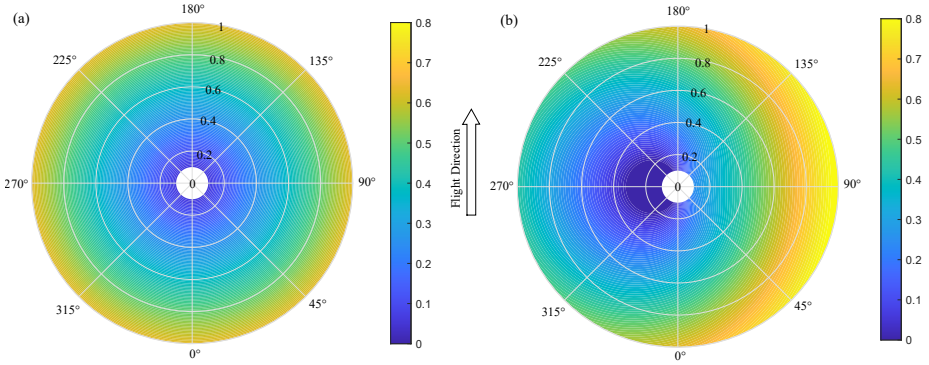


Figure 1.2: Mach number distribution over rotor disk for a tip speed of 218 m/s, $\omega = 44.4$ rad/sec, $R = 4.9$ m.

and those that matured to a level of prototyping and wind tunnel testing. Furthermore, the number of concepts that were flight tested on a flying testbed (FTB) either as a scaled model or full-scale model is very limited. Figure 1.3 shows the data [8] for both fixed-wing and rotary-wing aircraft. It indicates that, although researchers have worked on numerous concepts, yet many of those did not make it to the testing phase. The concept development and subsequent testing are even lower for rotorcraft owing to the additional complexities as discussed earlier. It is pertinent to mention that for rotorcraft, the concepts linked to FTB mainly included twist and camber morphing.

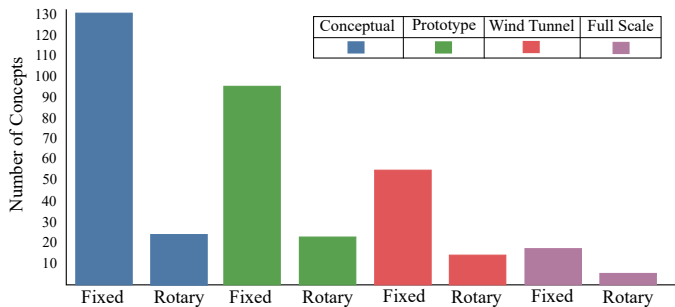


Figure 1.3: Development overview of morphing concepts [8].

Considering the additional complexities in rotorcraft, it is even more important to look at the morphing solutions that utilize existing structures and materials from a morphing perspective. This can introduce morphing benefits to a rotorcraft without bringing the unknowns of novel materials and components to the design process. It is not only because of the challenges associated with the design of such materials but also since extensive material, and structural testing (keeping in view the airworthiness regulations [9]) generally takes considerable time and resources. On the other hand, the research to design a morphing system in the conventional domain can lead to a practical solution with a significant reduction in an otherwise longer development time.

1.3. RESEARCH GOAL AND OBJECTIVES

In a review of morphing aircraft, it is highlighted that camber morphing has remained the most popular choice for morphing in rotorcraft [8]. In the author's opinion, camber morphing is a technique that gives the opportunity of not only smooth aerodynamic flow but also makes primary control and noise and vibration mitigation possible in a rotorcraft. In this way, the scope of morphing solutions is broadened, and so is the extent of the potential advantages. Due to this reason, the present research aims to design and explore the feasibility of a camber morphing flap for rotorcraft. The design process looks at the possibilities of morphing the trailing edge flap with active means. Moreover, ideas to morph the flap passively by using centrifugal force are also explored. However, the aim of research extends beyond the design process and also focuses on the feasibility study of the overall morphing system(s) by developing and testing specific demonstrators. The approach adopted for the feasibility study stems from a typical qualification cycle for rotor flaps. This qualification cycle mainly consists of the development of a preliminary design followed by the separate elementary wind tunnel [10] and whirl tower prototypes [11]. The two test campaigns give essential information regarding design improvements that lead to the design and development of a (common) Mach-scaled model for wind tunnel and whirl tower tests [12, 13]. The resulting data helps in further improvements and eventually paves the way for full-scale rotor design and test. Keeping this process in perspective, the present research work is dedicated to the preliminary phase and intends to design, develop and explore the feasibility of the elementary models.

In this context, the main research question that needs to be answered in the present thesis is as follows:

How can an active and passive morphing system be envisaged with a camber morphing technique for rotorcraft blades?

The main question gives rise to the following key sub-questions:

1. What are the design considerations and requirements for developing a morphing flap and the requisite actuation system?
2. How can the feasibility study of active and passive morphing systems be carried out to show the potential of both systems for rotorcraft?

1.4. PROJECT OVERVIEW

The research work related to the active morphing system presented in this dissertation is a part of the European Union project Shape Adaptive Blade for Rotorcraft Efficiency (SABRE) under Horizon2020 ¹. The project work involved working on the camber morphing concept by taking the Messerschmitt-Bölkow-Blohm (MBB) Bo105 helicopter as the baseline rotor. At first, surrogate models are developed indicating the potential gain in aerodynamic efficiency of the concept by using low fidelity tools like *JavaFoil*². Later, high fidelity simulations using *Ansys Fluent*³ are performed to generate the refined surrogate models. Afterwards, the design, fabrication, and testing of the wind tunnel and

¹<https://sabreproject.eu/>

²<https://www.mh-aerotoools.de/airfoils/javafoil.html>

³<https://www.ansys.com/products/fluids/ansys-fluent>

whirl tower demonstrator are carried out. The project deliverable also included reports containing the requisite analysis performed throughout the design and development process. It must be noted that the Bo105 helicopter is taken as the baseline case for the studies during the project as decided by the project consortium. The same has been considered as the baseline case in the dissertation where required.

1.5. DISSERTATION OVERVIEW

The outline of the thesis is shown in Fig.1.4. After discussing state of the art, Chap. 3 to 5 describe the design and analysis of the active and passive camber morphing systems. Whereas, Chap. 6 and Chap. 7 discuss the test setup and the experimental investigation of each concept.

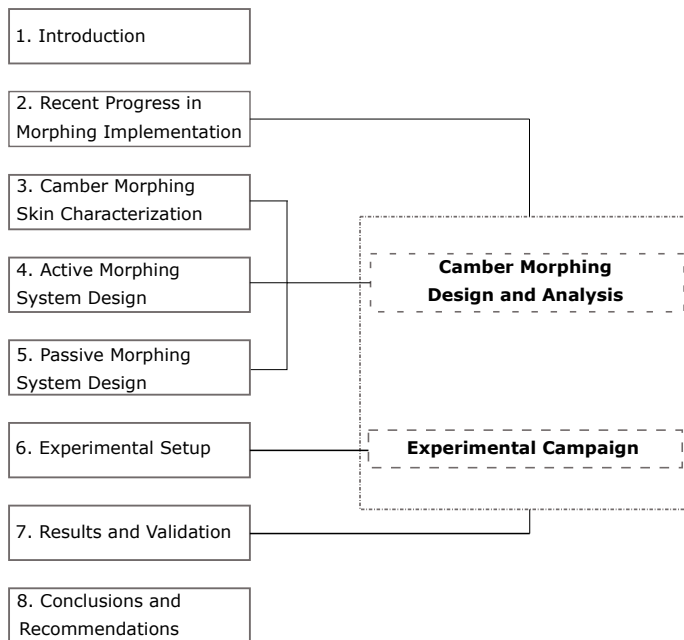


Figure 1.4: Dissertation outline.

Referring to the outline in Fig.1.4, Chap. 2 discusses the recent progress in the morphing domain, particularly for rotorcraft. Chapter 3 explains the design considerations of morphing skin and its characterization, which is common to both the active and passive concepts. Chapter 4 discusses the actuation system for the active morphing concept for rotorcraft. Similarly, Chap. 5 investigates the possibility of the design of a passive actuation system and discusses its benefits, design process, and implementation. Chapter 6 presents the experimental campaign with the details of the test setups, manufacturing, and integration of the demonstrators. Chapter 7 presents the results of the test

campaign and presents a correlation with the numerical and analytical work presented in the earlier chapters. The final chapter provides the conclusions and recommendations based on the design and experimental work for the active and passive morphing concepts built for rotorcraft.

BIBLIOGRAPHY

- [1] G. Amendola, I. Dimino, A. Concilio, R. Pecora, F. Amoroso, and M. Arena, *Morphing Aileron*. Elsevier Ltd., 2017, pp. 547–582, ISBN: 9780081009697.
- [2] C. Thill, J. Etches, I. Bond, K. Potter, and P. Weaver, “Morphing skins,” *Aeronautical Journal*, vol. 112, pp. 117–139, 2008, ISSN: 00019240.
- [3] P. P. Friedmann and T. A. Millott, “Vibration reduction in rotorcraft using active control - A comparison of various approaches,” *Journal of Guidance, Control, and Dynamics*, vol. 18, pp. 664–673, 1995, ISSN: 0731-5090.
- [4] E. Garcia, “Smart structures and actuators: past, present, and future,” pp. 1–12, 2002.
- [5] R. P. Thornburgh, A. R. Kreshock, M. L. Wilbur, and M. K. Sekula, “Continuous Trailing-Edge Flaps for Primary Flight Control of a Helicopter Main Rotor,” *AHS 70th Annual Forum*, 2014, ISSN: 15522938.
- [6] M. Khoshlahjeh and F. Gandhi, “Extendable chord rotors for helicopter envelope expansion and performance improvement,” *Journal of the American Helicopter Society*, vol. 59, pp. 1–10, 2014, ISSN: 00028711.
- [7] L. F. Campanile, “Initial thoughts on weight penalty effects in shape-adaptable systems,” *Journal of Intelligent Material Systems and Structures*, vol. 16, pp. 47–56, 2005, ISSN: 1045389X.
- [8] S. Barbarino, O. Bilgen, R. M. Ajaj, M. I. Friswell, and D. J. Inman, “A review of morphing aircraft,” *Journal of Intelligent Material Systems and Structures*, vol. 22, pp. 823–877, 2011, ISSN: 1045389X.
- [9] F. D. Florio, *Airworthiness: An Introduction to Aircraft Certification and Operations*. Elsevier Ltd., 2016, ISBN: 9780081009406.
- [10] P. Crozier, P. Leconte, Y. Delrieux, B. Gimonet, A. Le Pape, and H. M. Des Rochettes, “Wind-tunnel tests of a helicopter rotor with active flaps,” *National Aerospace Laboratory NLR - 32nd European Rotorcraft Forum, ERF 2006*, vol. 1, pp. 235–250, 2007.
- [11] P. Leconte and H. Mercier, “Experimental Assessment of an Active Flap Device,” 2002.
- [12] S. R. Hall and E. F. Prechtel, “Preliminary testing of a Mach-scaled active rotor blade with a trailing-edge servo flap,” *Smart Structures and Materials 1999: Smart Structures and Integrated Systems*, vol. 3668, pp. 14–21, 1999.
- [13] N. A. Koratkar and I. Chopra, “Wind tunnel testing of a smart rotor model with trailing-edge flaps,” *Journal of the American Helicopter Society*, vol. 47, pp. 263–272, 2002, ISSN: 00028711.

2

RECENT PROGRESS IN ACTIVE AND PASSIVE MORPHING IN ROTORCRAFT

If I have seen further, it is by standing upon the shoulders of giants.

Sir Isaac Newton

To clearly understand the research gaps and the aims presented in 1, it is important to have an overview of the progress in morphing implementations on rotor blades. This chapter discusses the literature related to the significance of trailing edge flaps, camber morphing strategies, and morphing concepts built specifically for rotor blades. It also signifies the importance of the variable speed rotor (VSR), which has played a pivotal role in any passive morphing concept, as indicated by earlier studies.

The research work in this thesis deals with active and passive morphing. Therefore, Sec. 2.1 introduces the two strategies and their significance. Section 2.2 explains the progress in active morphing and, more specifically, talks about trailing edge camber morphing, which is the focus of the present work. The next section describes the previous research work related to passive morphing techniques. Section 2.3 also discusses the fundamentals behind the VSR and the associated advantages by considering the progress in this domain. This discussion is important since the passive concepts are generally linked to the changes in centrifugal forces through rotor RPM (Revolution per Minute) changes.

2.1. MORPHING STRATEGIES

Morphing capability in an aircraft can be achieved by active and passive means. However, most of the work in the morphing domain is based on active morphing systems [1]. An active system works by using specific actuators for controlling the behaviour of the morphing mechanism. In such cases, both the input and output are continuously monitored and controlled through a feedback system [2]. Being able to work in a closed-loop system, the active system can give an optimized performance. However, the complexities due to the added mass can introduce destabilization. On the other hand, a passive system requires no additional onboard energy source for actuation. It relies solely on either the aerodynamic loads, temperature, or centrifugal forces (in rotorcraft) to change the shape of the wing while maintaining sufficient stiffness. Due to this reason, passive systems are generally lighter and are inherently stable but provide less optimized performance. The advantage of such a passive system lies in the fact that the required shape changes are introduced without any additional feedback-driven actuation mechanism. However, active morphing potentially requires sophisticated onboard signal processing, multivariable, large dimensional controllers, rapid continuous actuation mechanisms, as well as computational power [2].

While implementing a morphing scheme, some concepts require sufficient space and design changes for the idea to work. One such example is the use of telescopic wing, which potentially increases the lift to drag ratio by 9-10% [3]. However, as noted by the authors, the overall performance benefits are reduced due to the drag penalty imposed by the seams of the wing sections. On the other hand, when the modifications are limited to only those sections where the high lift system is located, the necessity of a design change is limited, and the performance benefits are enhanced [4]. In other words, by incorporating design changes in the leading edge and trailing edge section, major modifications in wings may be avoided, reducing the overall development time significantly. Regarding the scale of modifications, Szorduch has shown for the fixed-wing aircraft that camber modifications may require minimal changes [5]. At the same time, such modifications result in an increase in the lift to drag ratio by 2% and also a reduction in root

bending moment by 2%. Monner et al. showed that the chordwise camber variation leads to an improvement in operational flexibility and performance and reported lift to drag increase of 3-9% [4]. In a similar work, for helicopters, Garcia et al. have shown a reduction in the cockpit vibrations by 80-90% and 5-10% dB reduction in Blade Vortex Interaction (BVI) noise by using trailing edge flap [6]. In the fish bone active camber (FishBAC) concept proposed by Woods et al., the authors show that over the range of angles of attack typically used in fixed and rotary wing applications, improvements in aerodynamic efficiency of approximately 25% are realized [7].

It must be noted that irrespective of the type of aircraft, the biggest current design problem seems to be to combine properties like flexibility and stiffness into one structure. Due to this reason, the technology readiness level (TRL) of morphing skins is generally low [8].

2.2. ACTIVE MORPHING IN ROTORCRAFT

In rotorcraft, swashplates are generally used for rotor primary flight control and have proved to be highly reliable. However, this traditional arrangement of rotor primary flight control adversely affects the performance of the rotorcraft. This is because these swashplates are mechanically complex, have numerous exposed linkages, bearings and hinges, which contribute to helicopter aerodynamic drag and weight [9]. This problem can be resolved by incorporating the control mechanisms embedded in the rotor blades making it an active area of research. However, for rotor primary flight control, much larger lift changes can be realized by rotating the whole rotor blade than by a deflection of a flap on a section of the rotor blade. To address the potential issue, Shen et al., at the University of Maryland, USA, reported a concept to use the rotor flap for its ability to create a pitch moment instead of a lift force [10]. The authors make use of a torsion spring at the blade root. Hence, a moment created by the flap makes the blade rotate, and as a consequence of the rotation, additional lift is created. To make it even more effective, the authors apply an “index angle”, which effectively pre-stresses the torsion spring at the blade root. In this way, the required trailing edge flap angles are found to be moderate, making the flaps potentially capable of performing both primary flight control and active vibration control functions [10].

Another area of interest in the rotorcraft community is the reduction in noise and vibration of rotorcraft to improve the overall performance. Both noise and vibration are associated with the main rotor, tail rotor, and engines, with the main rotor being the primary source, especially in forward flight [11]. A contributing factor to the noise is the BVI. BVI arises from the interaction of the rotor blade with the tip vortices generated by previous rotor blade passages that create an unstable aerodynamic load and leads to undesirable noise effects and fatigue in the rotor blade structure [12]. To overcome the issue of noise and vibration in the main rotor, two approaches are common, i.e., Higher Harmonic Control (HHC) and Individual Blade Control (IBC). HHC is based on actuators located below the swashplate, thus limiting mechanically the applicable control frequencies in the rotating frame for rotors with more than three blades due to the three swashplate control degrees of freedom, one collective and two cyclic as shown in Fig. 2.1. On the other hand, IBC is based on actuators in the rotating frame and thus overcomes the limits inherent to HHC [13]. HHC systems are realized by using an addi-

tional mechanical system of pushrods connected to a conventional swashplate causing additional tilt of its plane with higher frequencies [14]. In the case of an IBC system, each blade is controlled individually by pitch-link actuators or servo-flaps [15]. It has been shown that using IBC, simultaneous control of both noise and vibration may be achieved [16, 17]. Such a concept was also flight tested in the BK117 S7045 experimental helicopter, equipped with an active blade system based on piezoelectrically driven trailing edge flaps [17].

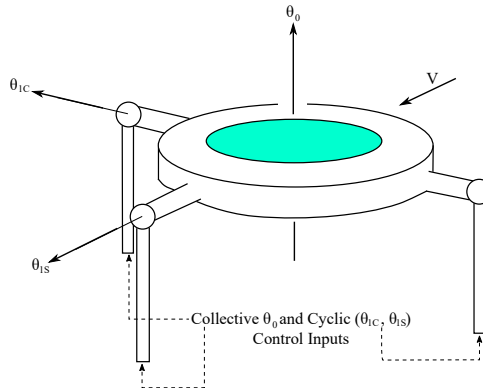


Figure 2.1: Schematic of swashplate actuation [18].

In terms of the actuation scheme, two different techniques have been proposed in the literature. The first technique uses active materials directly bonded or embedded in a rotor blade to twist the entire lifting surface [19]. The second technique based on rotating frame actuators uses discrete actuators fixed within the contour of the rotor blade to control a trailing edge servo flap [20]. In addition, some researchers also looked at other possibilities like airfoils with a Gurney flap showing better aerodynamic performance at the lower stall conditions [21]. However, in the case of airfoil camber variation, the trailing edge morphing concept is generally preferred. This is because it offers advantages of a possible modular design, simplified maintenance, and the fact that the actuator may be easily detached from the host blade structure for replacement [19].

TRAILING EDGE CAMBER MORPHING

Trailing edge camber morphing can be traditionally linked to the servo flap in rotorcraft. The earliest example of a servo flap appeared during the early 1920s when Louis Brennan worked on a helicopter concept that had an unusually large single two-bladed rotor equipped with servo-flaps for control [22]. In 1930, Corradino d'Ascanio of Italy built a helicopter with servo tabs shown in Fig. 2.2. D'Ascanio designed these servo-tabs so that they could be deflected cyclically by a system of cables and pulleys, thereby cyclically changing the lift on the blade as it swept around the rotor disk [22].

Later in the 1940s, Charles Kaman (Kaman Helicopters) adopted D'Ascanio's concept and designed a helicopter with servo-flaps [23]. When these flaps were deflected cyclically, the aerodynamic moments caused the blades to twist, changing their angle of attack and thus introducing a cyclic rotor control capability [22]. This servo-flap shown



Figure 2.2: Corradino d'Ascanio's helicopter with servo tabs.

in Fig. 2.3 is considered a trademark of the Kaman Helicopters to date.



Figure 2.3: Flap used in Kaman helicopters.

The trailing edge camber morphing idea stems from the concept of a plain servo flap. Unlike traditional hinged flaps that are externally mounted aft of the blade's trailing edge, plain flaps eliminate the hinge gap and flap support structure. This brings advantages of reduced power losses due to aerodynamic drag and improved flap effectiveness. For rotorcraft, trailing edge camber morphing provides an opportunity to improve these plain flaps by eliminating the hinge and exposing a smooth surface [24].

While designing a trailing edge morphing system, the frequency of morphing actuation is highly dependent on the desired goal. For instance, the performance and power benefits are achieved from quasi-static to 2/rev inputs [25], vibration reduction from 3/rev to 5/rev for a four-bladed rotor [26], and noise mitigation from considerably higher frequencies [27]. Active vibration control can be achieved by changing the aerodynamic loads on the airfoil through high-frequency changes in camber [28].

The use of a trailing edge flap for primary flight control is attractive in the context of an actively controlled rotor, where the embedded flaps can perform multiple functions [10]. In this context, Shen et al, developed a comprehensive rotorcraft analysis for a swashplateless rotor with trailing edge flaps and evaluated the actuation requirements of a primary control system. The results show that the swashplateless rotor trims successfully with the trailing edge flap control system in the complete range of advance ratios [29]. Similarly, Yang. et al. present analysis of a swashplateless electrically controlled rotor, where the primary flight control can be provided by applying blade pitch inputs via an integrated active trailing edge flap [30]. The authors show that it is possible

to achieve theoretically about 3% power reduction using the closed-loop active control method. However, the authors do not explicitly talk about achieving the desired control power and mention the work carried out at the University of Maryland discussed earlier [29].

2

It is also important to emphasize here that trailing edge flaps are also popular in the wind turbine community. Lachenal et al. carried out a review of the morphing concepts and materials for wind turbines and show that the researchers in the wind turbine community consider trailing edge flaps as a feasible option. This is because the trailing edge flaps have shown to potentially increase the aerodynamic efficiency (up to 15% in rotorcraft), simple construction, and low weight [31]. Similarly, a method based on beam element momentum theory (BEM) predicts a 10% increase in power coefficient of the wind turbine by using trailing edge camber morphing [32].

For the camber morphing system, the actuation scheme can be implemented in various ways. The most popular choices for rotorcraft have remained to be conventional means or piezoelectric actuation and have shown to be quite promising. However, in most cases, the overall morphing system has turned out to be quite complex. This complexity is either embedded in the fabrication of the morphing skin or in the actuation scheme itself. For example, Ben-Zeev et al. used bimorph elements consisting of isotropic piezoceramic (PZT) sheets that are diametrically bonded to a very thin brass shim with an electrically conductive adhesive coating. When it is cantilevered at one end, and equal but opposite fields are applied to each sheet, a pure bending of the bimorph occurs. The resulting tip displacement provides the actuation mechanism for the flap [33]. In another concept, a morphing cross-section for a helicopter rotor-blade is realized by a multi-morph bender including piezoelectric ceramics, glass fiber reinforced plastics, and further materials [11]. The continuous trailing edge flap is also studied using an optimized bimorph design with Macro-Fiber Composite (MFC) actuators [34]. Gandhi et al. proposed a design consisting of several compliant mechanisms of predetermined topology that are placed serially within the airfoil along the chord, aft of the leading-edge spar [35]. The actuation is achieved by piezoelectric actuators. In the conventional domain, the FishBAC concept proposed by Woods et al. [7] consists of a thin chordwise bending beam spine with stringers branching off to connect it to a pre-tensioned Elastomeric Matrix Composite (EMC) skin surface. Servo actuators are used to drive the tendon spooling pulleys in the FishBAC concept.

Although envisaged for fixed-wing aircraft, a concept that shows great potential is introduced by Vos et al. [36]. This concept works by having a discontinuity in the wing cross-section and relies on warping deformation of the wing skin, which is split at the trailing edge to create an open-section airfoil. The resulting geometry has reduced torsional stiffness due to the cut but retains its original torsional stiffness when the cut is closed by an appropriate actuation mechanism. Later, Werter et al. [37] investigated an extension of this principle to the leading edge and trailing edge morphing devices mounted on a typical wing-box structure for a fixed-wing aircraft. In this case, the actuation is introduced by the servo motors in the chordwise direction through the appropriate translation of the bottom skin; thus, the concept is called Translation Induced Camber (TRIC). Figure 2.4 shows an illustration of the mechanism based on the TRIC concept, inside the leading edge and the trailing edge sections of the wing structure [38].

The design and feasibility study of such a concept for rotorcraft can certainly prove to be beneficial.

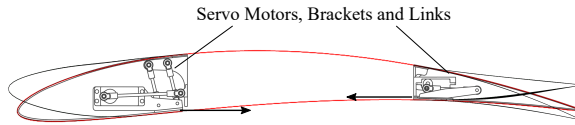


Figure 2.4: Mechanism inside the wing structure showing the full range of deformation [38].

2.3. PASSIVE MORPHING

The idea of passive morphing arises from the need to utilize the tremendous amount of centrifugal force generated in a rotorcraft, which can range from 6 to 12 tons at the blade root of two to four passenger helicopters and up to 40 tons for larger helicopters [39]. This centrifugal force may be utilized in actuating a flap that otherwise needs an active system for the same purpose. If the advantages of having a passively morphing flap are established in the flight operation of a rotorcraft, devising and testing a passively morphing system can prove beneficial. However, such a passive morphing system must have proper means to control the flap deployment.

In helicopters, passive morphing has been studied mainly to utilize large centrifugal force for chord and span morphing. In these concepts, the change in shape is achieved by changing the centrifugal force by varying the RPM of the rotor. For instance, a chord morphing system based on the cellular structure is designed and tested [40] that shows its significance for stall alleviation [41]. Similarly, another concept for chord morphing utilizes centrifugally operated Von Mises Truss to achieve the desired objectives of main rotor power reductions of up to nearly 17% [42]. In a similar work for span morphing, a proof-of-concept demonstration rotor is designed, fabricated, and tested on a hover stand [43]. This concept relies on a spring-based mechanism that works through the changes in the RPM and shows power reductions of around 10% when compared to its baseline configuration.

It is clear from the above-referred concepts that the change in centrifugal force is brought about by the change in RPM, which is a feature of VSR. The next section highlights the significance of VSR as compared to the conventional rotorcraft with fixed RPM.

VARIABLE RPM ROTORCRAFT

The idea of passive morphing systems discussed in the previous section depends on the variation of rotor RPM, so it is also important to look at the progress in the VSR domain. Conventional rotorcraft operate with a fixed RPM throughout the flight envelope in order to avoid the potential vibration and resonance associated with the rotor [44]. Hence, the conventional helicopters show a good dynamic behavior because the eigenfrequencies and rotor harmonics are separated [45]. On the other hand, for VSR, it is a real challenge for dynamics engineers to choose a scope of reliable rotor speeds if the rotor speed is allowed to vary within even a limited range during the flight [44]. Due to the flight con-

dition called *resonant*, helicopter manufacturers are reluctant to use much variation in rotor speed [46]. Despite the additional complexities and challenges, the studies of VSR indicate that varying rotor speed is advantageous. For instance, in a study performed by Han et al., it is shown that for a flight at 70 m/s, when the rotor rotational speed is decreased to 82% of the nominal speed, power is reduced by 40% for the same output thrust that is required at constant rotor speed [47].

It is important to realize that multiple aspects such as flight envelope extension, power optimization, and fuel consumption benefit from using a VSR system for rotorcraft. Hence, the technology is promising and maybe an indispensable feature for future rotorcraft configurations [45]. For instance, in terms of fuel efficiency, researchers have reported fuel reductions in the range of about 10-13% for a VSR as compared to standard constant-speed rotor operation [48, 49]. In addition, generalized treatments of helicopter rotor theory have long indicated that, for a given disk loading and solidity, the choice of rotor-blade tip speed greatly affects the performance of helicopters in the hovering and forward flight conditions and that the tip-speed requirements in the two flight conditions are conflicting [50]. This indicates another potential source of performance benefit. As true airspeed increases, advancing tip Mach numbers become large, and retreating blade stall occurs, leading to increased vibration. Slowed rotors, as the name suggests, can alleviate this behavior by slowing the rotor speed [51]. For an auto-rotating rotor at high speed, slowing the rotor reduces the power required, whether the rotor is in isolation or in combination with a fixed-wing [52]. There are quite a few examples of helicopters that have been developed with variable-speed capability, the earliest one being McDonnell-XV1. One of the features of the XV-1 was that in airplane mode, the rotor would be slowed to a significantly lower speed to reduce its drag in forward flight [52]. Other notable examples include Bell's Eagle Eye, Boeing's A-160 Humming Bird, and Airbus Helicopter's EC-145.

For conventional rotorcraft, turboshaft engines are the most common choices [53], and a governor system works to maintain the constant speed. When the swashplate is raised by the collective pitch lever, the blade pitch is increased, resulting in an increase in the angle of incidence on each blade as shown in Fig. 2.5. This results in an increase in drag and, as a result, requires a proportional change in power to compensate for the drag penalty. The governor system in a conventional helicopter adjusts engine power automatically. The system is able to sense the rotor RPM, and since the rotor speed is proportional to the engine speed, the appropriate signal from the integrated circuit is transferred to a motor that adjusts the throttle to increase the power as desired. Modern helicopter turboshaft engines operate at a constant rotational speed, with typically allowed variations in speed not exceeding 15%, mainly to avoid resonant frequencies and secondly to avoid a decrease in engine efficiency while operating in off-design conditions [49].

For variable speed helicopters, researchers have explored different speed ranges in the past. Han et al. [54] mentions research work of rotor speed change in the range of (100%-53.8%), (100%-31.5%) and (100%-39.2%), explaining that increasing the range of the variation of the rotor speed is beneficial to the helicopter performance. Also, the influence of speed reduction in hover, low-speed, and high speed is different. During hover and slow flight modes, VSR has shown to be less beneficial than for high-speed regime

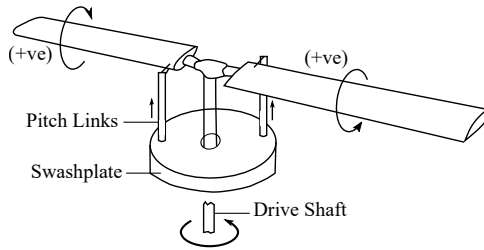


Figure 2.5: Change in blade pitch due to swashplate movement.

[55]. In the studies performed by Han et al. [56], the helicopter performance benefits by VSR and variable blade twist are investigated. It is found that the combination of VSR and variable blade twist can obtain more power reduction than individually varying rotor speed or blade twist. This is an important outcome and encourages further studies to observe the performance of camber morphing coupled with the VSR.

2.4. SUMMARY

The discussion in the preceding paragraphs indicates that primary flight control, flight performance, as well as noise and vibration mitigation are possible by employing trailing edge flaps. The primary control is, however, more challenging as it requires other design variables like blade index angle to be evaluated properly. Trailing edge *morphing* flaps offer similar capabilities with the added benefits of smooth shape changes. However, in terms of the design of the flap and its actuation, the challenges are complex, and the implementation has mostly remained limited as indicated in Fig. 1.3 in Chap. 1. However, as shown by the TRIC concept, the complexities of a morphing solution can be reduced to an extent by using conventional means design simplification. This signifies the importance of investigating conventional structures, materials, and systems for morphing concepts in rotorcraft also to minimize the number of unknowns and reduce the complexities. In addition, due to the high-frequency requirements of the actuation in rotor blades, the feasibility of such a concept for rotorcraft has to be established.

It is also highlighted in the literature review that the advantages of controlling rotor RPM are well established. However, the author was unable to find any study that relates the variation in RPM to camber morphing, despite being one of the most popular choices for active morphing in rotorcraft. If the slowed rotors are equipped with a camber morphing scheme that utilizes centrifugal forces for their operation, there is a potential to increase the rotorcraft performance.

BIBLIOGRAPHY

- [1] M. Mihir, "Quasi-Static Rotor Morphing Concepts for Rotorcraft Performance Improvements," no. December, 2012.
- [2] T. Oktay and F. Sal, "Combined passive and active helicopter main rotor morphing for helicopter energy save," *Journal of the Brazilian Society of Mechanical Sciences and Engineering*, vol. 38, pp. 1511–1525, 2016, ISSN: 18063691.
- [3] J. Blondeau, J. Richeson, D. J. Pines, and A. Norfolk, "Design , development and testing of a morphing aspect ratio wing using an inflatable telescopic spar," *44th AIAA / ASME / ASCE / AHS Structures , Structural*, vol. 1718, pp. 1–11, 2003, ISSN: 02734508.
- [4] H. P. Monner, H. Hanselka, and E. J. Breitbach, "Development and design of flexible Fowler flaps for an adaptive wing," *SPIE 3326, Smart Structures and Materials 1998: Industrial and Commercial Applications of Smart Structures Technologies, 60*, vol. 3326, pp. 60–70, 1998, ISSN: 0277786X.
- [5] J. SZODRUCH, "The influence of camber variation on the aerodynamics of civil transport aircraft," *23rd Aerospace Sciences Meeting*, 1985, ISSN: 01463705.
- [6] E. Garcia, "Smart structures and actuators: past, present, and future," pp. 1–12, 2002.
- [7] B. K. S. Woods, O. Bilgen, and M. I. Friswell, "ICAST2012: 23 rd International Conference on Adaptive Structures and Technologies Wind Tunnel Testing of the Fish Bone Active Camber Morphing Concept," pp. 1–14, 2008.
- [8] C. Thill, J. Etches, I. Bond, K. Potter, and P. Weaver, "Morphing skins," *Aeronautical Journal*, vol. 112, pp. 117–139, 2008, ISSN: 00019240.
- [9] A. Saxena and I. Chopra, "Development and testing of a swashplateless rotor with compact brushless motor actuated flaps for primary control," 2011.
- [10] J. Shen, M. Yang, and I. Chopra, "Swashplateless helicopter rotor with trailing-edge flaps for flight and vibration control," *Journal of Aircraft*, vol. 43, pp. 346–352, 2006, ISSN: 15333868.
- [11] B. A. Grohmann, C. Maucher, T. Prunhuber, P. Jänker, O. Dieterich, B. Enenkl, M. Bauer, E. Ahci, A. Altmikus, and H. Baier, "Multidisciplinary design and optimization of active trailing edge for smart helicopter rotor blade," *Mechanics of Advanced Materials and Structures*, vol. 15, pp. 307–324, 2008, ISSN: 15376494.
- [12] M. Melnykowycz, "Active Airfoil Design and Finite Element Analysis of Smart Structures for Rotor Blade Applications,"
- [13] C. Kessler, "Active rotor control for helicopters: Individual blade control and swashplateless rotor designs," *CEAS Aeronautical Journal*, vol. 1, no. 1-4, pp. 23–54, 2011.

- [14] M. Miller, J. Narkiewicz, W. Kania, and T. Czechyra, "The application of helicopter rotor blade active control systems for noise and vibration reduction and performance improvement," 2006.
- [15] D. Teves, G. Niesl, S. Jacklin, and M. Field, "The Role of Active Control in Future Rotorcraft," 1995.
- [16] S. A. Jacklin, A. Blaas, K.-c. Germany, D. Teves, and R. Kube, "Consumption Through Individual Blade Control," pp. 662–680, 1995.
- [17] B. Enenkl, "Dy 04 active rotor control by flaps for vibration reduction-full scale demonstrator and first flight test results," 2006.
- [18] J. Paik, R. Singh, F. Gandhi, and E. Hathaway, "Active tiltrotor whirl-flutter stability augmentation using wing-flaperon and swash-plate actuation," *Journal of Aircraft*, vol. 44, no. 5, pp. 1439–1446, 2007.
- [19] B. Grohmann, C. Maucher, and P. Jänker, "Actuation Concepts for Morphing Helicopter Rotor Blades," *Proceedings of the 25th International Congress of the Aeronautical Sciences*, pp. 1–10, 2006.
- [20] E. F. Prechtel and S. R. Hall, "<title>Design of a high-efficiency discrete servo-flap actuator for helicopter rotor control</title>," pp. 158–182, 1997.
- [21] K. Yee, W. Joo, and D. H. Lee, "Aerodynamic performance analysis of a gurney flap for rotorcraft application," *Journal of Aircraft*, vol. 44, pp. 1003–1014, 2007, ISSN: 0021-8669.
- [22] J. G. Leishman, "A History of Helicopter Flight,"
- [23] M. V. Hoagland, "Development of a Low Cost Product: The K-max Story," in *19th Congress of the International Council of the Aeronautical Sciences and the American Institute of Aeronautics Aircraft Systems Conference*, Anaheim, CA: AIAA, 1994.
- [24] J. Milgram, I. Chopra, and F. Straub, "Rotors with trailing edge flaps: Analysis and comparison with experimental data," *Journal of the American Helicopter Society*, vol. 43, pp. 319–332, 1998, ISSN: 00028711.
- [25] H. Yeo, R. Jain, and B. Jayaraman, "Investigation of rotor vibratory loads of a UH-60A individual blade control system," *Journal of the American Helicopter Society*, vol. 61, 2016, ISSN: 00028711.
- [26] B. Enenkl, V. Klöppel, D. Preißler, and P. Jänker, "Full Scale Rotor with Piezoelectric Actuated Blade Flaps," *28th European Rotorcraft Forum*, pp. 89.1–X, 2002.
- [27] E. R. Booth and M. L. Wilbur, "Acoustic Aspects of Active-Twist Rotor Control," *Journal of the American Helicopter Society*, vol. 49, pp. 3–10, 2004, ISSN: 00028711.
- [28] F. Gandhi and P. Anusonti-Inthra, "Skin design studies for variable camber morphing airfoils," *Smart Materials and Structures*, vol. 17, 2008, ISSN: 09641726.
- [29] J. Shen and I. Chopra, "Swashplateless Helicopter Rotor with Trailing-Edge Flaps," *Journal of Aircraft*, vol. 41, pp. 208–214, 2004, ISSN: 15333868.
- [30] Y. Lu and C. Wang, "Active control for performance enhancement of electrically controlled rotor," *Chinese Journal of Aeronautics*, vol. 28, pp. 1494–1502, 2015, ISSN: 10009361.

- [31] X. Lachenal, S. Daynes, and P. Weaver, "Review of morphing concepts and materials for wind turbine blade applications," *Wind Energy*, vol. 16, pp. 283–307, 2013.
- [32] J. Alejandro Franco, J. Carlos Jauregui, and M. Toledano-Ayala, "Optimizing Wind Turbine Efficiency by Deformable Structures in Smart Blades," *Journal of Energy Resources Technology*, vol. 137, p. 051 206, 2015, ISSN: 0195-0738.
- [33] O. Ben-Zeev and I. Chopra, "Advances in the development of an intelligent helicopter rotor employing smart trailing-edge flaps," *Smart Materials and Structures*, vol. 5, pp. 11–25, 1996, ISSN: 09641726.
- [34] R. P. Thornburgh, A. R. Kreshock, M. L. Wilbur, and M. K. Sekula, "Continuous Trailing-Edge Flaps for Primary Flight Control of a Helicopter Main Rotor," *AHS 70th Annual Forum*, 2014, ISSN: 15522938.
- [35] F. Gandhi, M. Frecker, and A. Nissly, "Design optimization of a controllable camber rotor airfoil," *AIAA Journal*, vol. 46, pp. 142–153, 2008, ISSN: 00011452.
- [36] R. Vos, Z. Gurdal, and M. Abdalla, "Mechanism for Warp-Controlled Twist of a Morphing Wing," *Journal of Aircraft*, vol. 47, pp. 450–457, 2010, ISSN: 0021-8669.
- [37] N. Werter, J. Sodja, G. Spirlet, and R. De Breuker, "Design and Experiments of a Warp Induced Camber and Twist Morphing Leading and Trailing Edge Device," *24th AIAA/AHS Adaptive Structures Conference*, pp. 1–20, 2016.
- [38] G. B. Spirlet, "Design of Morphing Leading and Trailing Edge Surfaces for Camber and Twist Control," no. June, 2015.
- [39] U. Army, *Rotary Wing Flight - Flight Manual 1-51*. United States, Department of the Army, 1979.
- [40] S. Barbarino, F. Gandhi, and S. D. Webster, "Design of extendable chord sections for morphing helicopter rotor blades," *Journal of Intelligent Material Systems and Structures*, vol. 22, pp. 891–905, 2011, ISSN: 1045389X.
- [41] M. Khoshlahjeh and F. Gandhi, "Extendable chord rotors for helicopter envelope expansion and performance improvement," *Journal of the American Helicopter Society*, vol. 59, pp. 1–10, 2014, ISSN: 00028711.
- [42] P. Moser, S. Barbarino, and F. Gandhi, "Helicopter Rotor-Blade Chord Extension Morphing Using a Centrifugally Actuated Von Mises Truss," *Journal of Aircraft*, vol. 51, pp. 1422–1431, 2014, ISSN: 0021-8669.
- [43] T. Prabhakar, F. Gandhi, J. Steiner, and D. McLaughlin, "A centrifugal force actuated variable span morphing helicopter rotor," *Annual Forum Proceedings - AHS International*, vol. 1, pp. 710–724, 2007, ISSN: 15522938.
- [44] G. Wei, "Flight Control Design for Rotorcraft with Variable Rotor Speed," no. December, 2009.
- [45] H. Amri, R. Feil, M. Hajek, and M. Weigand, "Possibilities and difficulties for rotorcraft using variable transmission drive trains," *CEAS Aeronautical Journal*, vol. 7, pp. 333–344, 2016, ISSN: 18695590.
- [46] P. R. W., "Should we consider variable rotor speeds?," no. Vertiflite, 50 (4) (2004), pp. 24–27, 2009.

- [47] D. Han and E. C. Smith, "Lagwise dynamic analysis of a variable speed rotor," *Aerospace Science and Technology*, vol. 29, pp. 277–286, 2013, ISSN: 12709638.
- [48] J. F. Horn, "Implementation of Variable RPM in Helicopter Flight Control Laws," *The 3rd International Basic Research Conference on Rotorcraft Technology*, 2009, ISSN: 2356-6140.
- [49] G. A. Misté and E. Benini, "Variable-Speed Rotor Helicopters: Performance Comparison Between Continuously Variable and Fixed-Ratio Transmissions," *Journal of Aircraft*, vol. 53, pp. 1189–1200, 2016, ISSN: 0021-8669.
- [50] E. B. Gustafson and A. Gessow, "Effect of rotor-tip speed on helicopter hovering performance and maximum forward speed," *Naca Arr No. L6a16*, 1946.
- [51] C. Silva, H. Yeo, and W. Johnson, "Design of a Slowed-Rotor Compound Helicopter for Future Joint Service Missions," *American Helicopter Society Aeromechanics Specialists' Conference*, 2010.
- [52] M. W. Floros and W. Johnson, "Performance Analysis of the Slowed-Rotor Compound Helicopter Configuration," *Journal of the American Helicopter Society*, vol. 54, pp. 22 002–2 200 212, 2009, ISSN: 21616027.
- [53] J. Schenderlein and T. Clayton, "Comparison of Helicopter Turboshaft Engines," pp. 1–14, 1953.
- [54] D. Han and G. N. Barakos, "Variable-speed tail rotors for helicopters with variable-speed main rotors," *Aeronautical Journal*, vol. 121, pp. 433–448, 2017, ISSN: 00019240.
- [55] J. Xie, N. Guan, M. Zhou, and Z. Xie, "Study on the mechanism of the variable-speed rotor affecting rotor aerodynamic performance," *Applied Sciences*, vol. 8, no. 7, 2018, ISSN: 2076-3417.
- [56] D. Han, V. Patrikakis, and G. N. Barakos, "Helicopter performance improvement by variable rotor speed and variable blade twist," *Aerospace Science and Technology*, vol. 54, pp. 164–173, 2016, ISSN: 1270-9638.

3

CAMBER MORPHING FLAP CHARACTERIZATION

I prefer a fast prediction of 80% reliability in three hours rather than a solution of 100% accuracy in a week. The industry is often willing to take that risk.

Christos Kassapoglou

This chapter presents the design methodology for a compliant morphing flap for helicopter rotor blades that can work both in active and passive mode.

The chapter is organized as follows. Section 3.1 explains the design approach and considerations for the design and analysis carried out during the present study for the morphing skin. It gives a detailed account of the design framework for the morphing skin. Section 3.2 describes the numerical modelling used to establish the morphing shapes and the actuator forces. Section 3.3 provides an overview of the critical parameters that affect the design of the morphing flap in terms of the final material and layup selection.

3.1. DESIGN APPROACH

Before discussing the details of the skin for a morphing flap, it is important to highlight the key concept investigated in the present work for morphing in rotorcraft.

In the literature study presented in Chap. 2, several options for morphing are discussed. However, it is highlighted that trailing edge camber morphing is generally preferred for rotorcraft. Furthermore, for the overall morphing scheme, the TRIC morphing concept is mentioned which was envisaged for a fixed-wing aircraft. Due to its relative simplicity, use of conventional materials and opportunity to use off-the-shelf actuation options, this concept becomes an ideal candidate for the design and feasibility study for rotorcraft. Therefore, the present work explores the possibilities of implementing the TRIC morphing concept for rotorcraft.

The operational principle of the TRIC concept conceived for rotorcraft is shown in Fig. 3.1. It comprises of a hollow trailing edge portion, while the rest of the blade is based on a conventional rotor blade structure. This hollow trailing edge portion can be morphed using an actuation system. The desired actuation mechanism and trailing edge flap can be incorporated in a blade where required. Although the mass distribution and dynamic response of the blade would change for an existing blade, a modular design offered by TRIC morphing concept has its own benefits in terms of maintenance and inspection. By introducing the required actuators and appropriate trailing edge changes, an effective morphing mechanism can be developed.

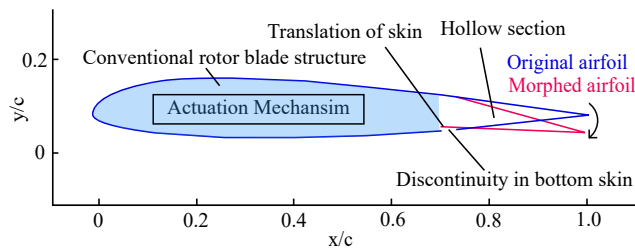


Figure 3.1: Proposed operational principle of TRIC for rotorcraft.

Keeping in view the TRIC concept and its application in rotorcraft, the design process mainly involves two key design elements, i.e., the morphing skin and the actuation mechanism. The present chapter deals with the design and analysis of the morphing skin for which a generalized approach is presented applicable to any rotorcraft demand-

ing a similar morphing solution. However, to help understand the applicability of the overall solution and quantify important parameters, the Bo105 helicopter [1] is taken as the baseline rotor to generate rotor-specific requirements.

3.1.1.1. DESIGN CONSIDERATIONS

At the initial design phase, key requirements have to be defined which can influence the outcome of the overall design to a larger extent. For instance, the requirements specific to a camber morphing solution need to have sizing, frequency and operational speed defined. For the case under consideration, the design requirements are stated in Tab. 3.1.

Table 3.1: Design requirements with respect to Bo105.

Property	Unit	Value
Control method	-	Active/Passive
Rotor radius	m	4.91
Rotation speed	rad/sec	44.4
Blade chord	mm	270
Airfoil type	-	Bo105 (NACA 23012)
Frequency	-	Quasi-static to 2/rev or higher
Advance Ratio	-	0.3

In Chap. 2 it is mentioned that some extra parameters such as blade index angle are required to reduce the flap control requirements in the flap for primary flight control. Shen et al. have shown that even moderate flap angles of around 2° to 6° can be used for active vibration control (5/rev) and primary flight control by having a blade-pitch index angle of 16° [2]. In a similar study, the authors also show that the flap deflection angles for vibration control can be as low as 40% compared to that required for the primary flight control [3]. Keeping this in perspective, the design process described in this chapter intends to achieve the downward flap deflection in the range of 6° to 8° . Since the flap control power is not considered during the present research work, these moderate flap deflection angles also keep the actuation possibilities open for a broader range of off-the-shelf actuators such as the piezoelectric actuators, which are limited by the stroke [4]. The definition of a morphed shape in terms of required deflection angle is shown in Fig. 3.2. The flap deflection angle is considered positive downwards. The flap's imaginary hinge is assumed to be located at 75% of the blade chord. For a flap length equal to 25% of the chord length, the deformed chord line makes an angle β as shown in Fig. 3.2.

In terms of the design objectives, the present study focuses on obtaining the required flap deflection and the corresponding actuation force. The deformed shapes are obtained for the two cases, i.e., under pure elastic loads and under aerodynamic loads obtained using 2D Computational Fluid Dynamics (CFD) simulation. However, based on the aerodynamic loads, unless the skin is sufficiently stiff, both the tip deflection and the deformed shape can vary significantly between the two cases. These criteria of a close match, both in terms of the tip deflection and deformed shape between the two cases, give rise to the requirement of a steady-state shape. To obtain the steady-state shape,

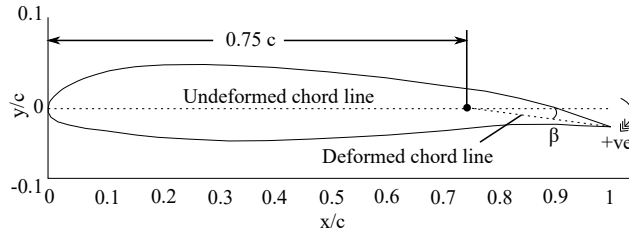


Figure 3.2: Deflection angle definition.

the thickness of the skin is increased (for a given material) when the maximum aerodynamic load is applied on the undeformed (baseline) shape in the Finite Element Analysis (FEA). An increase in thickness beyond a particular value has no significant influence on the deformed shape and the corresponding tip deflection. The resulting steady-state shape is used again in the CFD to obtain the aerodynamic loads for the next deflection case, and the process is repeated till the criteria of achieving the steady-state shape are satisfied. However, to keep the actuation loads as low as possible, another design objective is to find the minimum thickness of the skin that meets the above-referred criteria. Moreover, it is assumed that the complete flap is subjected to a uniform spanwise aerodynamic load, unlike the actual scenario for a rotor blade. This assumption works for the preliminary design phase, especially for smaller flap lengths and when the design is based on the worst-case scenario.

3.2. ANALYSIS METHODOLOGY

A Fluid-Structure Interaction (FSI) scheme is devised to determine the morphed shapes and corresponding actuation forces under flexible aero loads required to obtain the morphed shapes. To develop this scheme, a similar approach as presented by Daynes et al. is adopted. They coupled XFOIL¹ and Abaqus² for the FSI model [5]. In the present case, the author has used CFD (Ansys Fluent³), which uses Finite Volume Method (FVM), to obtain the aerodynamic loads. Abaqus/Standard is used as the FEA tool, which is more efficient in solving non-linear problems. However, the automatic coupling of the two software is not implemented at this stage since the number of morphed shapes is kept limited, and the aim is to find the actuation loads based on the worst-case load scenario. The basic methodology of the FSI scheme is shown in Fig. 3.3.

The process starts by specifying the design requirements for the design of the skin. These requirements include the type of airfoil, location and size of the flap, operating frequencies, range of deflections, Mach number, and angle of attack during the operation of the flap. As shown in Fig. 3.3, the 2D flow analysis is carried out using CFD simulations to calculate the aerodynamic loads on the skin for various morphed shapes starting from the unmorphed or baseline shape. This information is used in the FEA to observe the deflections under the influence of aerodynamic loads. This analysis helps

¹<https://web.mit.edu/drela/Public/web/xfoil>

²<https://www.3ds.com/products-services/simulia/products/abaqus/abaquscae>

³<https://www.ansys.com/products/fluids/ansys-fluent>

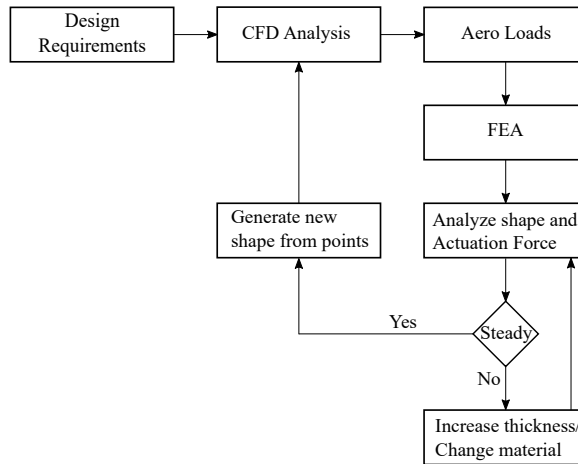


Figure 3.3: Basic methodology of the FSI scheme.

in determining both the desired morphed shapes and actuation forces for a given load case. Afterwards, the response of the flap, in terms of tip deflection and shape, is compared to the steady-state shape. A morphed shape must conform to the tip deflection and shape of the steady-state shape. If the criteria are not satisfied, the skin thickness is increased for the given material, and the above-mentioned process is repeated. Once these criteria are satisfied, a new morphed shape corresponding to a higher deflection angle is generated through the point data in FEA, and the process is repeated for the new shape.

For the implementation of the FSI scheme, a Matlab tool is developed to transfer loads from the CFD to the FEA, as shown in Fig. 3.4. The key steps performed to obtain the Finite Element Model (FEM) are as follows:

1. Nodal coordinates (corresponding to the mesh), forces, and moments are obtained in the form of a text file from the CFD after conducting the flow simulation on a particular airfoil shape.
2. Nodal coordinates corresponding to the mesh generated in FEA are obtained in the form of a text file for the same airfoil shape.
3. Due to the difference in the mesh sizes in the CFD simulations and the FEA analysis, Matlab's Nearest neighbour search is used to identify the closest coordinates of the FEA text file that are present in the CFD text file.
4. The forces and moments of these points are linked to the coordinate data from the FEA text file. Consequently, a text file is generated for the FEA.
5. In the FEM, the nodal forces and moments are applied using the file obtained in the previous step.

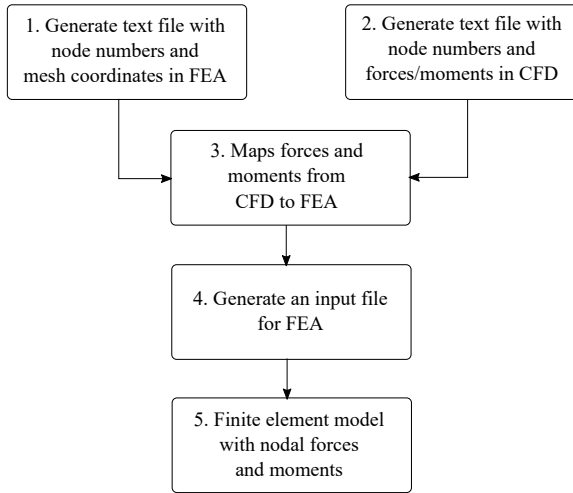


Figure 3.4: Implementation of the FSI scheme.

The flap used in the TRIC concept is subjected to the boundary conditions shown in Fig. 3.5 which are similar to those used in the initial version of the TRIC concept [6]. The portion of the top skin which is fixed to the rotor blade structure is constrained in all degrees of freedom (DOF) in the FEM. The bottom skin, which translates in the chordwise direction, is constrained in the out-of-plane direction. The node shown in Fig. 3.5 is subjected to a displacement in the chordwise direction. The resulting translation of the bottom skin causes the top skin to deform, giving the corresponding morphed shape. Consequently, the reaction force for the actuators is estimated on the node shown in Fig. 3.5.

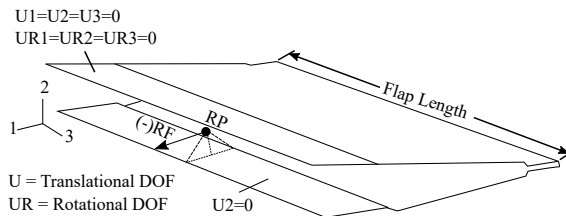


Figure 3.5: Boundary condition for the TRIC concept.

The resulting file obtained in step four is used in the Python Development Environment (PDE) of Abaqus to transfer the loads and moments to the respective nodes. Before the analysis, a mesh convergence study is done for the analysis as given in Tab. 3.2 based on which a mesh size of 2 mm is chosen. The elements used in the FEA are S4R general-purpose shell elements [7].

The resulting morphed shapes, as shown in Fig. 3.6, are used for the subsequent simulations in CFD to get the aerodynamic loads and coefficients, while the reaction forces obtained during these studies are used for the actuator selection. The baseline shape

Table 3.2: Mesh convergence study.

Mesh (mm)	Stress (MPa)	Reaction Force (N/m)
0.5	57.2	160
2	56	161
5	44	164

shown in Fig. 3.6 is the undeformed shape. Once the actuator selection is made based on the worst-case loads, the resulting information is used to design the actuation mechanism.

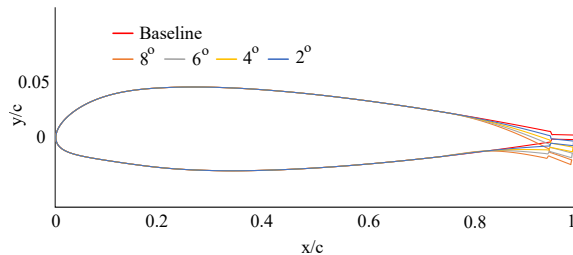


Figure 3.6: Trailing edge camber morphing for different deflections.

3.2.1. CFD STUDIES

In CFD simulations, the accuracy of the solutions is highly dependent on the quality of the mesh [8]. Mesh refinement is done till the majority of the C_l values are approximately around 10% of the corresponding values found in the experimental data. The final refined mesh for the deformed and undeformed shapes is a C-grid mesh with the number of cells equal to approximately 90,000, as shown in Fig. 3.7. The airfoil shapes are placed in this domain such that the outer boundary is more than 25 times the blade chord length all around. The airfoil surface is considered a viscous wall in the fluid domain. The fluid is assumed compressible choosing the ideal gas, and pressure-far-field is selected as the boundary condition. The dimensionless wall distance y^+ is kept close to 1 since no wall functions are used to resolve the boundary layer. To carry out the flow simulation, a pressure-based solver is used. The turbulence model used for the studies is the Spallart Allmaras (SA) model [9], which is a one-equation Reynolds-Averaged Navier Stokes (RANS) based model.

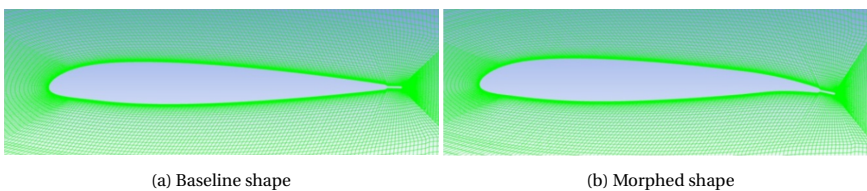


Figure 3.7: Final CFD mesh after refinement.

To validate the resulting mesh and model, the results for the baseline shape are compared to the experimental data [10] shown in Fig. 3.8, showing a close agreement between the two cases.

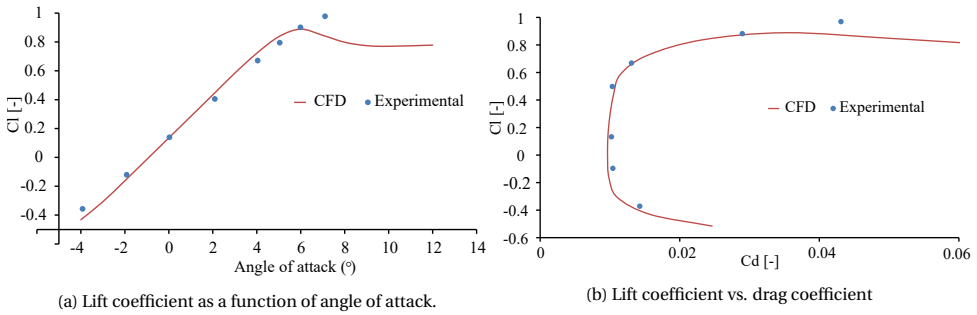


Figure 3.8: Comparison of CFD and experimental results for baseline shape at Mach 0.6.

Figure 3.9 presents the results of the CFD simulations carried out at Mach 0.37. Although the present study focuses on the positive deflections of the morphed flap, the CFD simulations are performed by varying the flap deflection angle between -4° and $+8^\circ$ with an interval of 2° to reduce the computational effort. Each morphed shape is generated by following the procedure mentioned earlier. The angle of attack is changed between -6° and $+16^\circ$ for the CFD simulations. Figures 3.9a and 3.9b show the behaviour of lift and drag coefficients for different morphed shapes in comparison to the baseline shape. The trend of higher $C_{l(max)}$ with higher camber is observed in both Figs. 3.9a and 3.9b. Also, for $C_{l(min)}(\text{Baseline}) \leq C_l \leq C_{l(max)}(\text{Baseline})$, the airfoil polars are closely stacked. This shows that morphed airfoils produce more lift with the same drag penalty as that attributed to the baseline airfoil. Abdelmoula et al. also noted similar observations when they studied the morphed camber airfoils at Mach 0.4 [9].

To quantify the aerodynamic efficiency of the concept, the lift-to-drag ratio is plotted for different morphed shapes at Mach 0.37, as shown in Fig. 3.9c. It can be seen that the aerodynamic efficiency increases by increasing the trailing edge camber morphing. This increase is more pronounced for $C_l \geq 1$ and higher flap deflection angles of 6° and 8° . In addition, the requirement of low pitching moment is one key parameter to minimize rotor control loads, that are a result of blade torsional dynamics [9]. As seen from Fig. 3.9d, the pitching moments coefficient around $+5^\circ$ remain less than -0.1 . As mentioned in [9], the airfoils with a 2D section C_m between -0.1 and 0.1 can still be safely used. It can also be observed that the compressibility effects are more pronounced on the C_m variations for the shapes with higher deflection angles.

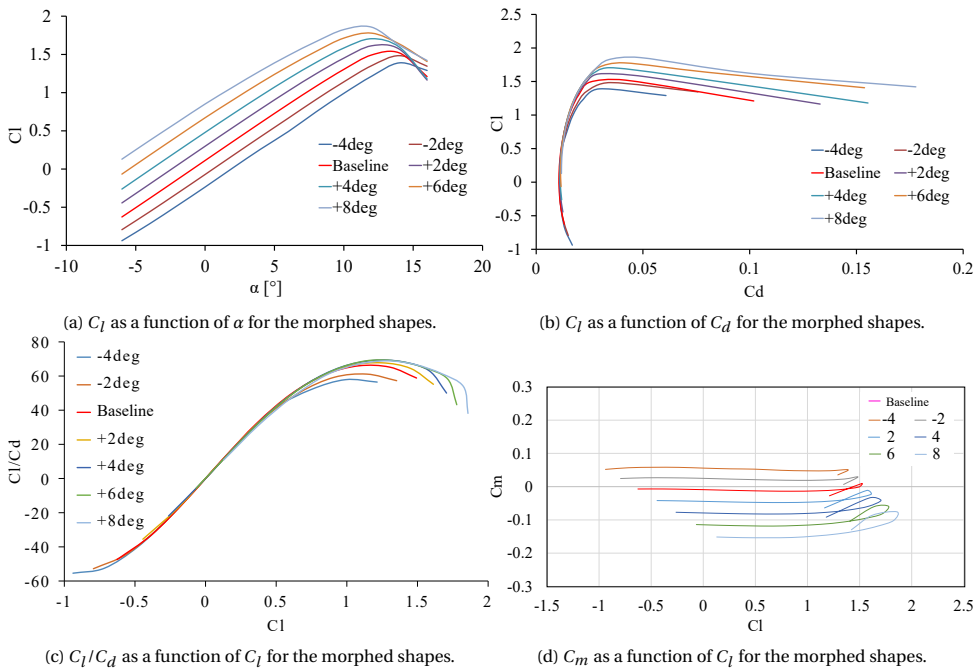


Figure 3.9: Results of aerodynamic analysis for different morphed shapes at Mach 0.37.

3.3. DESIGN STUDY OF MORPHING SKIN

As mentioned earlier, two of the primary design outcomes of the proposed concept are the steady-state morphed shapes and the corresponding actuation forces. During the course of studies performed by the author, it is observed that the thickness of the material, the type of material, stacking sequence for composite materials, and chord length of the trailing edge section are important factors to be considered as each of these influences the actuator selection with respect to a steady-state morphed shape. Hence, before finalizing the design of the morphing skin for the TRIC concept, a study is carried out to investigate the effects of the above-mentioned design considerations. Using the approach described in Sec. 3.2, the study is performed for a flap subjected to aerodynamic loads at Mach 0.46 at 10° angle of attack. For the Bo105 helicopter, this hover case corresponds to placing a flap at $0.75R$ (R is the rotor blade radius), as shown in Fig. 3.10. The outcome of this investigation results in the deformed shapes along with the mass and required actuator forces for each morphed shape. These results help in the overall design scheme of the trailing edge morphing flap keeping in view strength, flexibility, and weight considerations. Once these criteria are satisfied, the skin can be further analyzed for any potential damage under the same loading conditions using a failure criterion such as the Hashin damage model, which is a damage initiation criterion for composites [11].

As described in Sec. 3.1.1, the important factors for a deformed shape are to achieve both the desired deflection angle and also a close match to the steady-state shape. To

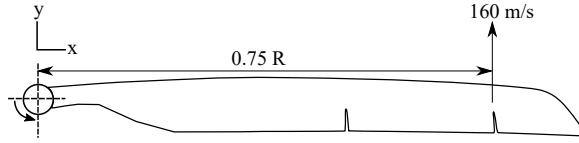


Figure 3.10: Flap depiction.

represent the similarity of the two shapes, the Kolmogorov–Smirnov (KS) test [12] is employed. Considering 2D airfoils, the y -coordinates of the steady-state shape are normalized with respect to the blade chord length. Afterwards, the cumulative values of the y -coordinates of the shape are calculated for the steady-state shape and also for the morphed shape using Eq. 3.1:

$$s_j = \sum_{i=1}^j y_i \quad (3.1)$$

where s_j represents the cumulative sum, y_i are the values representing the y -coordinates of the shape normalized with respect to the blade chord length, and j represents the number of coordinate points. A “Similarity Index” (SI) is then established by obtaining the maximum distance between the cumulative distributions as shown in Eq. 3.2. The smaller the value of SI, the better the match to the desired shape and vice versa.

$$SI = \text{Max}(\Delta s_j) \quad (3.2)$$

where Δs_j represents the maximum value of the difference between the cumulative values calculated for the steady-state shape and the deformed shape.

3.3.1. EFFECT OF MATERIAL THICKNESS

In order to specifically observe the effect of material thickness, an isotropic material is considered. Subsequently, the effect of thickness is explored by following the aforementioned approach. For this purpose, morphed shapes are generated for a deflection from 0° to 8° for a skin made of aluminium. The morphed shapes are generated at intervals of 2° to reduce the computational effort and by varying the thickness until the criterion for steady-state is satisfied. The thickness is varied from 0.1 mm to 1.5 mm.

Figure 3.11 represents the outcome of the study based on the KS test. It can be observed that for each deflection angle, there is a point where both criteria of the desired shape and tip deflection are met. In general, for all the cases, a SI of less than 0.3 gives a close match. It can be seen from these plots that increasing the thickness or stiffness of the skin beyond a certain design point would have no significant effect on the structural response of the skin and would only serve to increase the weight.

Figure 3.12 helps to visualize the effect of the above-mentioned scheme on the actual shape corresponding to 2° deflection. Figure. 3.12a shows the cumulative distribution is plotted for a skin thickness of 0.1 mm and 0.6 mm, while Fig. 3.12b shows the behaviour of the actual shape.

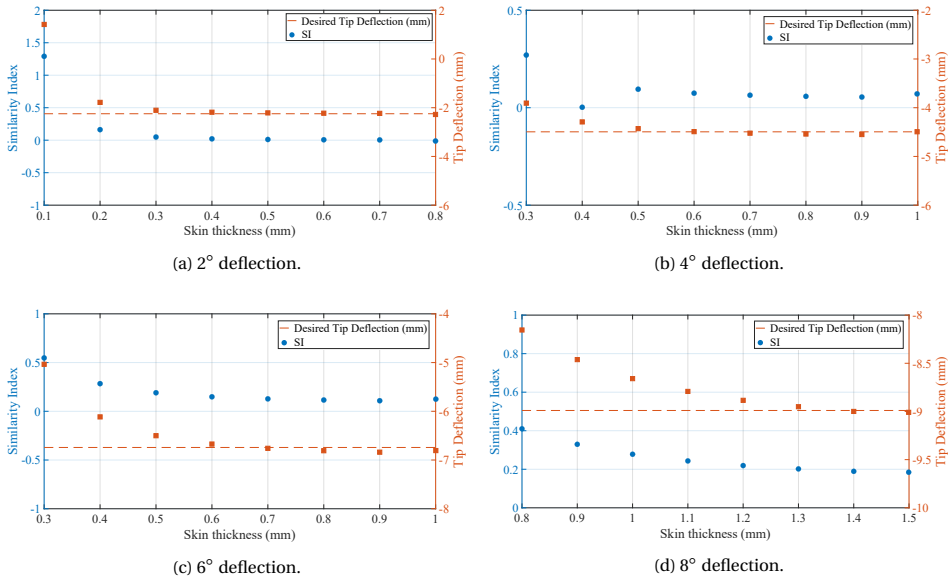


Figure 3.11: Similarity index and tip deflections for different deflections.

3.3.2. EFFECT OF MATERIAL AND LAYUP

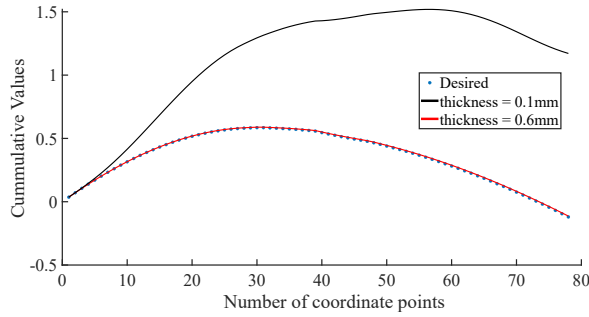
For the material effect analysis, four different materials are selected as potential candidates, i.e., aluminium, unidirectional (UD) prepreg carbon fibre [13], plain weave carbon fabric [13], and UD prepreg carbon fibre with thin plies [14] called Thinpreg. Table 3.3 shows the material designation and properties used for the subsequent studies.

Table 3.3: Properties of the candidate materials.

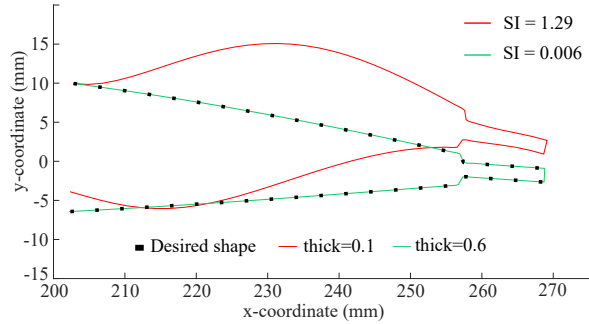
Property	UD Carbon Fibre	Plain Weave Carbon Fabric	Thinpreg	Aluminum
E_{11} (GPa)	138	68.9	85.63	68.3
E_{22} (GPa)	11.4	68.9	9.06	68.3
ν_{12}	0.29	0.05	0.27	0.34
G_{12} (GPa)	4.83	4.83	5	26
t_{ply} (mm)	0.1524	0.1905	0.05	-

While dealing with the composite laminates, it is crucial to have a stacking sequence that provides both the required strength and flexibility. Due to this reason, different layups are investigated with variable thickness to get an overview of the impact. This analysis is again performed at aerodynamic loads corresponding to Mach 0.46 and considering stacking sequences such as balanced, symmetric, and quasi-isotropic. The SI and tip deflection is obtained by changing the layup for each material to get the desired flap deflection of 6°. The SI and corresponding tip deflections for each material are shown in Fig. 3.13, 3.14 and 3.15.

Table 3.4 summarizes the data of steady-state shapes against each material and the corresponding actuation force.



(a) Effect of thickness on cumulative values.



(b) Effect of thickness on deformed shape

Figure 3.12: Effect of thickness on 2° deflection.

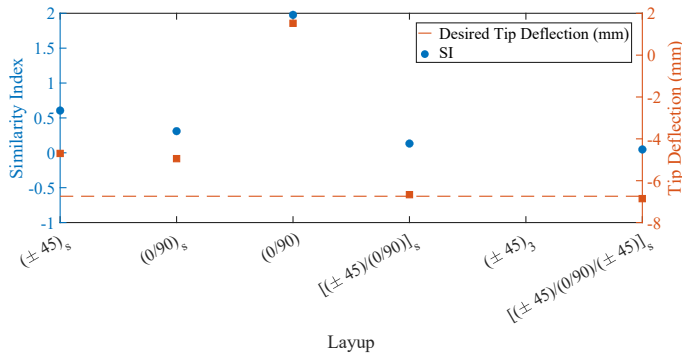


Figure 3.13: Similarity index and tip deflections for fabric.

The results in Tab. 3.4 show that in terms of mass and elastic force, both serial numbers 1 and 7 (fabric and Thinpreg) give acceptable solutions while maintaining the desired shapes under the given loads. For the case of UD prepreg, serial number 5 results in less skin thickness when compared to serial number 6 but at the cost of a higher actuation force. From a morphing perspective, it is important to keep the overall weight as low as possible. Therefore, a higher actuation force also means a potentially larger and heavier actuation system. In addition, the effect of increasing the plies for a better

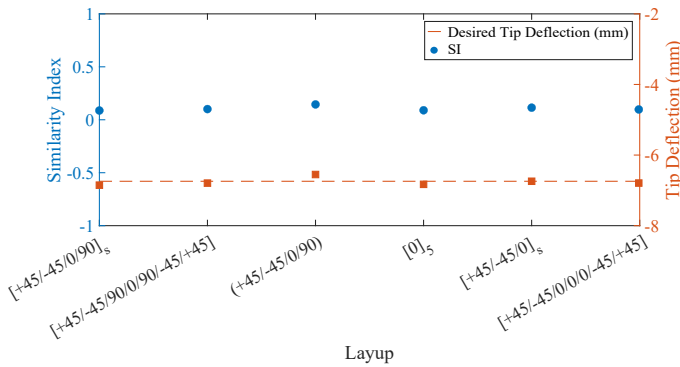


Figure 3.14: Similarity index and tip deflections for UD carbon prepreg.

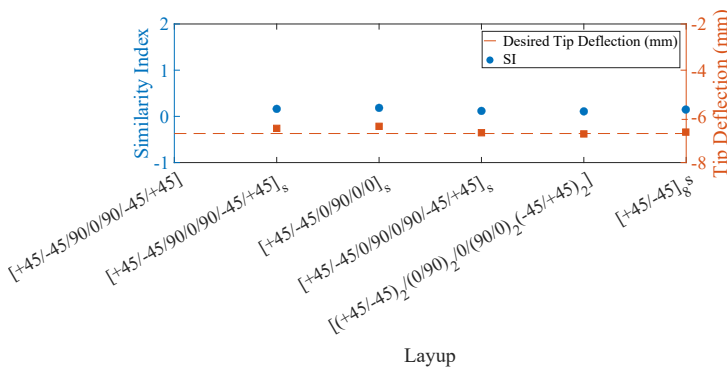


Figure 3.15: Similarity index and tip deflections for Thinprepreg.

Table 3.4: Actuator forces for 6° deflection.

Sr. No	Material	Layup	Ply thickness (mm)	Skin thickness (mm)	Actuation force (N/mm)
1	Fabric	[+45/ - 45/0/90]s	0.1905	0.762	1.07
2	Fabric	[+45/ - 45/0/90/ - 45/ + 45]s	0.1905	1.143	1.36
3	UD prepreg	[+45/ - 45/90/0/90/ - 45/ + 45]	0.1524	1.066	1.41
4	UD prepreg	[+45/ - 45/0/0/0/ - 45/ + 45]	0.1524	1.066	1.18
5	UD prepreg	[0]5	0.1524	0.762	1.11
6	UD prepreg	[+45/ - 45/0/90]s	0.1524	1.219	1.05
7	Thinprepreg	[+45/ - 45/0/90/0/90/ - 45/ + 45]s	0.05	0.8	1.05
8	Thinprepreg	[(+45/ - 45)2/(0/90)2/0/(90/0)2/(-45/ + 45)2]	0.05	0.85	1.15
9	Aluminum	-	0.8	0.8	1.23

match to the desired shape and tip deflection can be observed in Fig. 3.13, where the (0/90)s layup indicates a better match than the (0/90) layup.

For the demonstrators, Thinprepreg is preferred because it offers thin plies, giving more freedom in the number of plies and ply orientations. In addition, the extensive literature on composite materials suggests that thin plies delay delamination and matrix cracking [14]. In addition, the assessment of any potential damage is observed using the Hashin

damage model in Abaqus. The variables in this model indicate whether an initiation criterion in a damage mode has been satisfied or not; a value that is less than 1.0 indicates that the criterion has not been satisfied [7].

3.3.3. EFFECT OF TRAILING EDGE MORPHING LENGTH

The maximum lift of the plain flap is dependent on the flap chord, and a flap chord ratio between 0.2c to 0.3c generally yields the highest value of the maximum lift coefficient [15]. In addition, the optimum flap chord is often considered at 0.25c because of the optimum lift coefficient [16]. However, it is still important to establish the effect of varying chord length around this value of 0.25c because a deviation from this ideal value of 0.25c is inevitable in some instances. For instance, if the volume available to house the actuation system is insufficient, the chord length will be changed accordingly. For this reason, CFD simulations followed by the FEA analysis are carried out for a flap deflection of 8° to obtain the actuation force corresponding to aerodynamic loads at Mach 0.46 and 10° angle of attack. The material used in this case is aluminium having a skin thickness of 1.5 mm. The actuation forces corresponding to the elastic load are also noted in this study.

Figure 3.16 represents the plot for the actuation force corresponding to the elastic load, aerodynamic load, and total force. It can be observed that the elastic forces tend to decrease when the flap chord length increases. On the contrary, the aerodynamic forces show a slight increase in this case. The contribution of the aerodynamic force to the total force increases with the increase in flap chord length. However, the total force tends to decrease as the flap chord length increases. The outcome of this study indicates that although increasing the chord length may seem to be the preferred approach in terms of reduced loading requirement; the lower available volume might reduce the choice of actuators. On the contrary, reduction in the flap chord length from 30% to 20% increases the total force requirement by approximately 75%. Thus the final selection of the chord length should consider the volume available to house the required actuation system. Particularly for rotor blades, the volume constraint can become the deciding factor when selecting a chord length.

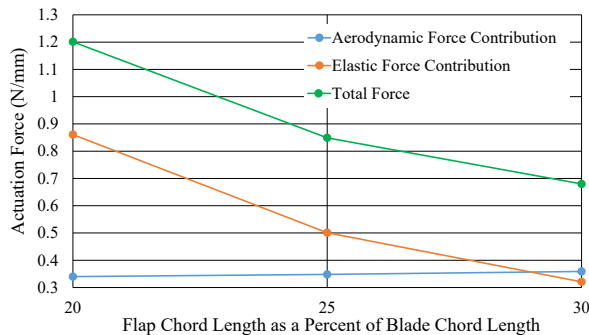


Figure 3.16: Change in actuation force corresponding to elastic and aero loads.

3.4. SUMMARY

This chapter was dedicated to the characterization of the morphing flap which was based on the TRIC concept. A design methodology was presented where the aerodynamic loads were transferred from CFD simulations to the FEA to get the desired morphed shapes. This was accomplished by mapping the nodal forces and moments from the CFD to the respective nodes in FEA. This method ensured that the aerodynamic forces are transferred in the FEA properly. The significance of a steady-state shape was also established, which ensured that increasing the flap stiffness did not affect the morphed shape. In addition, factors affecting the shape and actuation forces such as thickness, flap chord length, flap material, and stacking sequence were studied to show that an appropriate selection was possible by considering the actuation forces, shapes, and weight of the skin. The FSI scheme presented in this chapter was validated with the wind tunnel experiment and presented in Chap. 8.

BIBLIOGRAPHY

- [1] K. Kindler, E. Goldhahn, F. Leopold, and M. Raffel, "Recent developments in background oriented Schlieren methods for rotor blade tip vortex measurements," *Experiments in Fluids*, vol. 43, no. 2-3, pp. 233–240, 2007.
- [2] J. Shen and I. Chopra, "Swashplateless Helicopter Rotor with Trailing-Edge Flaps," *Journal of Aircraft*, vol. 41, pp. 208–214, 2004, ISSN: 15333868.
- [3] J. Shen, M. Yang, and I. Chopra, "Swashplateless helicopter rotor with trailing-edge flaps for flight and vibration control," *Journal of Aircraft*, vol. 43, pp. 346–352, 2006, ISSN: 15333868.
- [4] J. H. Lee, B. Natarajan, W. J. Eun, S. R. Viswamurthy, J. S. Park, T. Kim, and S. J. Shin, "Structural and mechanism design of an active trailing-edge flap blade," *Journal of Mechanical Science and Technology*, vol. 27, pp. 2605–2617, 2013, ISSN: 1738494X.
- [5] S. Daynes and P. M. Weaver, "Morphing blade fluid-structure interaction," *Collection of Technical Papers - AIAA/ASME/ASCE/AHS/ASC Structures, Structural Dynamics and Materials Conference*, no. April, 2012, ISSN: 02734508.
- [6] N. Werter, J. Sodja, G. Spirlet, and R. De Breuker, "Design and Experiments of a Warp Induced Camber and Twist Morphing Leading and Trailing Edge Device," *24th AIAA/AHS Adaptive Structures Conference*, pp. 1–20, 2016.
- [7] (). "Damage initiation for fiber-reinforced composites," [Online]. Available: <https://abaqus-docs.mit.edu/2017/English/SIMACAEMATRefMap/simamat-c-damageinitfibercomposite.htm>.
- [8] F. Aqilah, M. Islami, F. Juretic, J. Guerrero, D. Wood, and F. Nasir Ani, "Study of mesh quality improvement for CFD analysis of an airfoil," *IJUM Engineering Journal*, vol. 19, pp. 203–212, 2018.
- [9] A. Abdelmoula and J. Rauleder, "Aerodynamic performance of morphed camber rotor airfoils," *AIAA Scitech 2019 Forum*, pp. 1–15, 2019.
- [10] L. Dadone, "US Army Helicopter Design Datcom Volume 1. Airfoils. No. D210-11097-1," *US Army and Mobility R & D Laboratory*, pp. 168–176, 1976.
- [11] Z. Hashin, "Failure criteria for unidirectional fiber composites," *Journal of Applied Mechanics, Transactions ASME*, vol. 47, pp. 329–334, 1980, ISSN: 15289036.
- [12] A. N. Pettitt and M. A. Stephens, "The kolmogorov-smirnov goodness-of-fit statistic with discrete and grouped data," *Technometrics*, vol. 19, pp. 205–210, 1977, ISSN: 15372723.
- [13] C. Kassapoglou, *Design and Analysis of Composite Structures: With Applications to Aerospace Structures, 2nd Edition*. Wiley, 2013, ISBN: 9781118536940.

- [14] J. Kupski, D. Zarouchas, and S. Teixeira de Freitas, "Thin-plyies in adhesively bonded carbon fiber reinforced polymers," *Composites Part B: Engineering*, vol. 184, p. 107 627, 2020, ISSN: 13598368.
- [15] S. Gudmundsson, *General Aviation Aircraft Design: Applied Methods and Procedures*. Butterworth-Heinemann, 2013, ISBN: 9780123973290.
- [16] J. Cahill, "Summary of section data on trailing-edge high lift devices, naca r-938," 1949.

4

ACTIVE MORPHING SYSTEM DESIGN

The hardest choices in life aren't between what's right and what's wrong but between what's right and what's best.

Jamie Ford

Now that the morphing skin is characterized, the opportunities to build a morphing system around it are explored. This chapter discusses the design of the active system, which is followed by the design of the passive system in the next chapter.

For any actuation system to be designed, the requirements play a critical role which is presented in Sec. 4.3. This is followed by Sec. 4.2, where a comparison is presented for the potential off-the-shelf actuators. Section 4.3 presents an account of piezoelectric actuators which are considered appropriate for the present active morphing system. It also explains the selection procedure for the demonstrators for the wind tunnel and whirl tower tests. Section 4.4 explains the complete actuation mechanism designed in conjunction with the selected actuators and the associated kinematics.

4.1. ACTUATION SYSTEM REQUIREMENTS

4

The TRIC concept introduced in Chap. 2 was primarily envisaged for a fixed-wing aircraft. It consists mainly of two primary components: a compliant flap, maintaining its shape under the given load conditions, and an actuation system that can morph the skin when required. For the finalization of the design for rotorcraft, various requirements, including size, frequency, force, weight, voltage input, control system, capital cost, and maintenance cost, have to be considered. The force requirement can also determine the number of actuators (and weight) required for a particular flap length and operational condition. However, the present work is mainly focused on developing a morphing system based on three key requirements, i.e., size, frequency, and the required actuation force. The other requirements are also important and must be evaluated before the design finalization but are outside the scope of the present thesis.

The first key requirement important for the actuators for rotorcraft is size. In the case of its initial concept [1] for fixed-wing aircraft, servo motors (actuators) are housed inside the trailing edge and leading edge volumes, and the appropriate mechanism to change the wing camber is built accordingly. While considering a similar solution for rotor blades, it is important to note that the rotor blades are generally thin, and practically, it is highly improbable to house any actuator inside the limited volume available in the trailing edge section of the rotor blade. This limitation is illustrated in Figure 4.1 by comparing the two airfoil sections, i.e., the airfoil used in the case of fixed-wing aircraft (chord length of $c = 600$ mm) [1] and the airfoil of the Bo105 blade (NACA 23012 with a chord length of $c = 270$ mm). The illustration in Figure 4.1 helps to understand the volume constraints in a blade as compared to the fixed-wing aircraft. This does not imply that accommodating an actuator inside a fixed-wing aircraft is easier, as it depends on loads, operational requirements, and other factors discussed earlier. However, in the author's opinion, the volume available inside the blade structure is more critical for rotorcraft as the options are limited compared to fixed-wing aircraft.

The second key requirement that is solely applicable to a rotorcraft is the high actuation frequency, especially when reduction in noise and vibration are also required. The main rotor operational range, depending on the helicopter, is usually between 320 and 500 RPM [2]. Keeping rotor RPM in perspective, the frequency of morphing actuation is highly dependent on the desired goal, with performance/power benefits coming from quasi-static to 2/rev inputs (8.6 Hz) [3], vibration reduction from 3/rev (34 Hz) control inputs, and noise mitigation from 5/rev (57 Hz) control inputs [4]. From a pure design

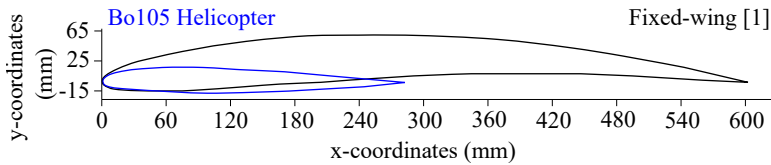


Figure 4.1: Illustration of comparison between the airfoil sections.

perspective, the selected actuator should ideally fulfil all these requirements.

The third key requirement is the force required for actuation. The maximum actuator force or torque determines the type and the number of actuators required to morph a flap of a certain span to the required deflection angle. The actuation force largely depends on the type of rotorcraft and its operating envelope.

4.2. ACTUATOR CONSIDERATIONS

To reduce the uncertainties and complexities of the overall solution, the present work aims to design a morphing solution with conventional components, including the skin and the actuation mechanism. This approach also gives the opportunity to explore the off-the-shelf components. The discussion in the preceding section indicates that the three important requirements at the preliminary design phase are the size of actuators, the operating frequencies, and the force or torque. In terms of actuation options, linear actuators ^{1,2,3,4}, Amplified Piezoelectric Actuator (APA) ⁵, and servo motors ^{6,7} are considered potential candidates for the active morphing concept. After doing a technology scan, the important aspects related to the different actuation options are identified and are presented in Tab. 4.1.

¹<https://www.actuonix.com/>

²<https://www.regner.es>

³<https://www.physikinstrumente.nl/en/>

⁴<https://microlinearactuator.com/>

⁵<https://www.cedrat-technologies.com/en/index.html>

⁶<https://mks-servo.com/HBL6625>

⁷<https://hitecrd.com/>

Actuator Type	Pros	Cons
Linear Actuators	<ul style="list-style-type: none"> • Light weight (60-170 g). • Higher stroke length (17-100 mm). • Simple control system. • Inexpensive. • Low energy consumption. 	<ul style="list-style-type: none"> • Lower operating speeds (1.5-25 mm/s). • Inherent delay in response. • Lower actuation force (more number of actuators required per unit length). • Mechanical backlash (0.2 mm max).
Servo Motors	<ul style="list-style-type: none"> • Light weight (28-100 g). • Medium to high stall torque (44 kg-cm max). • Simple controls system. • Inexpensive. • Low energy consumption. 	<ul style="list-style-type: none"> • Mechanical amplification required. • Lower to medium operating speed (0.11-0.17 sec/60°).
Amplified Piezo-electric Actuators (APA)	<ul style="list-style-type: none"> • Higher forces (18-1400N). • Higher operating frequencies. (Blocked-free resonance: (18-2100 Hz) • Compact. 	<ul style="list-style-type: none"> • Relatively heavy (18-650 g). • Limited stroke lengths (0.12-1.72 mm). • Expensive. • High energy consumption.

Table 4.1: Actuator options considered.

4.3. ACTUATOR SELECTION

In Sec. , it is mentioned that actuation force, frequency and size are the key requirements considered in this work. The data presented in Tab. 4.1 indicates that linear actuators are not suitable for the present case because of low operating speeds, delay in response, and backlash. Servo motors, on the other hand, appear to be a viable option at first sight but are also restricted by the need for amplification and operating speeds. APA presents

good options in terms of force and operating frequencies. However, APA offers limited stroke lengths as compared to servo motors and linear actuators.

It has to be noted that an important factor for the actuator selection for rotorcraft is the influence of the apparent centrifugal forces, which have to be considered in addition to the aerodynamic forces acting on the flap. These centrifugal forces are substantial, 10 times or more than the lift force [5], and the actuation system design must ensure to minimize their effect. Hence, an actuator that is suitable for the fixed-wing aircraft might not work in the case of the rotorcraft, even if the flap is subjected to similar aerodynamic loads. Due to these reasons, the author was unable to find a reference for a flap system in rotorcraft where servo motors or linear actuators are used. On the other hand, virtually all of the research efforts focusing on rotor trailing edge flaps for vibration reduction have used actuators constructed from piezoelectric material to deflect the flaps because these actuators are solid-state, compact, and can produce the required force at high-frequency [6]. However, as mentioned earlier, since the stroke of the piezoelectric actuators is limited, mechanical amplification is required, which adds to the complexity and can result in significant mechanical losses. In this case, actuators similar to APA present an attractive option since the amplification is embedded in the actuator.

In APA, the outer shell is the main reason for the relatively higher amplification [7]. In addition, these shells have the potential of further weight reduction by using composite materials rather than steel [8]. This is indicative of the fact that such actuators can also be customized if deemed necessary. Although the actuator strokes are still limited in such actuators even after embedded amplification, this limitation can be overcome by coupling the actuators in series [9] as shown in Fig. 4.2. Such an arrangement increases the actuator stroke by a factor equal to the number of actuators coupled in series while keeping the force constant. If the purpose is to increase the force without affecting the stroke, the actuators are coupled in parallel.

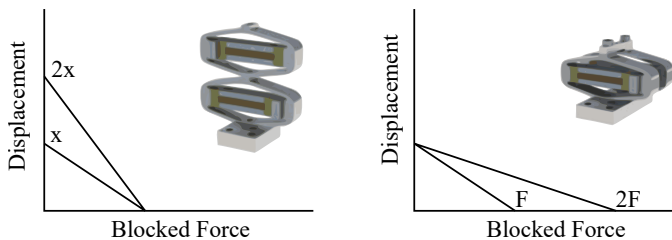


Figure 4.2: Actuators in series and parallel.

Based on the aforementioned discussion and the data in Tab. 4.1 APA is preferred for the present study. The operating frequencies of the APA are sufficient to fulfil the actuation requirements beyond $2/\text{rev}$, which is useful for noise and vibration reduction. It is pertinent to mention here that these actuators have been used in the rotorcraft application in the past [10], [11], and in Micro Air Vehicle (MAV) [12].

The force, displacement, and voltage relationship of the amplified piezoelectric actuators is vital for their actuation and is given by the characteristic equation Eq. 4.1 [13]. This equation can be used to determine the ideal stroke length by using the estimated force magnitude from the numerical analysis. In addition, the same equation can also

be used to obtain the actuation force corresponding to the stroke length obtained experimentally.

$$\frac{F}{F_{max}} + \frac{X}{X_{max}} = \frac{V}{V_{max}} \quad (4.1)$$

where V_{max} is the maximum permissible voltage, V is the supplied voltage, F_{max} is the maximum blocked force, F is the applied blocked force, X_{max} is the maximum stroke, and X is the stroke at supplied voltage.

4.3.1. SELECTION PROCEDURE FOR APA

The selection procedure described here is carried out keeping in mind the particular requirements and loading conditions specific to the two demonstrators built for wind tunnel testing and whirl tower testing. An explanation of the development of these demonstrators is given in Chap. 6. In the case of the wind tunnel demonstrator, both the aerodynamic and elastic loads are considered, and the required actuator forces are determined that can result in a flap deflection of 6° to 8° following the analysis scheme presented in Chap. 3. However, the whirl tower demonstrator is designed with the intention of testing under centrifugal loads only. For this reason, only the elastic loads due to the flap are considered for the actuator selection in this case. For the evaluation of the actuation force, the flap span of the wind tunnel test demonstrator (having a length of 1 m) is considered to be 990 mm. This span is selected mainly because it allows wind tunnel testing at most facilities. It also gives the opportunity to use two actuation points for morphing. For the whirl tower demonstrator, the flap span is taken as 200 mm, which is approximately equal to the length of the potential actuators. This flap span is kept to 4% of rotor radius corresponding to the minimum value of flap span used in the studies for helicopter vibration reduction [14]. It also reduces the elastic loads and allows maximum deflection angles for the selected actuator.

The force required and the stroke length against maximum loads considered for the two demonstrators are highlighted in Fig. 4.3. The required actuation force in each case is calculated by using the FEA approach discussed in Chap. 3. By using this force in Eq. 4.1, the corresponding stroke length is obtained. Figure 4.3 shows the design points obtained as a result of the design study at velocities of 30 m/s and 15 m/s, expected during the wind tunnel test. Similarly, for the whirl tower test, it shows the point where maximum force to deflect the flap (obtained numerically) is indicated. The data points in Fig. 4.3 help to identify the operating range of the actuators under different loading conditions. For instance, in the case of the wind tunnel test at $V = 30$ m/s, it is clear that the flap deflection angle will be lower due to a limited stroke length at stall conditions corresponding to 14° . This shows that at 30 m/s, the test has to be carried out at a considerably lower angle of attack to obtain the same deflections as mentioned for $V = 15$ m/s and $\alpha = 10^\circ$.

Based on the aforementioned analyses, several actuators provided by CEDRAT Technologies [9] are considered as shown in Fig. 4.4. In this figure, the bubble size represents the weight of the actuators.

The topmost (red) bubble shows APA 1500L connected in series (to double the stroke length) as the selected option to test the active TRIC concept. The main characteristics

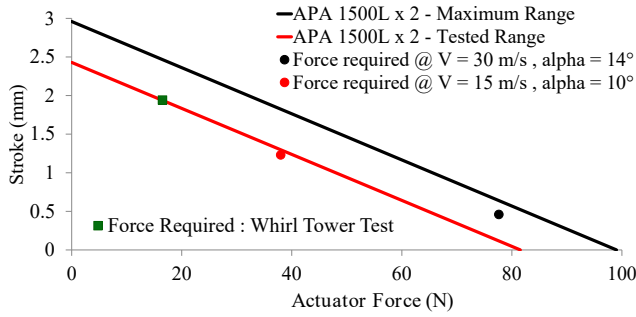


Figure 4.3: Required forces and operating range of APA 1500L.

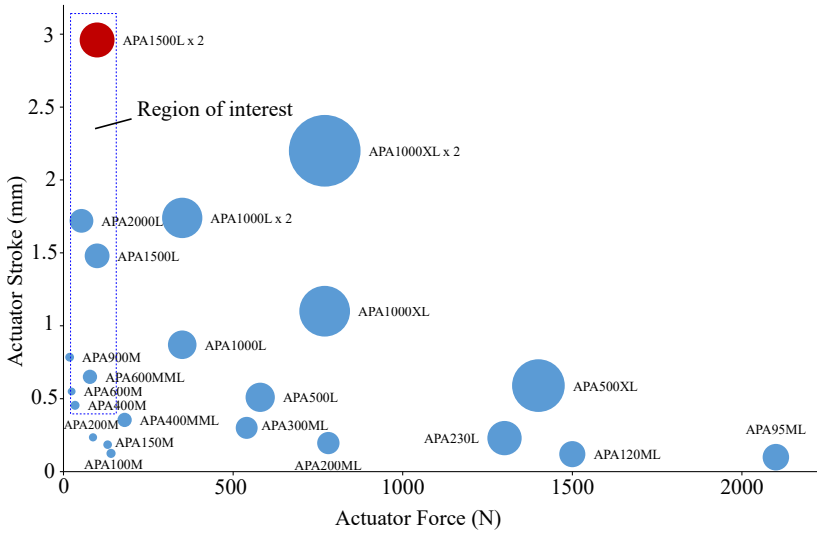


Figure 4.4: APA actuators from CEDRAT [9] indicating force, stroke and weight.

of this actuator are shown in Tab. 4.2.

Parameter	Value	Unit
Nominal stroke	1480	μm
Blocked force	99	N
Blocked-free resonance frequency	135	Hz
Voltage range	-20 .. +150	V
Stiffness	0.0669	$\text{N}/\mu\text{m}$
Mass	143	grams
Force/Volt	0.588	N/V

Table 4.2: Characteristics of APA 1500L [9]

4.4. ACTUATION MECHANISM DESIGN

As mentioned earlier, the rotor blades are subjected to enormous centrifugal forces. The centrifugal force acts through a line that passes through the centre of rotation (COR) and centre of gravity (CG) of mass m as shown in Fig. 4.5. Considering the scope of the present work and the testing on the whirl tower setup, the effect of the flap angle and the lead-lag angle are not taken into account.

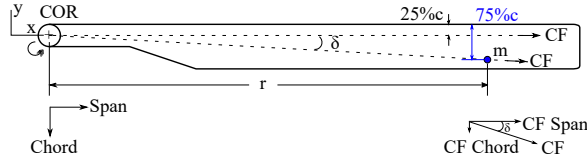


Figure 4.5: Centrifugal force acting on the blade.

When a blade rotates, a mass m placed at a distance r from the COR experiences a centrifugal force, which is represented by the following equation:

$$CF = mr\omega^2 \quad (4.2)$$

where CF is the centrifugal force, m is the mass of the component, and r is the radius of the CG of the component. Although mass on the 25% chord line would experience only a spanwise centrifugal force, any chordwise offset results in both spanwise and chordwise components of the centrifugal force [15] as shown in Eq. 4.3 and Eq. 4.4.

$$CF_{span} = CF \cos(\delta) \quad (4.3)$$

$$CF_{chord} = CF \sin(\delta) \quad (4.4)$$

where δ is the angle corresponding to the spanwise and chordwise components of the centrifugal force acting on mass m . Both the flap and the actuators experience the centrifugal force when mounted at a specific distance from the COR. Considering the line of action of the centrifugal force and the fact that the Aspect Ratio (AR) of the blades is relatively high, the chordwise component is small compared to the spanwise component. Nevertheless, depending on the magnitude of the parameters in Eq. 4.2 and the location of m , the chordwise component may still be considerable. This difference in magnitudes can be examined by considering an extreme case. For the Bo105 helicopter blade rotating at 44.4 rad/sec, when a mass is placed at $0.9R$ ($R = 4.9m$) from COR at 75% chord line as shown in Fig. 4.5, the value of centrifugal force turns out to be 8,680 N/kg. However, the chordwise component turns out to be only 266 N/kg.

It is clear that the chordwise component of centrifugal force would affect the actuation power. Thus, placing the actuation system so that its CG lies on or close to the COR in the chordwise direction would significantly reduce the chordwise component of the centrifugal force. However, the spanwise component of the centrifugal force must

be managed so that its effect on the actuation system is minimized. Due to this reason, the actuation system is intentionally designed to have its CG such that the chordwise component of centrifugal force is minimized to the extent that it can be neglected. In addition, with reference to Eq. 4.2, for the thin flap made of composite, the longitudinal (spanwise) component is also negligible if the skin is thin, light-weight, and appropriately constrained to the rigid structure. The effect of this component on the actuator and associated mechanics can be minimized by having additional supports. Two thin blades made of steel and teflon pads are introduced in the assembly, as shown in Fig. 4.6. The blades and the teflon supports react to the centrifugal loads to prevent the actuation system from bending due to these loads.

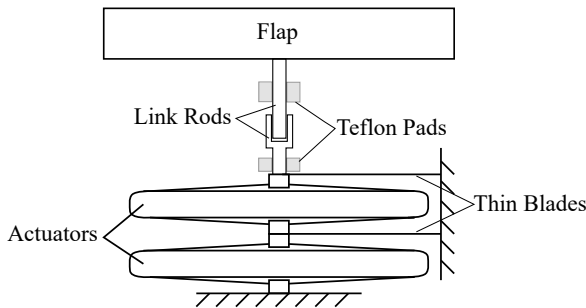


Figure 4.6: Top view of the proposed mechanics.

The effect of the thin blades on the force and stroke is examined by an analysis in Abaqus and shown in Fig. 4.7. In this case, the blades are deflected by applying a unit force, and the resulting tip deflection is observed. From this analysis, the force/stroke for the blades is noted as 1.6 N/mm. This analysis shows that for a maximum deflection, the force consumed by the blades is approximately 4% of the available blocked force from APA 1500L.

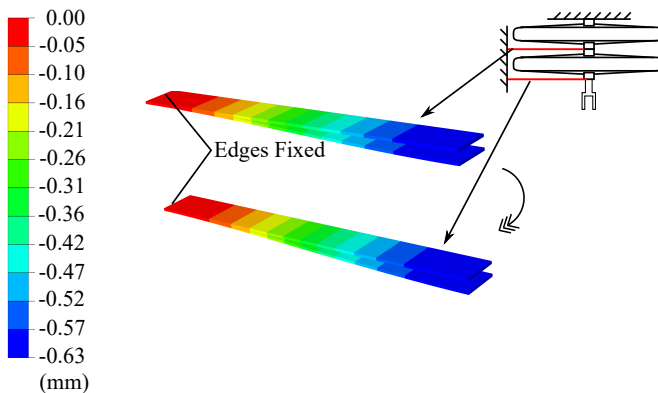


Figure 4.7: Deflection of blades under a unit force.

The functional design of the actuation system is shown in Fig. 4.8. Two APA actuators (4) are mechanically attached in series and fixed to the wingbox (5). The actuators are avoided from being overhung by providing rigid support (9) underneath the rightmost actuator in Fig. 4.8. A link rod (3) is attached to the free side of the actuator (4). A second link rod (2) is attached to the trailing edge flap (1) using a bracket (6) (bonded to the flap's bottom skin), creating a pin joint (7). The two actuators are attached to make another pin joint (8) that gives an additional DOF to accommodate the manufacturing tolerances and subsequent integration issues.

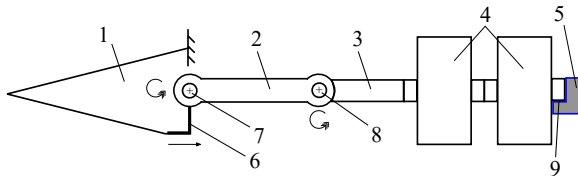


Figure 4.8: Cross-sectional view of the proposed kinematics.

4.5. SUMMARY

In this chapter, detail of the active morphing system design was presented. The actuation system consisted of mainly two components, i.e., a compliant flap and an actuation mechanism that was able to provide the strokes for 6° to 8° flap deflections with frequencies of 7 Hz to 21 Hz corresponding to the Bo105 helicopter. Out of several options considered, amplified piezoelectric actuators with an integrated housing were selected to amplify the stroke produced by the piezoelectric actuators. Based on the aerodynamic loads, these actuators showed the potential to fulfil the requirements of the desired stroke length and actuation frequencies. Mechanical links and stiffeners in the form of thin blades were designed around these actuators to transmit the desired stroke effectively to the morphing flap.

BIBLIOGRAPHY

- [1] N. Werter, J. Sodja, G. Spirlet, and R. De Breuker, "Design and Experiments of a Warp Induced Camber and Twist Morphing Leading and Trailing Edge Device," *24th AIAA/AHS Adaptive Structures Conference*, pp. 1–20, 2016.
- [2] Federal Aviation Administration, "Helicopter Emergencies and Hazards," *Helicopter flying handbook*, pp. 1111–1124, 2012.
- [3] H. Yeo, R. Jain, and B. Jayaraman, "Investigation of rotor vibratory loads of a UH-60A individual blade control system," *Journal of the American Helicopter Society*, vol. 61, 2016, ISSN: 00028711.
- [4] E. R. Booth and M. L. Wilbur, "Acoustic Aspects of Active-Twist Rotor Control," *Journal of the American Helicopter Society*, vol. 49, pp. 3–10, 2004, ISSN: 00028711.
- [5] J. A. J. Bennett, "Rotary-Wing Aircraft Evolution of Present Configurations," pp. 7–9, 1940.
- [6] T. Lee and I. Chopra, "Design of piezostack-driven trailing-edge flap actuator for helicopter rotors," *Smart Materials and Structures*, vol. 10, pp. 15–24, 2001.
- [7] A. Kras, O. Sosnicki, A. Riquer, S. Rowe, and F. Claeysen, "Advantages of Large Piezoelectric Actuators and High Power Drivers for Fatigue and Fretting Test," *Proceedings of 4th International Conference on Fracture Fatigue and Wear*, vol. 6, pp. 1–6, 2015.
- [8] A. Kras, M. Brahim, T. Porchez, C. Bouchet, and F. Claeysen, "Compact, lightweight, and efficient piezo-actuation chain for aeronautical applications," *Proceedings of the 14th International Conference on New Actuators, ACTUATOR 2014*, pp. 23–25, 2014.
- [9] Cedrat, "Products catalogue version 5.1 - cedrat technologies actuator solutions," 2013.
- [10] J. H. Lee, B. Natarajan, W. J. Eun, S. R. Viswamurthy, J. S. Park, T. Kim, and S. J. Shin, "Structural and mechanism design of an active trailing-edge flap blade," *Journal of Mechanical Science and Technology*, vol. 27, pp. 2605–2617, 2013, ISSN: 1738494X.
- [11] P. Leconte and H. Mercier, "Experimental Assessment of an Active Flap Device," 2002.
- [12] D. Schafroth, S. Bouabdallah, C. Bermes, and R. Siegwart, "From the test benches to the first prototype of the muFly micro helicopter," *Journal of Intelligent and Robotic Systems: Theory and Applications*, vol. 54, pp. 245–260, 2009, ISSN: 09210296.
- [13] U. Visconti, W. J. Eun, J. S. Sim, S. W. Lee, and S. J. Shin, "Design improvements and flap deflection evaluations with considering centrifugal load on active trailing edge flap," *Aircraft Engineering and Aerospace Technology*, vol. 91, pp. 10–19, 2018, ISSN: 17488842.

- [14] R. Mallick, R. Ganguli, and M. S. Bhat, "Robust design of multiple trailing edge flaps for helicopter vibration reduction: A multi-objective bat algorithm approach," *Engineering Optimization*, vol. 47, no. 9, pp. 1243–1263, 2015.
- [15] P. Moser, S. Barbarino, and F. Gandhi, "Helicopter Rotor-Blade Chord Extension Morphing Using a Centrifugally Actuated Von Mises Truss," *Journal of Aircraft*, vol. 51, pp. 1422–1431, 2014, ISSN: 0021-8669.

5

PASSIVE MORPHING SYSTEM DESIGN

The simpler, the better. Complications lead to multiplicative chains of unanticipated effects.

Nassim Nicholas Taleb

This chapter introduces the design of a passive camber morphing system driven by centrifugal forces. This system does not require external energy to control the morphing flap but utilizes the changes in rotor speed to deform the trailing edge. The chapter starts with a brief discussion on the performance benefits of the passive concept in relation to the VSR in Sec. 5.1.

The design process starts with the key considerations presented in Sec. 5.2. A design methodology is presented in which the passive concept is introduced, and the key design parameters are discussed, followed by the proposed concept to achieve the passive morphing. After having the complete problem definition, Sec. 5.3 discusses the approach to solve the overall design problem and obtain the required design parameters in the end. Finally, the complete working principle of the passive concept is explained in Sec. 5.4 based on the discussion in the preceding sections.

5.1. SIGNIFICANCE OF PASSIVE MORPHING

Before discussing the design requirements for a passive system and understanding the passive design concept and its implementation, it is important to show the significance of the passive morphing system for rotorcraft performance and how the requirements for its design are generated. For this purpose, a numerical tool called Helicopter Conceptual Design and Performance Analysis Tool (HOPLITE) developed by Vidyarthi et al. [1] is utilized, which is based on the Blade Element Theory to model the main rotor and accounts for changes in the rotor blade geometry, including the camber morphing. The induced velocity over the disk is calculated using Glauert's formulations [2]. This tool combines various low-fidelity methods, which are described by Vidyarthi et al. [1], such that quick design assessments can be performed for aerodynamic efficiency, power consumption, and engine emissions. On the basis of the aforementioned analysis tool, a detailed numerical analysis for both the active and passive morphing concepts in terms of performance benefits is presented in [3]. However, a brief account of the key performance benefits is highlighted in this section to indicate the importance of the passive concept.

As mentioned in Chap. 2, the passive morphing concepts are driven by the apparent centrifugal forces experienced by a rotor. The variation in rotor RPM can be used to change the centrifugal forces so that the morphing can be achieved in a controlled manner. Considering the Bo105 rotor as the baseline rotor, two flight conditions are studied, namely, hover at sea level and hover at an altitude of 2,000 m. In terms of performance parameters, collective pitch normalized with rotor thrust coefficient $\frac{\theta_0}{C_T}$ and rotor power coefficient normalized with thrust coefficient $\frac{C_P}{C_T}$ are used [3]. In the study, the flap is placed between 70% and 90% of the rotor radius. This is because the dynamic pressure around this location on the rotor blade keeps the morphing flap effectiveness at a high level resulting in a substantial impact on the local aerodynamics of the rotor when the flap is actuated. The rotor RPM is changed from 100% to 90%, and the flap deflections are varied between 0° and 6° for each case. The weight of the aircraft is taken as 2200 kg, approximately 90% of the maximum take-off weight [4]. The outcome of the performance analysis is presented in Fig. 5.1.

Figure 5.1a and 5.1b show respectively the power and collective pitch requirements

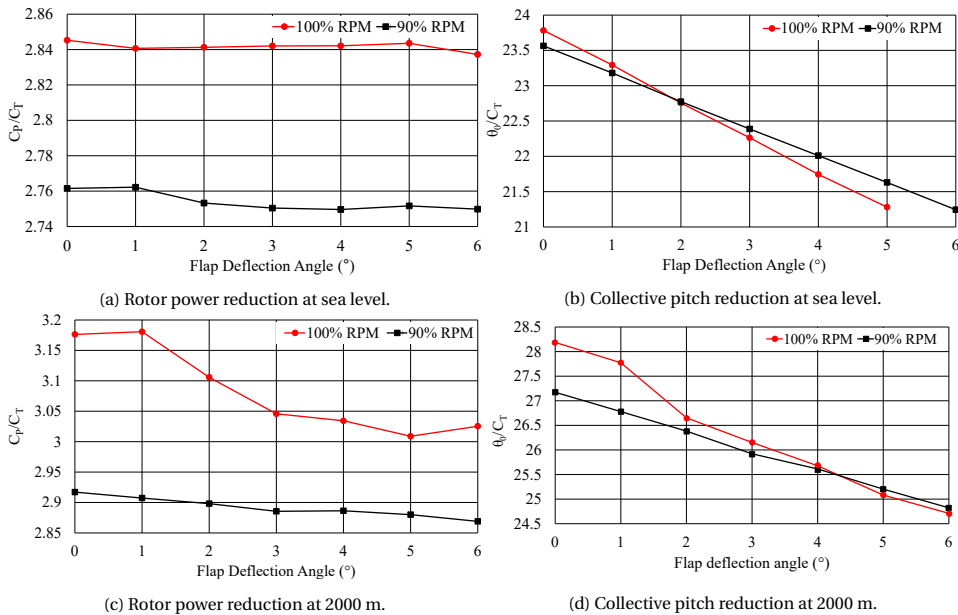


Figure 5.1: Power and collective pitch reductions with passive morphing.

to trim the rotor at sea-level. It can be seen that power reduction is mainly linked to the rotor RPM and are in line with the studies found in literature [5, 6]. It is also observed that slowing the rotor has more influence than camber morphing. However, the reduction in collective is around 10% which is quite significant and is an indirect measurement of pilot control authority [3]. For the edge of the flight envelope case, such as hover at 2000 m, rotor morphing has shown to be more useful [7]. Figure 5.1c and Fig. 5.1d shows a greater performance benefit when the RPM reduction is coupled with passive morphing. A 12% and 8% reduction in collective pitch and power required to trim the rotor are observed, respectively.

It is clear from the aforementioned study that passive morphing has potential benefits when coupled with a variable speed rotor. Passive morphing flap reduces the collective pitch requirement in a variable rotor speed rotorcraft, which increases the pilot control authority and can potentially extend the flight envelope. More details on the performance benefits associated with the passive morphing concept are provided in Ref. [3].

5.2. DESIGN METHODOLOGY

As mentioned in the literature review in Chap. 2, passive concepts that are based on the centrifugal forces are mainly developed for rotor blade chord extension or increase in rotor blade span. The passive system envisaged in the present research work is based on the TRIC morphing concept, as mentioned in Chap. 4. To replace an electrical actuator, a mechanical system is required that can perform the same function with the apparent centrifugal forces. In this case, the movement of the flap can be controlled by varying

the rotor RPM.

The performance benefits mentioned in the previous section are achieved with a certain flap size, location, flap deflection angle, and RPM range. All these parameters are considered as input to the design of the passive system. For the Bo105 case, the range of RPM is defined as 90% to 100% [3]. For 100% RPM, the flap is required to stay undeflected or at its baseline position. At a particular value of reduced RPM, for instance, 90% RPM mentioned in the case of Bo105, the flap should deflect downwards to the required angle and maintain its position. Once the operational requirement changes, the RPM is increased back to 100%, and the flap should return to its baseline position. This implies that on the ground, when the rotor is stationary, the flap is also at a deflected position. Hence, the RPM range and the required flap deflection both serve as key design inputs for the passive morphing system.

5.2.1. PROPOSED CONCEPT FOR PASSIVE MORPHING

In the active system, the TRIC concept is actuated using an actuator that requires external energy to operate. The actuator is connected to the bottom surface using a mechanical link rod. The passive concept utilizes the same point for actuating the flap through the apparent centrifugal force F_c . The novel concept [8] presented in this section is based on the operational requirements of the flap discussed in Sec. 5.1 where the morphing flap has to deflect downwards between 100% RPM and 90% RPM. At a given rotational speed, if a mass m , comprising of a spanwise shaft and an extension spring, is placed within the rotor blade at a distance r from the COR, it experiences a centrifugal force normal to the velocity vector v , as shown in Fig. 5.2 and given by Eq. 4.2.

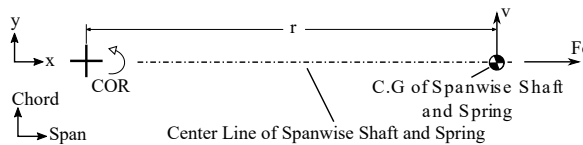


Figure 5.2: Placement of the components w.r.t centrifugal force.

Based on Fig. 5.2, Fig. 5.3 shows a mechanical arrangement in the form of orthogonal shafts. The system of shafts shown in Fig. 5.3 converts the motion introduced by the apparent centrifugal force in the spanwise direction (x_s) to a corresponding movement in the chordwise direction (x_t) for the actuation of the flap. An extension spring with a preload (pL) is attached in line with the spanwise shaft such that any movement in the spanwise shaft causes the spring to extend. The preload in the extension spring ensures that the movement starts when the rotor RPM exceeds the 90% mark. The restoring force of the spring at 100% RPM causes the flap to deflect downwards when the RPM is reduced to 90%. The spanwise shaft (2), linked to the extension spring (4), provides an inclined surface for the chordwise shaft (1) to move. The relative movement of both the shafts is achieved by having rollers attached to the chordwise shaft (1) (not shown in Fig. 5.3) at the interface (6). The placement of the extension spring (4) and spanwise shaft (2) with respect to the overall system is shown in Fig. 5.2. It must be noted that, in principle, the shape of the spanwise shaft (2) at the interface (6) can be tailored for

different flap angles at various RPM.

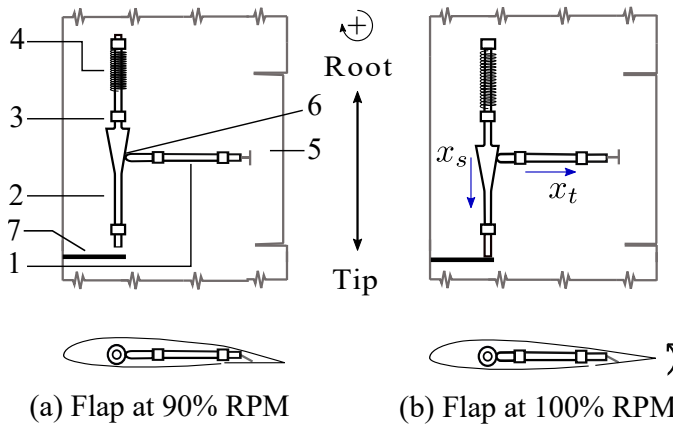


Figure 5.3: Schematic of the passive system.

Figure 5.3 also shows the position of the flap with respect to the desired RPM value. When the rotorcraft is on the ground, and the rotor starts to spin, the flap deflects upwards to attain the undeflected or baseline position at 100% RPM as shown in Fig. 5.3 (b). When the RPM decreases, the flap deflects downwards and attains the required deflection angle at 90% RPM as shown in Fig. 5.3 (a). It must be noted that when the rotorcraft is about to take off, the collective pitch control is used to increase the rotor blade pitch angle. At this stage, the aerodynamic load can cause the flap to deflect upwards beyond its baseline position. To avoid this movement, it is important to have a mechanical end-stop 7 shown in Fig. 5.3 that prevents the movement due to the aerodynamic load. When the flap is required to deflect downwards by the contraction in the extension spring, the reduction in the centrifugal force from 100% RPM to 90% RPM must account for the aerodynamic load in order for the spring to contract as required.

The function of each component shown in Fig. 5.3 is summarized as follows:

1. Chordwise shaft (1) is linked to the trailing edge flap (5) at one end. The other end has roller bearings that are constrained inside the spanwise shaft (2). It is free to slide only along the chordwise direction.
2. Spanwise shaft (2) is placed perpendicular to the chordwise shaft (1), and its axis intersects the axis of the chordwise shaft (1). It provides a path for the roller bearings to move smoothly and also constrain the independent movement of the chordwise shaft (1). It is free to slide only along the spanwise direction.
3. Extension spring (4) has a particular value of pL due to which it does not extend until the apparent centrifugal force exceeds that value as shown in Fig. 5.4. It also enables the flap actuation at the desired RPM. The extension spring (4) is connected to the rotor blade structure at one end, and the other end is fixed to the spanwise shaft (2).

4. Support (3) refers to the mechanical housings for components such as mechanical sleeves that are fixed to the rotor blade structure. This results in constraining the movement of both the shafts in the desired direction while minimizing the friction.
5. Mechanical endstop (7) is attached to the rotor blade structure and limits the movement of the spanwise shaft (2) to ensure that the flap does not deflect upwards beyond its baseline position.

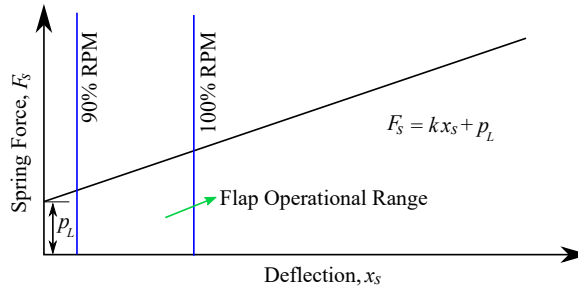


Figure 5.4: Force and displacement relation of an extension spring.

5.2.2. DESIGN PARAMETERS

Based on the above-mentioned discussion, key design parameters are identified and presented in Fig. 5.5. The rotor parameters, which serve as the design inputs, include information such as flap length, flap location, flap chord, flap deflection angle, rotor radius, rotor blade airfoil and maximum RPM.

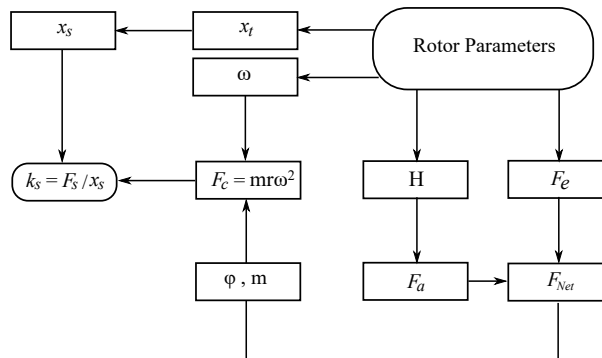


Figure 5.5: Block diagram representing the design parameters.

In a conventional flap with a distinct hinge, the aerodynamic load is the main force and the resulting hinge moment H determines the actuation force F_a . However, in the TRIC morphing flap, the elastic load is also a key design input, and an actuation force F_e is required to compensate it. This elastic load results from the stiffness of the flexible

morphing skin and depends on the size of the flap, its thickness, and material. Therefore, to design a passive system around such a concept, both the elastic and aerodynamic loads must be determined. Once these two loads are known, the net force F_{Net} is calculated against which the centrifugal force has to operate. The other important parameters which are needed to be determined include the stroke or chordwise movement x_t of the bottom skin required for the desired flap deflection β . This chordwise movement is linked to the spanwise movement x_s of the extension spring. The shaft angle φ resolves the net force required to deflect the flap into spanwise and chordwise components. After having all the input parameters identified, the required spring stiffness K_s and the pL of the extension spring can be estimated.

5.3. MATHEMATICAL FORMULATION

The mathematical formulation discussed in the following sub-sections describes the procedure adopted to estimate the required spring stiffness and preload for the passive morphing system.

5.3.1. SCOPE AND ASSUMPTIONS

Figure 5.5 indicates that the design solution for the passive system involves the estimation of the aerodynamic forces and elastic forces, which can be obtained by following the methodology in Chap. 3. However, mathematical formulations presented in this section intend to formulate an analytical tool that can solve the overall design problem quickly and with reasonable accuracy as per the flow chart in Fig. 5.5. Once stiffness and preload of the spring are determined, a higher fidelity analysis can be performed using CFD and FEA before the final selection of the spring.

In the analytical formulation, the actuation force F_e corresponding to the elastic load is based on the classical beam theory [9] and the Classical Laminate Theory (CLT) [10] when composites are used as the flap material. In the case of composites as flap material, balanced and symmetric laminates are considered [11]. A correlation of the F_e obtained with the analytical formulation is established with FEA studies to determine the extent of difference between the two approaches. Correction factors based on the FEA are also determined that are used in the analytical tool for better prediction of actuation force.

For the aerodynamic loads, the methodology is based on thin airfoil theory and blade element theory for hovering, assuming uniform inflow and symmetric, untwisted rotor blades [12].

5.3.2. ELASTIC LOAD ESTIMATION

In the TRIC concept, the bottom skin is connected to the actuation system and translated to deform the top skin. This deformation of the skin can be considered as pure bending of the top skin that is fixed at one end. If the actual trailing edge portion is replaced by a simplified geometry that joins the root and tip of the flap with a straight line, the actual airfoil coordinates of the trailing edge flap show a good match to the simplified geometry. The chord length of the trailing edge flap c_f is taken as 50% of the rotor blade chord length c as shown in Fig. 5.6.

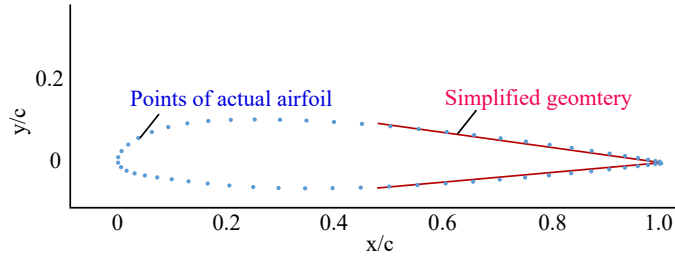


Figure 5.6: Simplified representative shape based on NACA 23102, $c = 270$ mm.

Based on the above-mentioned simplification, F_e can be determined using the bending stiffness of the top skin. For an isotropic material like aluminium, estimating the bending stiffness is straightforward as the modulus of elasticity is known. However, for composites, the bending modulus of elasticity has to be calculated and depends on the material and layup. For this reason, the stiffness matrices $[A]$, $[B]$ and $[D]$ of the laminates are calculated using the CLT as given Eq. 5.1 [13].

$$\begin{aligned}
 A_{ij} &= \sum_{k=1}^n Q_{ij} (z_k - z_{k-1}) \\
 B_{ij} &= \frac{1}{2} \sum_{k=1}^n Q_{ij} (z_k^2 - z_{k-1}^2) \\
 D_{ij} &= \frac{1}{3} \sum_{k=1}^n Q_{ij} (z_k^3 - z_{k-1}^3)
 \end{aligned} \tag{5.1}$$

where $i, j = 1, 2, 6$, n is the total number of plies in the laminate, Q_{ij} are the elements of the stiffness matrix and (z_k, z_{k-1}) are the upper and lower z coordinates of the k^{th} ply as shown in Fig. 5.7 .

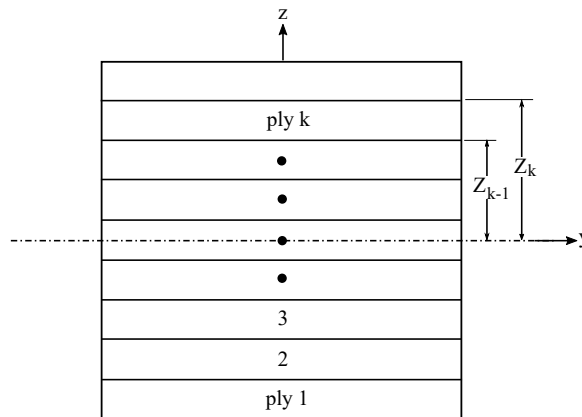


Figure 5.7: Ply numbering system [13].

The expressions for the in-plane forces and moments are given as follows [10]:

$$\begin{Bmatrix} N_x \\ N_y \\ N_{xy} \\ M_x \\ M_y \\ M_{xy} \end{Bmatrix} = \begin{bmatrix} A_{11} & A_{12} & A_{16} & B_{11} & B_{12} & B_{16} \\ A_{12} & A_{22} & A_{26} & B_{12} & B_{22} & B_{26} \\ A_{16} & A_{26} & A_{66} & B_{16} & B_{26} & B_{66} \\ B_{11} & B_{12} & B_{16} & D_{11} & D_{12} & D_{16} \\ B_{12} & B_{22} & B_{26} & D_{12} & D_{22} & D_{26} \\ B_{16} & B_{26} & B_{66} & D_{16} & D_{26} & D_{66} \end{bmatrix} \begin{Bmatrix} \epsilon_x^0 \\ \epsilon_y^0 \\ \gamma_{xy}^0 \\ \kappa_x^0 \\ \kappa_y^0 \\ \kappa_{xy}^0 \end{Bmatrix} \quad (5.2)$$

where A_{ij} are the in-plane stiffnesses that relate the in-plane forces N_x , N_y , N_{xy} , to the in-plane strains ϵ_x^0 , ϵ_y^0 , γ_{xy}^0 . D_{ij} are the bending stiffnesses that relate the moments M_x , M_y , M_{xy} , to the curvatures κ_x^0 , κ_y^0 , κ_{xy}^0 . B_{ij} are the in-plane-out-of-plane coupling stiffnesses that relate the in-plane forces N_x , N_y , N_{xy} to the curvatures κ_x^0 , κ_y^0 , κ_{xy}^0 and the moments M_x , M_y , M_{xy} , to the in-plane strains ϵ_x^0 , ϵ_y^0 , γ_{xy}^0 .

SIMPLE CANTILEVER BEAM CASE

Before carrying out the analysis based on the simplified shape of the trailing edge, boundary conditions in the FEA are determined for a simple cantilever beam shown in Fig. 5.10. This is especially important for the composite skins, which is the primary candidate for the TRIC concept as discussed in Chap. 3. To compare the analytical and FEA models, the beam width is taken as $1/10^{th}$ of the beam length. Considering NACA 23012 and having a rotor blade chord length $c = 270$ mm, the flap chord length is taken to be 25% of the rotor blade chord.

For a laminate, the correct boundary conditions should take into account the situations where the D_{16} and D_{26} terms in the ABD matrix calculated using the CLT are not zero. As shown in Fig. 5.8, U1, U2, U3 are the translational DOF, and UR1, UR2 and UR3 are the rotal DOF with respect to the prescribed coordinate system. In the FEM, the middle node at the root is constrained in all DOF, and only the rotation about UR3 is permitted. For the remaining nodes on the root, U3, UR2, and UR3 are constrained as shown in Fig. 5.8.

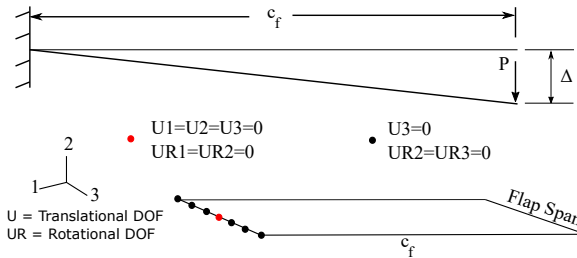


Figure 5.8: Boundary conditions and deflection of the cantilever beam.

Now using the CLT, the bending modulus of elasticity of the laminate is calculated by using the following expression [10]:

$$E_b = \frac{12}{h^3 d_{11}} \quad (5.3)$$

where E_b is the bending modulus of elasticity of skin, d_{11} is the (4,4) element obtained from ABD matrix inversion and h is the thickness of the laminate. The bending modulus of elasticity of the skin is used in the beam theory to obtain the tip deflection Δ by using the following equation [9]:

$$\Delta = \frac{PL^3}{3E_b I} \quad (5.4)$$

where P is the applied load, I is the moment of inertia, and $E_b I$ is the bending stiffness of the skin in $\text{N}\cdot\text{mm}^2$. For the prepreg material AS4, the material properties are given in Tab. 3.3 in Chap. 3. For this case, the difference in the tip deflections obtained using both FEA and analytical formulation is shown in Fig. 5.9 where the difference is mostly less than 5%.

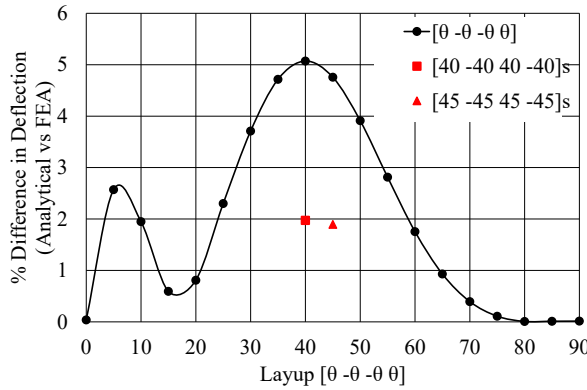


Figure 5.9: Difference in tip deflection between FEA and analytical formulation for different layups.

The tip deflections obtained using analytical formulation correspond well to the FEA result. The difference is generally higher in layups where the relative magnitude of D_{16} and D_{26} terms are higher as compared to the D_{11} term. However, increasing the number of plies reduces the error considerably. This is indicated in Fig. 5.9 for the case of two layups that resulted in the highest difference, i.e., $[40/-40]_s$ and $[45/-45]_s$. When the number of layers in these two layups is doubled, and the length-to-width ratio is kept the same, the percentage difference in deflection is reduced by approximately 60%. Further investigation on these results is not performed as it is considered beyond the scope of the present work.

SIMPLIFIED TRAILING-EDGE SHAPE CASE

For the case of simplified shape, the beam formulation can also work considering the cantilever beam subjected to a moment as shown in Fig. 5.10.

The bending modulus of elasticity of the skin obtained in Eq. 5.3 is used in the following expression to obtain the tip deflection of the flap [9]:

$$\Delta = \frac{ML^2}{2E_b I} \quad (5.5)$$

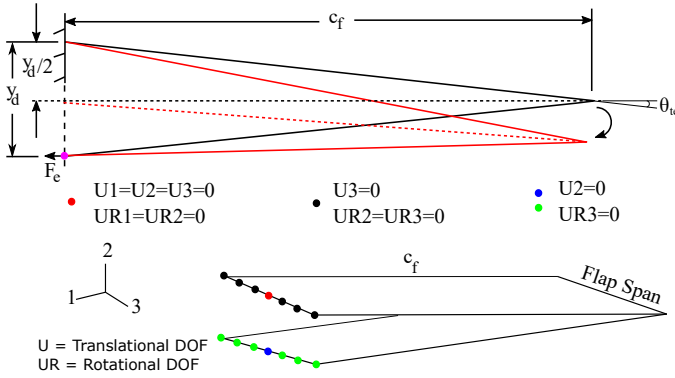


Figure 5.10: Boundary conditions and deflection of the simplified trailing edge shape.

where M is the moment due to the force applied at the prescribed distance $y_d/2$. Referring to Fig. 5.10, Eq. 5.5 takes the following form for the analytical formulation:

$$\Delta = \left(F_e \left(\frac{y_d}{2} \cos(\theta_{te}) \right) \right) \left(\frac{c_f}{\cos(\theta_{te})} \right)^2 \frac{1}{2E_b I} \tag{5.6}$$

For calculating F_e , Eq. 5.6 takes the following form:

$$F_e = \frac{4 \cos(\theta_{te}) \Delta E_b I}{c_f^2 y_d} \tag{5.7}$$

where F_e is the force required for the deflection Δ and θ_{te} is the angle created between the line representing the top surface and the centerline as shown in Fig. 5.10.

For the FEM used here and in all the subsequent cases, a trailing edge portion of 6 mm span and 65 mm length is subjected to a translation of 1 mm, and the corresponding reaction force is noted at the prescribed node. In addition, the point of constrain on the top skin and the point of actuation on the bottom skin occur on the same line as shown in Fig. 5.10

Given the boundary condition specified in Fig. 5.10, two important factors are considered before establishing a correlation between the analytical formulation and FEA of the simplified shape. Firstly, there is an effect of the stiffness of the bottom skin on the tip deflection when a force is applied, as shown in Fig. 5.10. Secondly, unlike the simplified case, the actual boundary conditions of the bottom skin in the TRIC concept ensure translation with $UR3=0$. To analyze this problem, an isotropic material is considered first. In the FEM, the top skin is considered to be aluminium, while the bottom skin is artificially stiffened by using an infinitely high value of modulus of elasticity E . By having $UR3 \neq 0$, the deflection obtained in FEA is used as an input for the analytical formulation to estimate the bending moment, which subsequently results in estimating the required force F_e using Eq. 5.7. In this case, the force F_e estimated by the analytical formulation matches well to the force in FEA as shown in Fig. 5.11a. The process is repeated by varying the skin thickness and calculating the corresponding forces. It can be seen from

Fig. 5.11b that considering an infinitely stiff bottom skin and having $UR3 \neq 0$, the error is very small when the reaction force from FEA is compared to the corresponding force in the analytical formulation. In addition, there is a negligible effect of thickness change in the error.

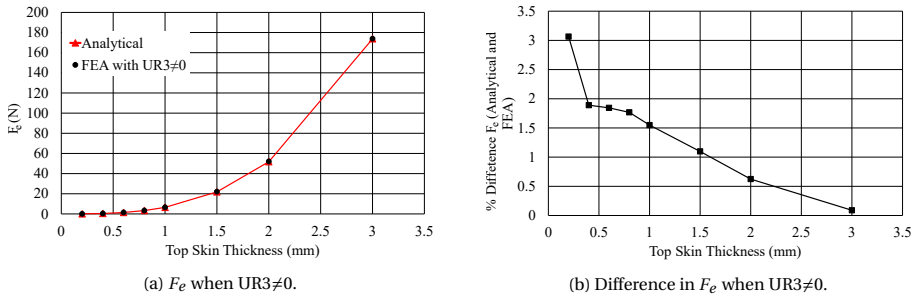


Figure 5.11: F_e calculated when bottom skin is considered infinitely stiff.

5

As mentioned earlier, the actual boundary condition for the bottom surface shown in Fig. 5.6 also restricts the rotation, i.e., $UR3=0$, resulting in a significant increase in the reaction force. The next analysis shows the influence of the change in boundary conditions in FEA and the difference with analytical prediction in Fig. 5.12a. It is clear that the reaction force increases substantially by restricting $UR3=0$. Furthermore, when F_e is calculated with $UR3=0$ in FEA and with analytical formulation, an approximately constant ratio, defined in Eq. 5.8, is observed throughout the thickness range as shown in Fig. 5.12b. The outcome of this analysis indicates that to include the effect of actual boundary conditions in the analytical model, a correction factor, kf as shown in Eq. 5.8 can be used for the case of isotropic materials.

$$kf = \frac{F_e(FEA)}{F_e(Analytical)} \quad (5.8)$$

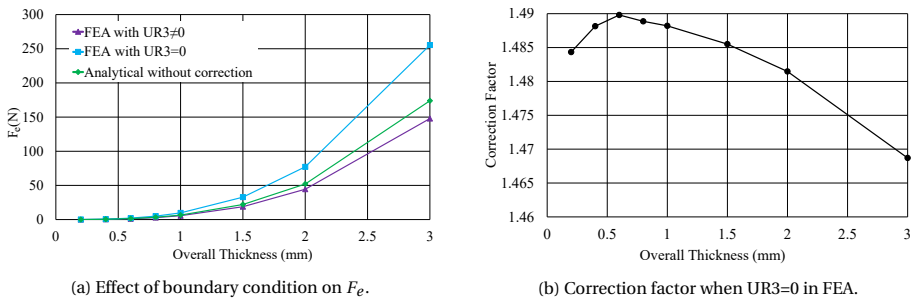


Figure 5.12: RF calculated for aluminum.

For the case of composite materials, the calculation of the correction factor is not straightforward because of the presence of D_{16} and D_{26} terms discussed earlier. However, for balanced and symmetric laminates, a sufficient number of plies ensures an ap-

proximately constant correction factor. In Fig. 5.13a, bending modulus of elasticity of the skin, E_b is plotted for various laminates by changing the ply angles. As noted in Fig. 5.13a, the variation in E_b is more pronounced in the layups where the ply angle changes between 5° and 50° . In addition, when the number of plies increases, the variation in E_b tends to reduce. Subsequently, the difference in kf is also reduced, establishing an approximately constant correction factor as shown in Fig. 5.13b. This analysis shows that the correction factor kf can also be used for composite materials. However, depending on the layup, the deviation in the force calculated can be higher as compared to the force calculated in the FEA.

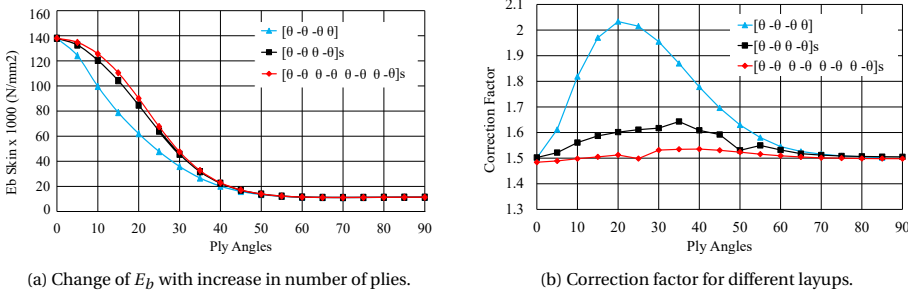


Figure 5.13: E_b and correction factors for composites.

In order to generalize the aforementioned approach, the effect of change of flap geometry on the correction factor must also be considered. The 2D simplified shape in Fig. 5.6 can be mathematically represented by the ratio \mathcal{R} of chord length c_f and the distance y_d as shown in Eq. 5.9. For different values of \mathcal{R} and materials, RF is calculated from FEA by assuming $UR3 \neq 0$ and $UR3 = 0$ as shown in Fig. 5.14 and the bottom skin subjected to a translation of 1 mm. The properties of the materials used are the same as mentioned in Tab. 3.3 in Chap. 3.

$$\mathcal{R} = \frac{c_f}{d_y} \tag{5.9}$$

It can be observed from Fig. 5.14 that RF values tend to increase as the \mathcal{R} increases. However, the correction factor for all cases remains the same, irrespective of the material and aspect ratio as shown in Fig. 5.15. As mentioned earlier, the correction factor presented in Fig. 5.14 assumes the point of constrain on the top skin and the point of actuation on the bottom skin to be in line with each other.

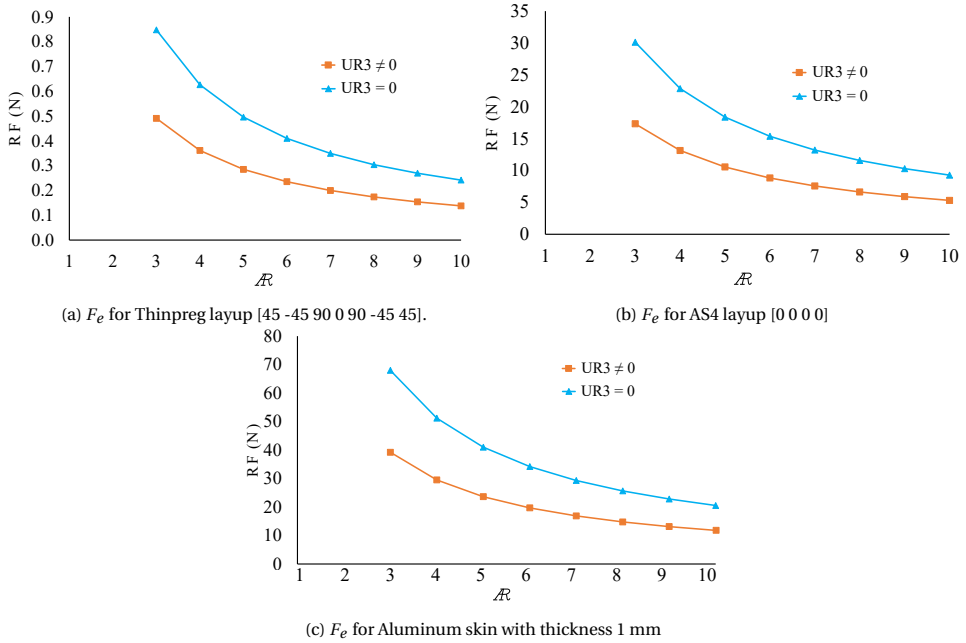
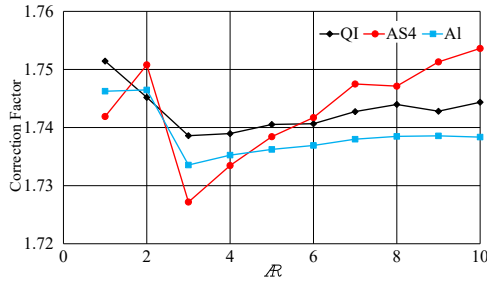
Figure 5.14: F_e for composite and aluminum.

Figure 5.15: Correction factor as a function of aspect ratio.

5.3.3. AERODYNAMIC LOAD ESTIMATION

In order to calculate the force required to deflect the flap under the influence of aerodynamic loading, the flap hinge moment (H) is estimated based on the approach presented by Walz et al. [12]. The blade geometry is depicted in Fig. 5.16. The morphing flap is considered to be a conventional flap with a pseudo hinge. The aerodynamic forces are obtained by estimating the hinge moment on the flap about the pseudo hinge located at a specified distance as shown in Fig. 5.17. The hinge moment coefficient can be given as the summation of the moment due to the airfoil lift coefficient shown in Eq. 5.10:

$$C_h = C_l \frac{dC_h}{dC_l} + \beta \frac{dC_h}{d\beta} \quad (5.10)$$

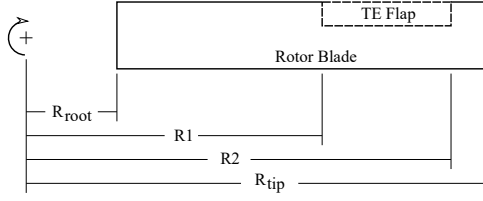


Figure 5.16: Representation of geometric parameters of the rotor blade.

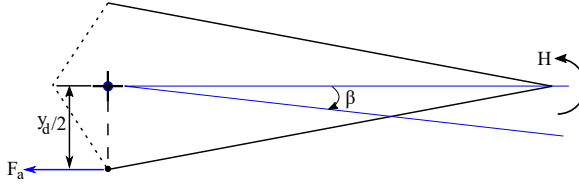


Figure 5.17: Hinge moment depiction on flap.

where C_l is represented as [14]:

$$C_l = C_{l\alpha} \left(\theta_0 + \frac{\Delta\alpha_0}{\Delta\beta} \beta - \frac{\lambda\Omega R_{tip}}{\Omega r} \right) \quad (5.11)$$

Considering the non-dimensional flap chord $Z = c_f/c$, the two terms $\frac{dC_h}{dC_l}$ and $\frac{dC_h}{d\beta}$ in Eq. 5.10 are given as follows [15]:

$$\frac{dC_h}{dC_l} = -0.01018 - 0.5494Z + 1.028Z^2 - 0.9934Z^3 + 0.277Z^4 \quad (5.12)$$

$$\frac{dC_h}{d\beta} = -0.8469 + 0.9833Z - 0.07663Z^2 + 0.2567Z^3 - 0.3205Z^4 \quad (5.13)$$

The flap hinge moment coefficient is given by [12]:

$$C_h = \frac{h}{\frac{1}{2}\rho V^2 c_f^2} \quad (5.14)$$

Using Eq. 5.10 and Eq. 5.12, the hinge moment per unit span is given by:

$$h = \frac{1}{2}\rho(\omega r)^2 c_f^2 \left[C_{l\alpha} \left(\theta_0 - \frac{\lambda R_{tip}}{r} \right) \frac{dC_h}{dC_l} Z + \frac{dC_h}{d\beta} Z \beta \right] \quad (5.15)$$

where θ_0 is the collective rotor blade pitch angle, ρ is the air density, $C_{l\alpha}$ is the lift curve slope of the rotor blade's airfoil and λ is the rotor inflow ratio. The total hinge moment can be obtained by integrating the expression in Eq. 5.15 along the flap span and is given in Eq. 5.16 [12] (assuming all the other quantities are constant along the span). Using Eq. 5.16 and Eq. 5.11 the hinge moment on the flap is calculated, which is then converted to the force by dividing with the moment arm as shown in Fig. 5.17.

$$H = \frac{1}{2} \rho \Omega^2 c_f^2 \left[\left(\frac{R_2^3}{3} - \frac{R_1^3}{3} \right) \left(C_{l\alpha} \theta_0 \frac{dC_h}{dC_l} Z + \frac{dC_h}{d\beta} Z \beta \right) - C_{l\alpha} \lambda R_{tip} \left(\frac{R_2^2}{2} - \frac{R_1^2}{2} \right) \frac{dC_h}{dC_l} Z \right] \quad (5.16)$$

5.3.4. ESTIMATION OF GEOMETRIC PARAMETERS

The third important parameter to estimate is the chordwise stroke x_t necessary to achieve the desired deflection angle β . This stroke length is associated with the flap geometry and the tip deflection of the flap. To establish this relationship, deflections are obtained in FEA for different aspect ratios defined in Eq. 5.9. Figure 5.18 shows the trailing edge tip deflection plotted against the aspect ratios for x_t values of 1 mm, 3 mm and 5 mm.

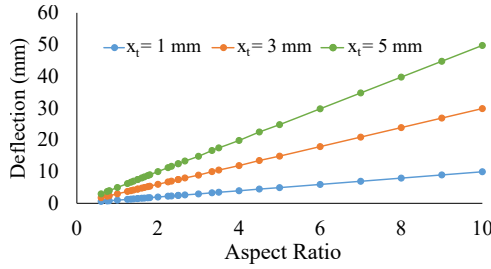


Figure 5.18: Relation of deflection and aspect ratio.

Based on the results in Fig. 5.18 and assuming that the location of constraint on the top skin and the point of actuation on the bottom skin is vertically in-line, the expression in Eq. 5.17 is obtained. Once x_t is known, the corresponding movement of the spring or the spanwise shaft x_s is determined using Eq. 5.18.

$$x_t = \frac{\beta}{\mathcal{R}} \quad (5.17)$$

$$x_s = \frac{x_t}{\tan \varphi} \quad (5.18)$$

where, φ is the angle of the inclined surface of the spanwise shaft 2 in Fig. 5.3.

5.3.5. FORCE EQUILIBRIUM

In order to solve the overall design problem, the equilibrium of forces is established on the spanwise shaft (2) in Fig. 5.3. The effect of the frictional force is included in the formulation. Figure 5.19 shows the free-body diagram (FBD) for the case when the flap tends to rotate upwards due to the outward movement of the spanwise shaft. Resolving the forces shown in Fig. 5.19, the following expressions are obtained:

$$F_s + F_{fk1} + F_{fr} \cos \varphi + F_r = F_n \sin \varphi + F_c \quad (5.19)$$

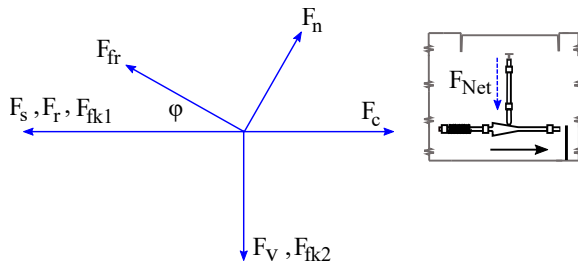


Figure 5.19: Equilibrium of forces when the flap tends to deflect upwards.

$$F_n \cos \varphi + F_{fr} \sin \varphi = F_v + F_{fk2} \tag{5.20}$$

where φ is the angle created by the tapered portion of the spanwise shaft, F_s is the spring force given by $(K_s x_s + pL)$, F_{Net} is the net force accounting for the aerodynamic force and the elastic force of the flap, F_n is the normal force due to component of F_{Net} , F_r is the reaction force developed by the mechanical endstop due to the applied aerodynamic load, F_v is the vertical force of constraint that compensates all vertical components of the forces acting on the inclined plane, F_{fk1} and F_{fk2} are the friction forces due to the kinetic friction caused by the spanwise shaft and chordwise shaft supports respectively, and F_{fr} is the friction force due to the rolling contact at the inclined surface. These frictional forces can be determined by an appropriate selection of the coefficient of friction. It must be noted that the friction force due to the weight of the shaft is considered negligible and not included in the formulation.

As noticed, the outward movement of the spanwise shaft results in the extension of the spring and upward movement of the flap. Similarly, contraction of the spring deflects the flap downwards. Figure 5.20 shows the free-body diagram when the flap tends to deflect downwards due to the inward movement of the spanwise shaft. Resolving the forces shown in Fig. 5.20, the following expression in Eq. 5.21 and Eq. 5.22 are obtained.

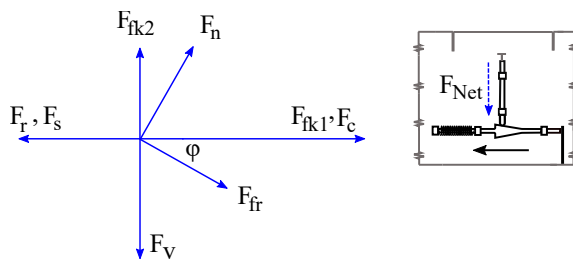


Figure 5.20: Equilibrium of forces when the flap tends to deflect downwards

$$F_s + F_r = F_c + F_n \sin \varphi + F_{fk1} + F_{fr} \cos \varphi \tag{5.21}$$

$$F_n \cos \varphi + F_{fk2} \sin \varphi = F_v + F_{fr} \sin \varphi \quad (5.22)$$

Equations 5.19 and Eq. 5.21 indicate the complication in the centrifugal-force-based actuation with the morphing flap. From the equations, it can be seen that the force required by the spring to deflect the flap downwards during the so-called unloading cycle is not equal to the force required to deflect the flap upwards in the so-called *loading cycle* on the ground. This behaviour is mainly due to the fact that the baseline position in the loading cycle is achieved on the ground, with negligible influence of the aerodynamic loads. However, during the unloading cycle, the spring has to account for the aerodynamic loading due to flap deflection and rotor blade pitch angle.

Another important factor to consider in the system is the effect of friction force with the morphing flap. The magnitude of the elastic force produced by the flap varies, depending on its deflection angle β . Consequently, the friction force at the interface of the spanwise shaft and the chordwise shaft also changes. To demonstrate this behaviour of the friction caused by the morphing flap, a bench test is performed where a pulley system is used to apply the force at the free end of the spanwise shaft, and the extension in the spring is noted as shown Fig. 5.21. More details of the setup and instrumentation to record the extension are discussed in Chap. 6.

5

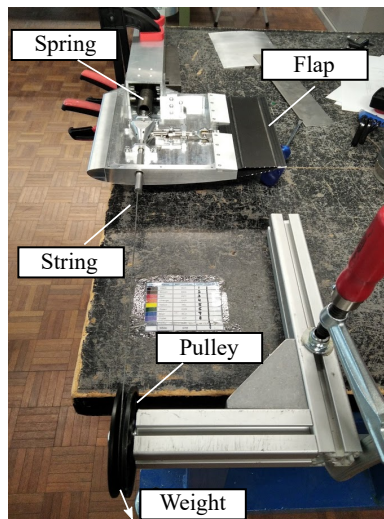


Figure 5.21: Flap at baseline position when weights are applied.

In Fig. 5.22, the result of the bench test is presented where the spring extension is shown for the two cases. In the first case, the flap is removed from the system, and weights are loaded in small steps to record the spring extension. During the *unloading cycle*, the weights are removed, and the corresponding movement of the spring is recorded. In the second case, the same experiment is performed with the flap attached to the chordwise shaft. Initially, the flap is set at a deflected position and held by the spring's preload. Subsequently, the weights are loaded till the baseline position is achieved, as

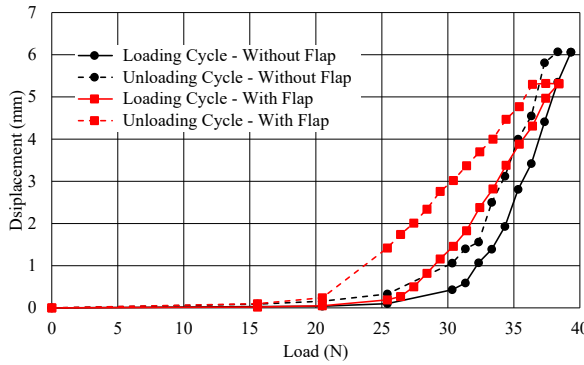


Figure 5.22: Effect of friction during loading and unloading cycle.

shown in Fig. 5.21. During the unloading cycle, the flap is brought back by removing the weights in small steps. It can be seen in Fig. 5.22 that the slopes of the loading and unloading curves are approximately similar when the flap is not attached. However, when the flap is engaged, the slope of the loading curve is more than the unloading curve. The difference in the slopes indicates that the system has to account for varying forces of kinetic friction during the *unloading cycle* and the *loading cycle*. In addition, it can also be observed that the elastic force of the flap reduces the spring preload as the deflection starts at an earlier value compared to the case when the flap is not engaged.

PROBLEM SETUP

Using Eq. 5.19 - 5.22 presented in Sec. 5.3.5, an iterative procedure is proposed to determine the spring constant and the preload required to keep the flap deflected at a certain position. When the helicopter is on the ground, the preload in the spring must keep the flap deflected till the rotor speed exceeds 90% RPM. During this phase, a component of F_n acts in the direction of the total applied force on the spring. This component corresponds to the magnitude of F_e as the aerodynamic forces on the flap are negligible at this stage. In this case, the preload is given by:

$$pL = F_{c(90\%)} + F_{n1} \sin \varphi \quad (5.23)$$

where F_{n1} is the normal force corresponding to the maximum value of F_e . When the rotor speed exceeds 90% RPM and reaches 100% RPM, the apparent centrifugal force increases, and the spring extends, resulting in the movement of the spanwise shaft and causing the flap to deflect upwards. In this case, the resulting equilibrium equation is given as follows:

$$(K_s x_s)_{100\%} = F_{c(100\%)} + F_{n(min)} \sin \varphi - F_{fk1} - F_{fr} \cos \varphi - pL \quad (5.24)$$

where $F_{n(min)}$ is the minimum value of normal force. When the helicopter starts hovering, the rotor blade's collective pitch is at a specified angle resulting in a hinge moment on the flap. The equilibrium of forces is represented by the following equation in this case:

$$(K_s x_s)_{100\%} + F_r = F_{c(100\%)} + F_{n2} \sin \varphi - F_{fk1} - F_{fr} \cos \varphi - pL \quad (5.25)$$

where F_{n2} is the normal force corresponding to the aerodynamic force at the required rotor blade pitch angle. During the hover phase, when the operational need to deform the flap arises, the rotor RPM is reduced. In this situation, the spring responds to the reduction in the centrifugal force. This case is given by Eq. 5.26 as follows:

$$(K_s x_s)_{90\%} + F_r = F_{c(90\%)} + F_{n(max)} \sin \varphi + F_{fk1} + F_{fr} \cos \varphi - pL \quad (5.26)$$

The effective spring force $[K_s x_s]_{ef}$ required to deform the flap to the required angle β can be obtained by using Eq. 5.25 and Eq. 5.26 resulting in the expression shown in Eq. 5.27 and Eq. 5.28. In this way, the spring stiffness K_s is obtained as shown in Eq. 5.29. If the desired spring stiffness is now used in Eq. 5.24, the resulting displacement of the spanwise shaft, shown in Eq. 5.30, turns out to be higher than the required value of x_s corresponding to the deflection β . This means that for the desired tip deflection during the unloading cycle, the initial deflection of the flap should be kept higher than the required flap deflection β . In other words, the initial position of the flap needs to be at a higher deflected position than what is required when the RPM is reduced to 90%. This approach does not change the overall functionality of the system since the initial flap deflection is only present on the ground when the rotor is spinning up.

$$[K_s x_s]_{ef} = (K_s x_s)_{100\%} - (K_s x_s)_{90\%} \quad (5.27)$$

$$[K_s x_s]_{ef} = F_{c(100\%)} - F_{c(90\%)} + F_{n(min)} \sin \varphi - F_{n(max)} \sin \varphi \quad (5.28)$$

$$K_s = \frac{[K_s x_s]_{ef}}{x_s} \quad (5.29)$$

$$x_{s(max)} = \frac{F_{c(100\%)} + F_{n(min)} \sin \varphi - F_{fk1} - F_{fr} \cos \varphi - pL}{K_s} \quad (5.30)$$

where $x_{s(max)}$ is the maximum value of the spring extension which results in the maximum chordwise movement $x_{t(max)}$ and the maximum flap deflection angle $\beta_{(max)}$.

From Eq. 5.23, it is clear that for a full-scale passive system, the preload mainly depends on the apparent centrifugal force at 90% RPM. Therefore, in Eq. 5.24, pL is considered to be equal to the centrifugal force at 90% RPM. Once $x_{s(max)}$ is determined, the value of preload can be estimated more accurately. The spring stiffness and the preload obtained using the aforementioned approach can now be related to the off-the-shelf extension spring data or discussed with a spring manufacturer for customization. In case of unavailability of the spring, the process is repeated by changing the mass of the spanwise shaft or adjusting the angle φ . The iterative process is shown in Fig. 5.23.

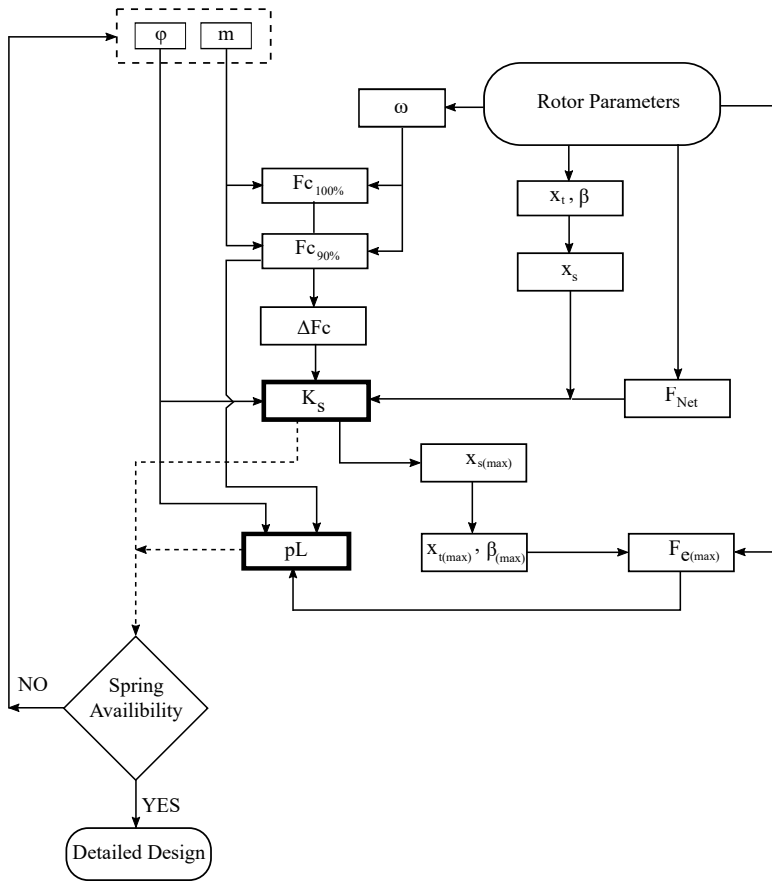


Figure 5.23: Proposed iterative process to obtain preload and stiffness of the spring.

5.4. WORKING PRINCIPLE OF PASSIVE CONCEPT

Based on the discussion in the preceding sections, the working principle of the passive concept is summarized and shown in Fig. 5.24. The trailing edge flap is initially adjusted and set at a deflected position C, higher than what is desired at 90% RPM. Once the rotor starts rotating, the flap stays at the deflected position due to the preload. As the rotor RPM increases, the corresponding centrifugal force also increases and crosses the value corresponding to the spring preload causing the flap to deflect to its baseline position A. At this stage, the rotorcraft can perform its normal operation. Once the operational requirements of the flap deflection arise, the RPM is reduced, resulting in the flap deflecting downwards. The desired deflection position B is achieved once the RPM is reduced to 90%. After the operational requirement is fulfilled, the RPM increases again, bringing the flap to its baseline position. The deflection of the extension spring corresponding to the working principle is depicted in Fig. 5.25. The spring is fully extended at the baseline position and is kept undeflected on the ground when the flap is deflected at its extreme

position.

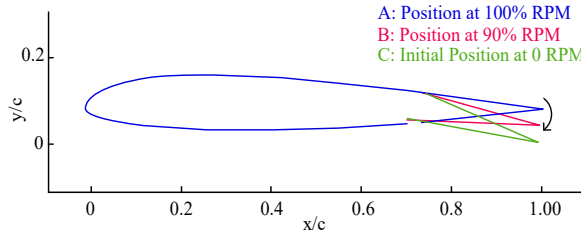


Figure 5.24: Working principle of passive concept.

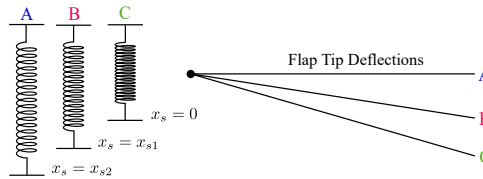


Figure 5.25: Spring deflections in the passive concept.

CASE STUDY

A short case study is presented in this section to evaluate the outcome of the formulation presented in Sec. 5.3.5 for a typical helicopter. In the present case, requirements are generated pertaining to the Bo105 helicopter as mentioned in Sec. 5.1 and also discussed by Vidyarthi et al. [3]. For the sake of simplicity, the passive system is considered frictionless in the case study. The CG of the spanwise shaft and spring is assumed to be at the centre of the flap. Table 5.1 presents the summary of the requirements.

Table 5.1: Summary of requirements related to Bo105[3]

Parameter	Value	Unit
R_{tip}	4.9	m
R_{root}	0.875	m
R_1	3.43	m
R_2	4.41	m
$\omega_{100\%}$	424	RPM
β	6	degree
θ_0	10	degree
c	270	mm

Table 5.2 shows the results of the four iterations carried out with a different mass of the shaft and spring and the angle φ . It can be seen that the variation in mass has a significant effect on both the spring and the stiffness of the extension spring. The maximum

flap angle β is also an important outcome as it indicates the amount of bottom surface that has to be accommodated inside the mechanism at the start. Since this portion needs to be straight for translation, it can impose a constraint of maximum allowable β and has to be considered during the detailed design phase.

Table 5.2: Summary of results [3]

Iteration	Value	Unit
1	$m = 0.2 \text{ kg}$	$K_s = 18 \text{ N/mm}$
	$\varphi = 20^\circ$	$pL = 1275 \text{ N}$
		$\beta_{(max)} = 18^\circ$
2	$m = 0.2 \text{ kg}$	$K_s = 17 \text{ N/mm}$
	$\varphi = 10^\circ$	$pL = 1275 \text{ N}$
		$\beta_{(max)} = 9^\circ$
3	$m = 0.3 \text{ kg}$	$K_s = 46.5 \text{ N/mm}$
	$\varphi = 20^\circ$	$pL = 1895 \text{ N}$
		$\beta_{(max)} = 10.5^\circ$
4	$m = 0.3 \text{ kg}$	$K_s = 32.5 \text{ N/mm}$
	$\varphi = 10^\circ$	$pL = 1882 \text{ N}$
		$\beta_{(max)} = 7.5^\circ$

It can be observed from the case study that an estimation of the required spring parameters is possible with the analytical formulation. As a quick check, the spring stiffness and preload are searched in the online catalogues of few spring manufacturers ^{1,2,3,4}. The outcome of this search reveals that both the spring stiffness and the preload values can be found independently for off-the-shelf springs. The author believes that the combinations of the spring stiffness and preload given in Tab. 5.2 calls for customized manufacturing of springs. In addition, a customized option shall also help in understanding the possibilities and limitations of the passive system for large-scale applications.

5.5. SUMMARY

In this chapter, details of the passive camber morphing system were presented. The importance of the passive morphing in relation to the variable rotorcraft was briefly explained, which resulted in the requirement of flap deflection and RPM range for which the flap deflection is desired. A novel concept was introduced, which showed the potential of achieving the desired goal of flap morphing by using centrifugal forces. It was shown that the extension spring is the key component in the system whose stiffness and preload have to be calculated based on the rotorcraft requirement of flap size and deflection angle. A complete analytical scheme was presented, which was able to predict the desired spring parameters quickly and with reasonable accuracy using well-established

¹<https://www.tevema.com/>

²<https://www.acxesspring.com/>

³<https://www.leespring.com/>

⁴<https://www.amatec.nl/en/>

theories. The details of the demonstrator built as a proof of concept for the passive system are included in Chap. 6, and the results of the testing are described in Chap. 7.

BIBLIOGRAPHY

- [1] K. Vidyarthi, M. Beuker, F. Yin, M. Voskuijl, and M. Pavel, "Hoplite - a conceptual design environment for helicopters incorporating morphing rotor technology," English, in *Proceedings of the 44th European Rotorcraft Forum*, C. Hermans, Ed., 44th European Rotorcraft Forum, ERF 2018 ; Conference date: 18-09-2018 Through 21-09-2018, 2018.
- [2] T. van Holten and J. A. Melkert, "Helicopter Performance, Stability and Control," Tech. Rep. November, 2002, p. 746.
- [3] K. Vidyarthi, Y. Zahoor, M. D. Pavel, M. Voskuijl, and R. de Breuker, "Active and passive camber morphing for helicopter rotors towards performance improvements in hover and vertical flight," *Vertical Flight Society's 76th Annual Forum and Technology Display*, 2020.
- [4] J. Rauleder, B. G. Van Der Wall, A. Abdelmoula, D. Komp, S. Kumar, V. Ondra, B. Titurus, and B. K. Woods, "Aerodynamic performance of morphing blades and rotor systems," *Annual Forum Proceedings - AHS International*, vol. 2018-May, 2018, ISSN: 15522938.
- [5] F. Gandhi, C. Duling, and F. Straub, "On power and actuation requirement in swashplateless primary control of helicopters using trailing-edge flaps," *The Aeronautical Journal (1968)*, vol. 118, no. 1203, pp. 503–521, 2014.
- [6] D. Han, V. Pstrikakis, and G. N. Barakos, "Helicopter performance improvement by variable rotor speed and variable blade twist," *Aerospace Science and Technology*, vol. 54, pp. 164–173, 2016, ISSN: 1270-9638.
- [7] M. Khoshlahjeh, E. S. Baet, F. Gandhi, and S. Webster, "Helicopter performance improvement with variable chord morphing rotors," *36th European Rotorcraft Forum, ERF 2010*, vol. 2, pp. 919–930, 2010.
- [8] Y. Zahoor, R. De Breuker, M. Voskuijl, and J. Sodja, *Actuation device for actuating a high-lift device of a rotor blade*, TU Delft Patent N2029203, Sep.2021.
- [9] S. Timoshenko and S. W. Krieger, *Theory of Plates and Shells*. McGraw Hill Book Company, 1989.
- [10] L. P. Kollár and G. S. Springer, *Mechanics of Composite Structures*. Cambridge University Press, 2003.
- [11] "Aeroelastic response of composite helicopter rotor with random material properties," *Journal of Aircraft*, vol. 45, no. 1, pp. 306–322, 2008, ISSN: 15333868.
- [12] C. Walz and I. Chopra, "Design and testing of a helicopter rotor model with smart trailing edge flaps," 1994.

- [13] C. Kassapoglou, *Design and Analysis of Composite Structures: With Applications to Aerospace Structures, 2nd Edition*. Wiley, 2013, ISBN: 9781118536940.
- [14] J. H. Lee, B. Natarajan, W. J. Eun, S. R. Viswamurthy, J. S. Park, T. Kim, and S. J. Shin, "Structural and mechanism design of an active trailing-edge flap blade," *Journal of Mechanical Science and Technology*, vol. 27, pp. 2605–2617, 2013, ISSN: 1738494X.
- [15] S. M. Berkowitz, "Theory of wing sections," *Journal of the Franklin Institute*, vol. 249, p. 254, 1950, ISSN: 00160032.

6

EXPERIMENTAL SETUP

To understand how something works, figure out how to break it.

Nassim Nicholas Taleb

6.1. INTRODUCTION

Two morphing systems are introduced in the preceding chapters, namely the active morphing system in Chap. 4 and the passive morphing system in Chap. 5. Each of these systems needs to have a proof-of-concept model or demonstrator to show that the design studies can be transformed towards the realization of each concept. For this reason, appropriate demonstrators are designed, fabricated, integrated, and instrumented to perform the required tests. These tests are characterized as the wind tunnel test for the active system, whirl tower test for the active system, and whirl tower test for the passive system. This chapter provides a detailed account of the processes involved in developing, manufacturing, and integrating these demonstrators.

Section 6.2 explains the development and manufacturing process related to morphing skin, active demonstrator, and passive demonstrator. Section 6.3 discusses the test setups and objectives for each test campaign.

6.2. DESIGN AND MANUFACTURING OF THE DEMONSTRATORS

For each of the systems mentioned above, the design and manufacturing of the demonstrators include the mechanical system housed inside an aluminium structure and a morphing flap made out of composite prepreg material as discussed in Chap. 3. The next section is dedicated to discuss the manufacturing of the morphing flap.

6

6.2.1. DESIGN AND MANUFACTURING OF MORPHING FLAP

The schematic showing the details of the flap manufactured for the TRIC concept is shown in Fig. 6.1.

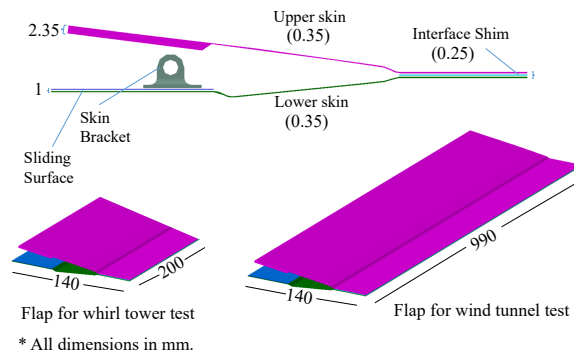


Figure 6.1: TRIC flap manufacturing layout.

The flap consists of the top and bottom skins made out of Thinpreg NTPT 135 (NTPT-HTS(12K)-5-35%), which is a carbon fibre prepreg material with plies having a thickness of 0.05 mm. As mentioned in Chap. 3, the boundary conditions for the TRIC require the upper skin to be fully clamped while allowing the bottom skin to translate. As the required skin thickness for the demonstrators was 0.35 mm (7 layers), it was not sufficient to mechanically fasten the top skin with the help of countersunk screws. This was because sufficient thickness was required for the countersunk screws to be fully flushed

with the skin. Furthermore, the bottom skin also needed to be thicker than 0.35 mm due to two reasons. Firstly, the bottom skin required a smooth sliding surface giving rise to the need for both surfaces of the bottom skin to be of mould quality. Secondly, a bracket required to connect the skin to the actuators had to be bonded to the bottom skin. Due to these reasons, two additional laminates were produced with the following considerations to act as stiffeners.

1. One laminate was produced having a width of approximately 30 mm corresponding to the interface on the blade structure. The thickness of this laminate was kept at 2.35 mm required to flush M3 countersunk screws completely. This stiffener was attached to the top skin before its curing. This laminate required 40 plies to achieve the desired thickness of 2.3 mm and was produced following the guidelines [1] for ply drop-off to avoid stress concentrations.
2. Keeping in view the available design space and size of the flap, the overall skin thickness was set at 1 mm. Therefore, the second laminate with the required width was produced with 0.65 mm thickness and attached to the bottom skin before its curing. An aluminium sheet was placed on top of it to ensure that both surfaces were smooth after curing.

At the top and bottom skin interface, additional layers were used to achieve the required thickness of the trailing edge tab.

Aluminium moulds were designed and manufactured to produce the laminates required for the test campaigns. The flap span for the wind tunnel testing was required to be 990 mm, while the span of the flap for the active and passive system tested in the whirl tower test was set at 200 mm. A fixture with locating pins was devised to join the metal bracket with the bottom skin (after curing) at the required location. In addition, the size of the skins in the chordwise direction (both sides) was kept 15 mm to 25 mm larger than required to allow trimming to the exact size later. The mould, skin, and fixture arrangement for the bottom skin is shown in the Computer-Aided Design (CAD) model in Fig. 6.2.

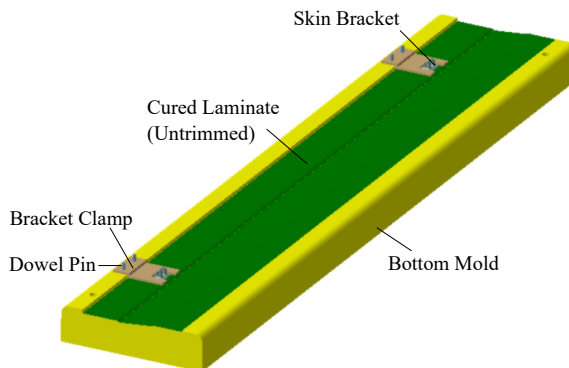


Figure 6.2: Bottom mould showing bracket and fixture on skin.

The curing of laminates took place in the autoclave at the recommended temperature and pressure cycle ¹. After the curing cycle of the longer flap (990 mm), some warping in both upper and bottom skin was observed due to residual stresses in the skin, as shown in Fig. 6.3.



Figure 6.3: Wind tunnel demonstrator skin.

To eliminate this warping, the extra material for trimming was removed, and the skins were heated for stress relieving at 60° Celsius for 30 minutes. This process significantly reduced the warping after which the skins were put in the mould for joining the two halves using the structural adhesive EC 9323, which is a structural epoxy adhesive from 3M ². It was used with glass beads to maintain a uniform thickness throughout the length of the flap. After allowing sufficient time to settle at room temperature, the joint was cured further at elevated temperature to increase its strength. The final form of the two flaps produced in this way is shown in Fig. 6.4 and Fig. 6.5. It has to be mentioned that the presence of warping and joining the upper and bottom skin without proper jigs and fixtures contributed to a non-uniform bending stiffness of the longer flap. The details and consequences of this behaviour are discussed in Chap. 7.

6



Figure 6.4: Wind tunnel demonstrator flap.



Figure 6.5: Whirl tower demonstrator flap.

¹<https://www.thinplytechnology.com/datasheets>

²https://www.3mnederland.nl/3M/nl_NL/p/d/v000118253/

6.2.2. WIND TUNNEL TEST DEMONSTRATOR

The wind tunnel test demonstrator was designed as an aluminium structure with a length of 990 mm and having a cross-section corresponding to NACA 23012 airfoil with a chord length equal to 270 mm. The actuation system was housed in the pockets created in the solid aluminium structure. The overall mechanics of the actuation system in the area corresponding to the Bo105 blade cross-section is shown in Fig. 6.6. It consists of actuators in series connected via metallic link rods to the morphing flap. Based on the force required for actuation determined in Chap. 4, two sets of actuators are used and placed farthest apart to actuate the flap. Steel bush is used in the connection holes of these link rods to provide smooth contact with minimum play. The actuators were mechanically secured to the wingbox. The flap was mounted with the countersunk screws at the top, and a metal bracket was attached at the bottom skin. The bottom skin slides in the guides when pulled by the actuators connected with the bracket. A displacement transducer (SoftPot from spectrasymbol³) is mounted underneath the link rods, which provides the actuator displacement when a plunger moves over it. This plunger is a spring-loaded soft plunger from MISUMI⁴ which is screwed in the link rod and presses gently against the displacement transducer.

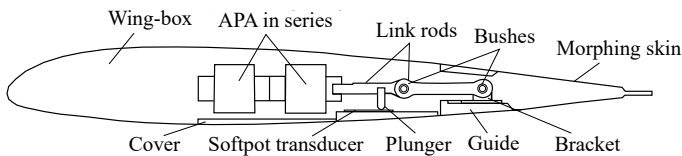


Figure 6.6: Cross-sectional view of the actuators, mechanics and skin.

The final integration of the demonstrator for the wind tunnel testing with critical components can be observed in Fig. 6.7 where a CAD model is shown along with the manufactured demonstrator.

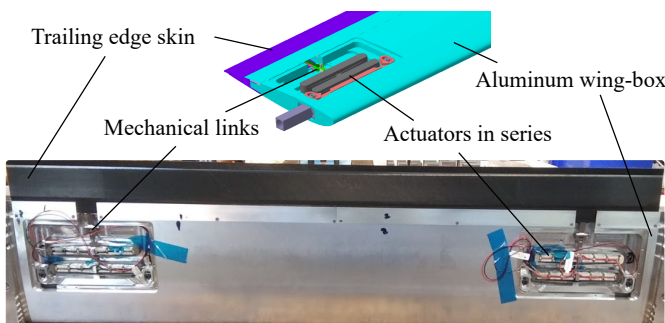


Figure 6.7: Integration of demonstrator.

³<https://www.spectrasymbol.com/>

⁴<https://uk.misumi-ec.com/vona2/detail/110300143710/>

6.2.3. WHIRL TOWER TEST DEMONSTRATORS

In this section, the design and development of the active and passive system demonstrators for the whirl tower test are presented. Some key design aspects are also discussed in relation to both the active and passive system demonstrators to help understand the correlation presented later with the experimental results.

ACTIVE SYSTEM DEMONSTRATOR

The main purpose of the whirl tower test demonstrator for the active system is to capture the response of the skin and actuators under centrifugal loads. A cross-sectional view of the demonstrator is shown in Fig. 6.8 with the main components similar to those mentioned in Sec. 6.2.2. Since the aerodynamic forces on the flap are not considered for this elementary model, the wingbox section is not made in a typical airfoil shape. Consequently, the aluminium housing for the actuation system is simplified for manufacturing.

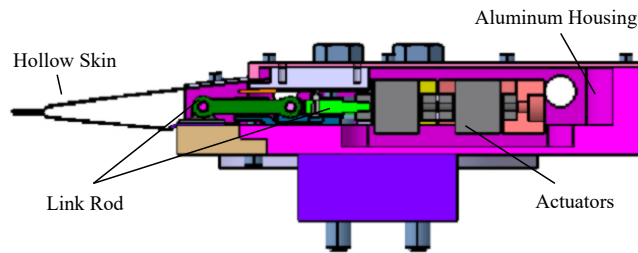


Figure 6.8: Cross-section of the actuation system.

The CG of the actuation system is adjusted with respect to the COR in such a way that the chordwise component of the centrifugal force becomes small and negligible for both the actuators and flap. As mentioned in Chap. 4, the effect of the spanwise component of the centrifugal force on the actuator and the associated mechanics can be minimized by having additional supports in the form of thin steel blades and Teflon pads as shown in Fig. 6.9

The complete CAD model of the demonstrator is shown in Fig. 6.10. The actuation system is attached to the aluminium housing using an aluminium base plate. This plate is then inserted and bolted inside the hollow aluminium beam having a cross-section of $4\text{mm} \times 4\text{mm}$. At the other end, a counterweight is fixed to balance the demonstrator about its centre of rotation. The central interface part, made of aluminium, is also secured inside the hollow aluminium beam on both sides.

PASSIVE SYSTEM DEMONSTRATOR

For the proof of concept of the passive camber morphing system presented in Chap. 5, a demonstrator is designed, which is presented in the form of a CAD model in Fig. 6.11.

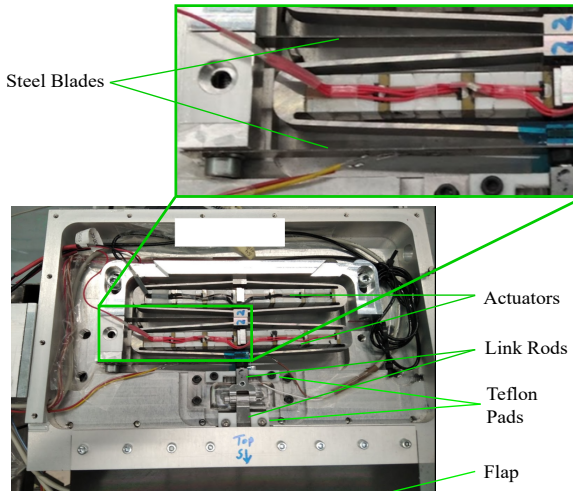


Figure 6.9: Components of the actuation system.

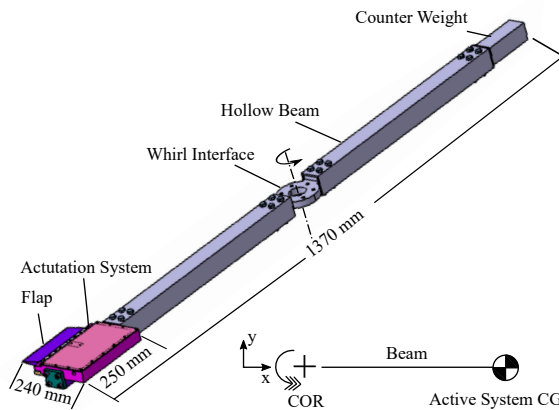


Figure 6.10: CAD model of the active system demonstrator for whirl tower test.

The spanwise shaft is supported by two flanges at each end having steel bushes. One end of the extension spring is connected to the spanwise shaft while the other end is fixed to the beam. The centre portion of the spanwise shaft is tapered, providing an inclined surface for the rollers. These rollers, which are attached to the chordwise shaft, are secured inside the groove provided by the spanwise shaft. The other end of the chordwise shaft is connected to a male rod end which is attached to the metal bracket bonded to the flap. This shaft is also supported by bearing support and pin support, as shown in Fig. 6.11.

The manufactured model with the two main shafts is shown in Fig. 6.12. In this figure, the groove and path for roller bearings can be seen. It is also worth mentioning here

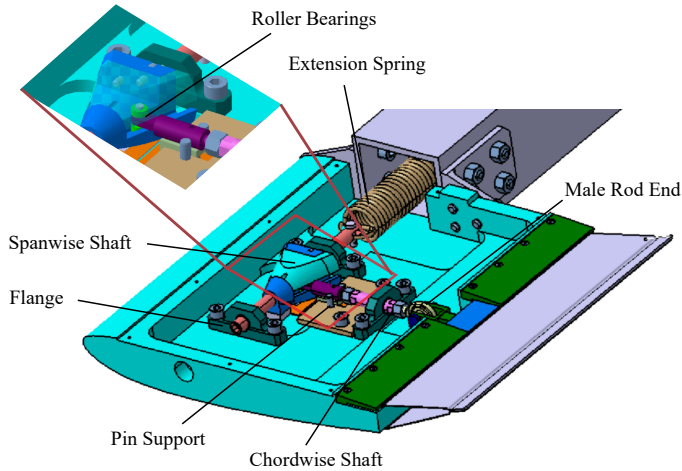


Figure 6.11: CAD model showing detail of passive system.

that the initial position of the flap is achieved by adjusting the length of the chordwise shaft appropriately. This is achieved by providing a left-hand and a right-hand threaded interface at both sides of the shaft.

6

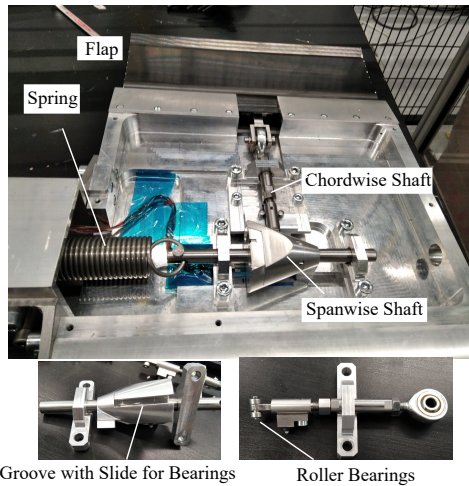


Figure 6.12: Physical model of passive system.

Before taking the passive system to the whirl tower test, some bench testing was performed to ascertain the working of the system. This was done with a pulley and string arrangement as shown in Fig. 6.13. This setup was used to estimate the initial tension in spring and the force required to deflect the flap, as shown in Fig. 6.13 (a). In addition, the same setup is utilized to estimate the force required by a spring to hold the flap at its deflected initial position. This is accomplished by removing the spring from the assembly

and attaching a string with suitable weights hanging from a pulley, as shown in Fig. 6.13 (b).

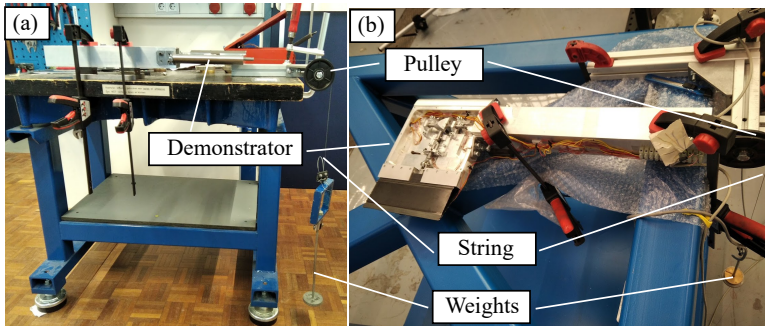


Figure 6.13: Bench test setup: Functional test (a), Flap elastic force (b).

As in the case of the active system, a detailed CAD model of the complete demonstrator for the passive morphing system is developed with the consideration that it is balanced properly on the whirl tower test setup and that the CG of the spanwise Shaft and spring assembly lies on the x-axis (spanwise direction) without any chordwise offset as shown in Fig. 6.14.

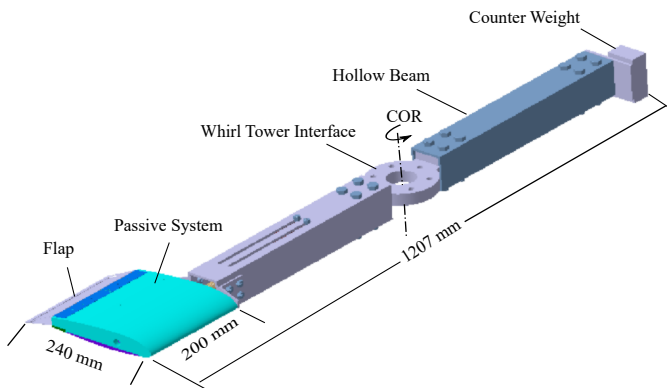


Figure 6.14: Passive demonstrator for whirl tower test.

It is also pertinent to mention that the springs for the passive demonstrator are procured from Tevema⁵ by considering the size, spring constant, and initial tension of the springs. In total, five springs were purchased for the test campaign, with some differences in the overall specifications. Since initial tension and the spring constant are the two driving parameters for the selection of the spring for the passive system, both these parameters were obtained experimentally for all the springs using a tensile test machine as shown in Fig. 6.15.

⁵<https://webshop.tevema.com/gb/extension-springs>

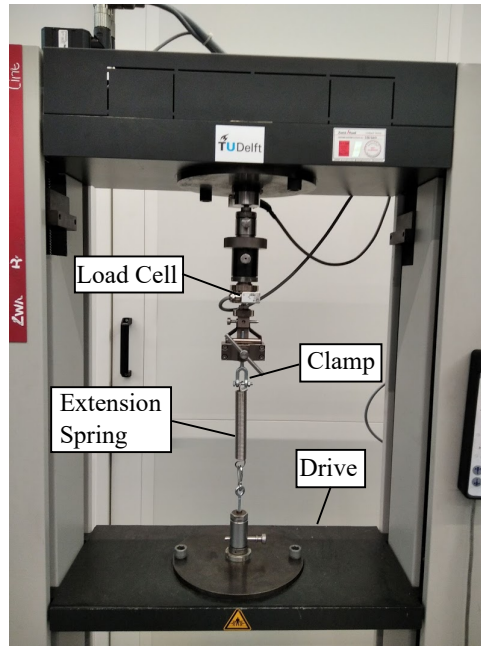


Figure 6.15: Spring test for initial tension and spring constant.

6

6.3. TEST SETUP AND OBJECTIVES

In this section, the test setup for the three test campaigns is described with the instrumentation and the test objectives.

6.3.1. WIND TUNNEL TEST

The wind tunnel experiment was performed for the active morphing system in a low-speed open jet wind tunnel with a cross-section of 60 cm × 60 cm, having a velocity of 15 m/s. The main objectives of this test campaign were to record the stroke of the actuators and the tip displacement of the flap by deforming the flap and changing the angle of attack to a maximum value of 10°. The second main objective was to measure the deformed shape of the flap under the aerodynamic loads. Although the tunnel and the setup were not ideal for recording the aerodynamic coefficients, still an effort was made to record the coefficients using a force balance.

Figure 6.16 shows the main components used during the test campaign. The demonstrator was installed in front of the exit section of the wind tunnel, and the cameras for Digital Image Correlation (DIC) were arranged to capture the 3D image of the speckle pattern painted on the trailing edge skin. The DIC system is a VIC-3D system which is a powerful solution for measuring and visualizing three-dimensional shape and displacement based on the principle of DIC. Using this method, 3D displacements and strains are available at every point on the specimen's surface ⁶. A turntable was used to change

⁶<https://www.correlatedsolutions.com/vic-3d/>

the angle of attack of the wing. Simcenter SCADAS Mobile & Recorder Data Acquisition (DAQ) system was used to measure the stroke length of the actuators from the displacement transducers. SCADAS stands for Signal Condition And Data Acquisition System ⁷. The Simcenter Testlab is a data acquisition and analysis software for noise, vibration, and durability testing ⁸ and was used to process the acquired data.

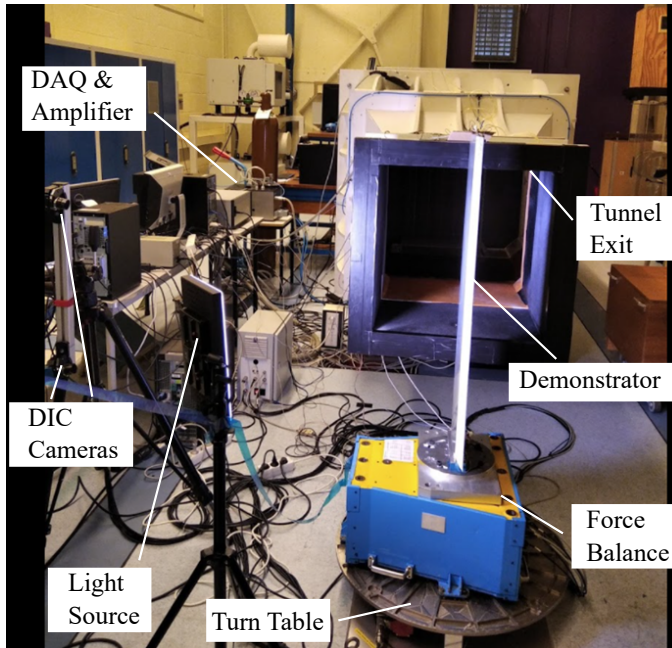


Figure 6.16: Wind tunnel test setup.

6.3.2. WHIRL TOWER TEST

The whirl tower test was performed for both the active and passive demonstrators. This was done by using a test setup meant for the vertical axis wind turbine, which was adapted in a way so that it could be used as the whirl tower test rig for both the demonstrators. The whirl tower setup shown in Fig. 6.17 was used as a test rig for the vertical axis wind turbine [2]. It consists of thrust bearings that transfer the thrust and weight of the rotor to the structural base while allowing the rotation and torque to be passed through a torque and speed sensor. The drive-line is further extended to a motor that is coupled to an appropriate gearhead to increase the torque. The full whirl tower system is clamped to a heavy steel base that is placed on the ground. Considering the limitations of the whirl tower, the maximum allowable limit of rotational speed for the test campaign was set as 240 RPM. Furthermore, the change in RPM, both increase and decrease, was also accomplished manually by inputs from the keyboard resulting in a change of 1 RPM

⁷<https://www.plm.automation.siemens.com/global/en/products/simcenter/scadas.html>

⁸<https://www.plm.automation.siemens.com/global/en/products/simcenter/testlab.html>

(maximum) to avoid damaging the torque sensors in the system. Before using the whirl tower test setup for the test campaign, necessary vibration analysis was carried out to ensure that the whirl tower testing with the demonstrators does not introduce resonant frequencies in the system.

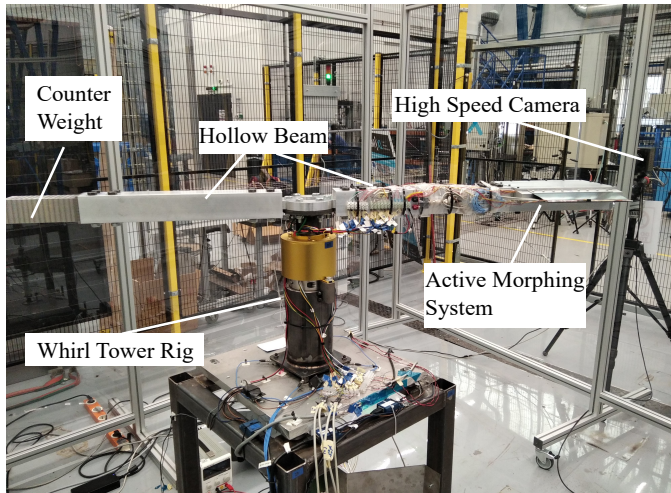


Figure 6.17: Whirl tower setup for active system.

6

ACTIVE SYSTEM TEST

The test campaign involved testing the active morphing demonstrator under centrifugal loads. One of the main objectives of the test was to record the response of the actuator under centrifugal load by recording its stroke. The second main objective was to observe the tip deflections of the flap. The measurements corresponding to these objectives were recorded in both the quasi-static and dynamic tests of the actuation system.

The test setup shown in Fig. 6.17 consists of an active morphing system demonstrator with an interface at the centre for its attachment to the whirl tower. The whirl tower system was mounted on a rigid base. A data acquisition system was used to record the actuator displacement and strain in the skin while a high-speed camera (Photron⁹ FAST-CAM Mini AX200) was positioned to capture the tip deflection of the flap. The types of sensors used in the experiments and their location are shown in Tab. 6.1. The strain gauge used on the top skin was a quarter bridge strain gauge mounted in the chordwise direction. This strain gauge was placed at the midpoint, both spanwise and chordwise, and was used to measure the strains when the skin bends or morphs as a result of the applied force. Another strain gauge was placed on the bottom skin in the spanwise direction to observe the strains that might occur as the result of centrifugal force. The third strain gauge was a full-bridge strain gauge that comes embedded on the piezoelectric actuator. A displacement transducer (SoftPot from spectrasymbol¹⁰) was used to

⁹<https://photron.com/>

¹⁰<https://www.spectrasymbol.com/>

measure the stroke of the actuation system. This transducer is in the form of a membrane over which a spring-loaded plunger moves. This plunger was screwed to the link rod, which is attached to the skin. This transducer was used to measure directly the actual displacement that was forced on the skin to complement the actuator strain gauge, which provided an indirect displacement measurement.

Table 6.1: Instrumentation overview.

Sensor	Location
Strain gauge	Top skin surface
Strain gauge	Bottom skin surface
Strain gauge	Actuator
Displacement transducer	Link rod
LEDs	1 on skin tip, 4 on aluminum housing, 1 fixed to the ground
Triaxial Accelerometer	Turbine base

In order to capture the tip displacement of the flap from the high-speed camera, a single LED is placed on the tip of the flap to indicate its deflection under different actuation amplitudes. In addition, one LED is set as a fixed point (FP) attached to the ground while four LEDs are placed on the aluminium housing to indicate any torsional deformations of the demonstrator. These four LEDs are on the same plane. This arrangement of LEDs is shown in Fig. 6.18.

To have a sufficiently darker background and to have a high frame rate, the shutter speed was adjusted to $1/600,000$ s, and the frame rate was set to 9,000 frames/s. For each test case, a high-speed video was recorded by triggering the camera at a point where the plane defined by 4 LEDs as shown in Fig. 6.18 is nearly perpendicular to the viewing axis of the camera. The trigger was generated by a photosensor present in the whirl tower and enabled the recording of the frames before and after the trigger generation. This ensured that the frame of interest was always captured and also helped to reduce the number of frames captured in each video.

The purpose of mounting a triaxial accelerometer on the base of the turbine was to take note of any adverse vibrations on the demonstrator during the whirl tower testing.

PASSIVE SYSTEM TEST

The arrangement for the passive whirl tower test is similar to the one mentioned for the active system, as shown in Fig. 6.19. The objective of the test was to show the function of the passive camber morphing under the influence of the apparent centrifugal force. In this test, the focus was to obtain the spanwise and chordwise movements of spanwise and chordwise shafts, respectively, and also the corresponding tip deflections of the flap. A displacement transducer, similar to the one used for the active test, was fixed underneath the two shafts providing the stroke measurement. For the flap tip deflection, a high-speed camera was used.

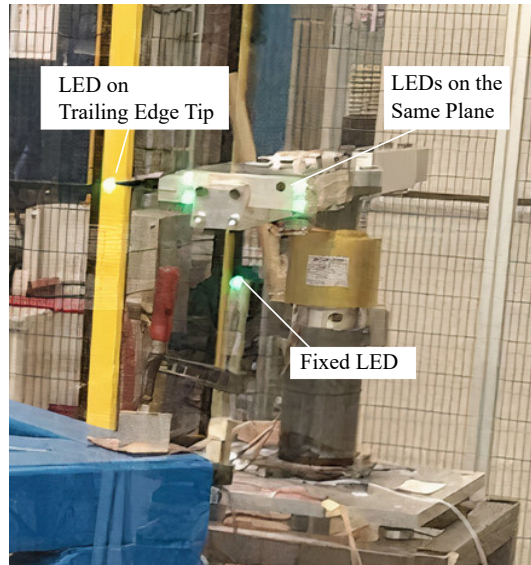


Figure 6.18: Whirl tower setup with LEDs.

6

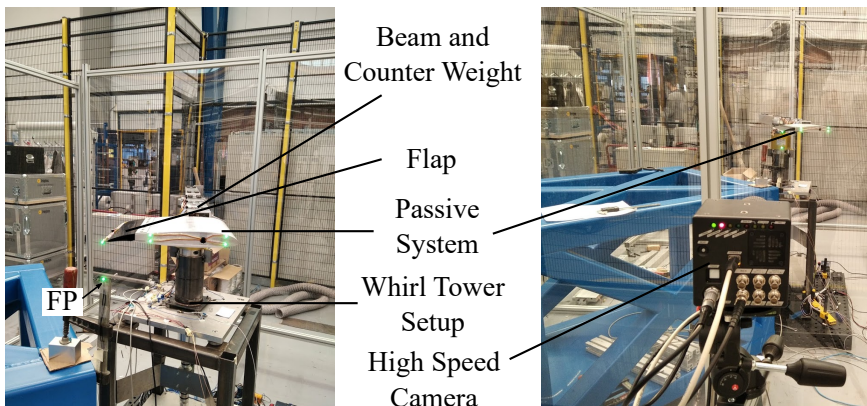


Figure 6.19: Whirl tower setup for passive system.

6.4. SUMMARY

This chapter presented a detailed account of the development and manufacturing of the three demonstrators built for the three test campaigns. This includes the wind tunnel test demonstrator and whirl tower test demonstrators for the active and passive systems. Two flaps were manufactured using prepreg carbon fibre material. The longer flap with a 990 mm span was dedicated to the wind tunnel test, while the shorter flap, having a span of 200 mm, was used to test the active system and passive system. Both the active and

passive system demonstrators were developed to ensure proper balance on the setup. This was achieved by detailed CAD modelling.

The test campaigns consisted of a wind tunnel test for the active system and a whirl tower test for both the active and passive systems. For these test campaigns, requisite instrumentation and test setup were explained. In the case of the wind tunnel test, a 60 cm × 60 cm, a low-speed tunnel was used, while for the whirl tower test, a special test setup was utilized with certain limitations. A summary of the whole test campaign is presented in Tab. 6.2 where the full-scale conditions correspond to the data obtained for Bo105 [3, 4].

Table 6.2: Overview of the scope of the test campaign.

Test Description	Demonstrator Shape	Demonstrator Size	Measured Parameters	Test Conditions	Full-scale Conditions (Bo105)
Wind tunnel test of the active morphing system in an open jet facility	Aerodynamic profile	<ul style="list-style-type: none"> Span = 990 mm Chord = 270 mm 	<ul style="list-style-type: none"> Deformed shape. Actuator stroke Flap tip deflection under aerodynamic load 	<ul style="list-style-type: none"> Velocity 15 m/s. Flap deflection angles up to 6° Dynamic actuation at 7 Hz (1/rev) 	<ul style="list-style-type: none"> Hover tip speed 196 m/s Deflection angles up to 6° Dynamic actuation at 1/rev and higher
Whirl tower test of the active morphing system	Blunt face	<ul style="list-style-type: none"> Flap Span = 200 mm Width = 270 mm Radius = 600 mm 	<ul style="list-style-type: none"> Actuator stroke Flap tip deflection 	<ul style="list-style-type: none"> 240 RPM max 40 g appx. Flap deflection angles up to 8° Dynamic actuation at 1/rev, 2/rev and 3/rev 	<ul style="list-style-type: none"> 424RPM 450 - 800 g Flap deflection angles up to 8° Dynamic actuation at 1/rev and higher
Whirl tower test of the passive morphing system	Aerodynamic profile	<ul style="list-style-type: none"> Flap span = 200 mm Chord = 270 mm Radius = 600 mm 	<ul style="list-style-type: none"> Flap tip deflection Displacement of shafts 	<ul style="list-style-type: none"> 240 RPM Deflection angles up to 4° 	<ul style="list-style-type: none"> Flap span \approx 1 m 424 RPM Radius = 4.9 m Deflection angles up to 6°

BIBLIOGRAPHY

- [1] “Good design practices and design ‘rules of thumb’,” in *Design and Analysis of Composite Structures*. John Wiley & Sons, Ltd, 2013, ch. 12, pp. 343–349.
- [2] B. Leblanc and C. Ferreira, “Experimental characterization of H-VAWT turbine for development of a digital twin,” *Journal of Physics: Conference Series*, vol. 1452, no. 1, 2020, ISSN: 17426596.
- [3] K. Vidyarthi, Y. Zahoor, M. D. Pavel, M. Voskuijl, and R. de Breuker, “Active and passive camber morphing for helicopter rotors towards performance improvements in hover and vertical flight,” *Vertical Flight Society’s 76th Annual Forum and Technology Display*, 2020.
- [4] J. Rauleder, B. G. Van Der Wall, A. Abdelmoula, D. Komp, S. Kumar, V. Ondra, B. Titurus, and B. K. Woods, “Aerodynamic performance of morphing blades and rotor systems,” *Annual Forum Proceedings - AHS International*, vol. 2018-May, 2018, ISSN: 15522938.

7

RESULTS AND VALIDATION

What is learned out of necessity is inevitably more powerful than the learning that comes easily.

Malcolm Gladwell

During the test campaigns for the active and passive concepts, a significant amount of test data is recorded. This data requires discussion in relation to the design of morphing skin and the active and passive system designs discussed in the preceding chapters. The test setup, instrumentation, and objectives with respect to each test have already been explained in Chap. 6. Therefore, Chap. 7 focuses on the results and their relation to the numerical and analytical work done during the design process.

Keeping in view the experimental campaigns of the wind tunnel test, whirl tower test for the active system and whirl tower test for the passive system, Sec. 7.1, Sec. 7.2 and Sec. 7.3 provide the results and discussion for each test campaign respectively.

7.1. WIND TUNNEL TESTING

The first experiment conducted in relation to the active morphing system is the wind tunnel test. As discussed in Chap. 6, the main objective of this test campaign is to study the response of the actuator under aerodynamic loads, to record the deformed shapes and to observe the aerodynamic effect of morphing.

7.1.1. QUASI-STATIC TESTING

During the quasi-static tests, the demonstrator is oriented at angles of attack (AoA) between 0° and 10° and a specific voltage is applied to the actuators, and the corresponding actuator stroke is measured using the displacement transducers (DT). The input signal to the actuators is provided by using Siemens Simcenter Testlab's Multi-Input Multi-Output (MIMO) Frequency Response Function (FRF) feature, which enables the possibility of generating custom output signals. Since there are two sets of actuators to morph the flap, one DT is used for each set to record the overall displacement. Figure 7.1 presents the load displacement curves at no-load corresponding to different voltages between 80 V and 140 V. In addition, the measured stroke for the top and bottom actuators is plotted without the aerodynamic load. It can be seen that the response of the two sensors is not identical, with the bottom actuators indicating more magnitude than the top side. The response to the increasing voltage is also not entirely linear. The potential reason for this nonlinearity is the non-uniform bending stiffness of the flap over the entire span resulting from the issues encountered during the manufacturing of the flap for wind tunnel testing as discussed in Chap. 6. Another potential cause of this behaviour lies in the joining of the upper and bottom skin and its integration with the actuators. The skins are manufactured separately without a proper fixture to align the tabbed portion at the tip on both halves. Due to the absence of such a fixture, the alignment is ensured visually while joining the two halves. Similarly, when integrating the flap with the actuators, the skin had to be screwed to the aluminium housing while at the same allowing its connection to the two sets of actuators. The process of integration is also carried out without jigs and fixtures that would ensure the placement of each component at its place without putting the skin under stress.

Figure 7.2 compares the stroke lengths of the two actuators with and without the maximum aerodynamic loading. It can be seen that there is a slight decrease in the stroke length of the actuators owing to the loading conditions.

The difference in the tip deflections in the two load cases presented in Fig. 7.2 can

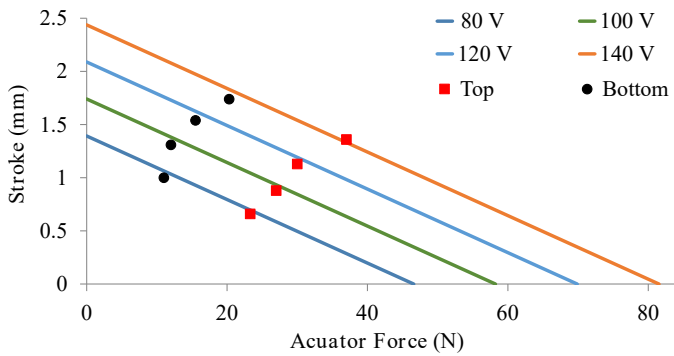


Figure 7.1: Stroke obtained from two displacement transducers without aerodynamic load.

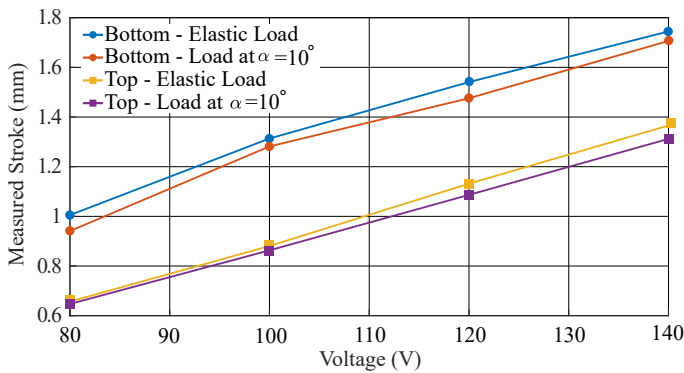
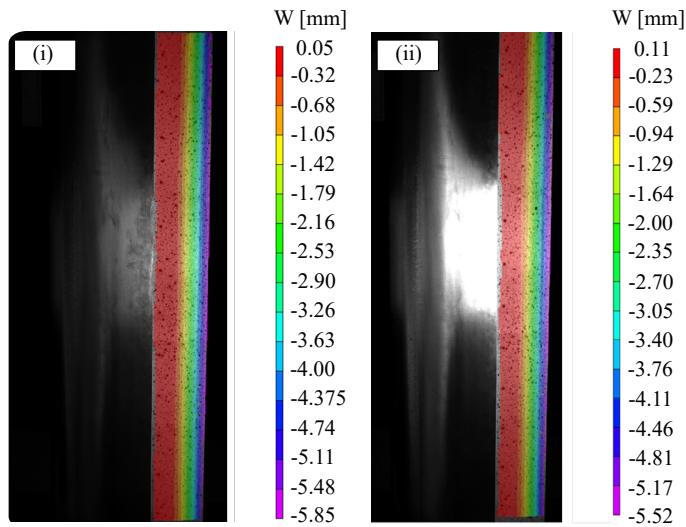


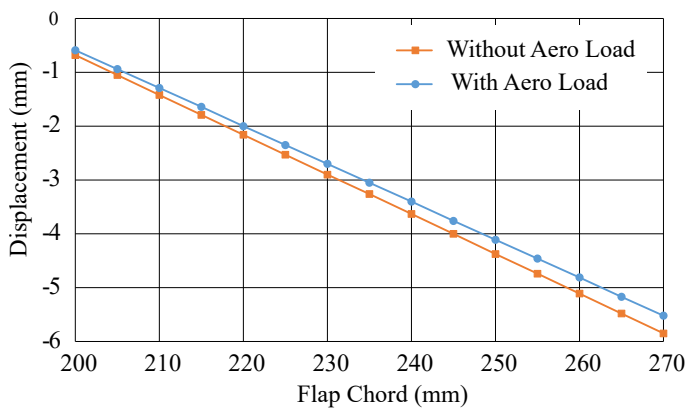
Figure 7.2: Reduction in stroke due to aerodynamic loading.

also be observed in the deformations obtained after post-processing the images recorded through the DIC technique. Figure 7.3a shows the maximum deflections recorded for the two load cases, while Fig. 7.3b highlights the difference in the two displacement fields shown in Fig. 7.3a.

To validate the FSI scheme and the aerodynamic analysis, the actuation forces are obtained corresponding to the measured stroke from each DT corresponding to the minimum load case and the maximum load case as shown in Fig. 7.2. For the experimental case, the characteristic Eq. 4.1 presented in Chap. 4 is used to obtain the forces against the applied voltage and measured stroke. For the FEA, the average of the stroke lengths measured by the two DT is used to obtain the actuation forces as discussed in Chap. 3. Table 7.1 presents the data for the top and bottom actuators corresponding to the elastic load and maximum aerodynamic load. In the last column, values obtained from the FEA are presented. The net difference obtained between the actuation forces corresponding to the two load cases is also presented in Tab. 7.1. A direct match of the actuation forces between the experimental data and the FEA is only possible when the bending stiffness of the skin is uniform across its span and strokes of the two sets of actuators spaced at the specified distance are identical. In the present case, the higher absolute values of



(a) Maximum deflections (i) without aero load (ii) with aero load at 10° angle of attack.



(b) Difference between the displacement fields.

Figure 7.3: Results of DIC showing flap deflection.

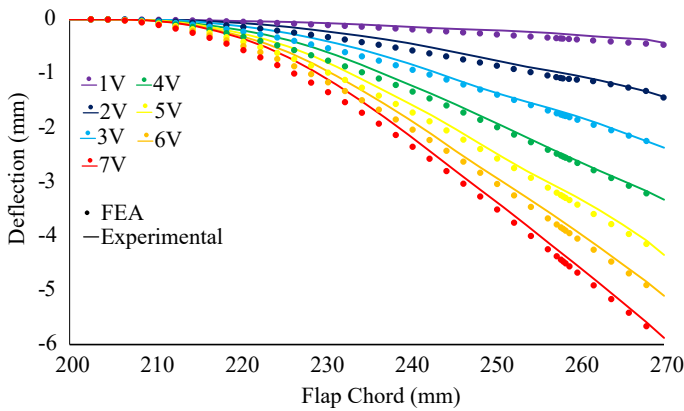
the force obtained from the characteristic equation are a result of a smaller stroke measured by the DT against the applied voltage. The outcome reflects that more energy is consumed by the actuators to morph the top portion of the flap than what is required to morph the bottom portion. A comparison between the FEA and the experimental data is established by evaluating the increase in force. From Tab. 7.1, it can be noticed that the experimental and numerical values show a close match, indicating that the overall numerical analysis predicts the actual behaviour of the skin with a difference of about 10% when the difference in force is observed with and without the aerodynamic loading.

The stroke lengths corresponding to the tip deflections observed experimentally are used in the FEA to generate the morphed shapes and the corresponding point data.

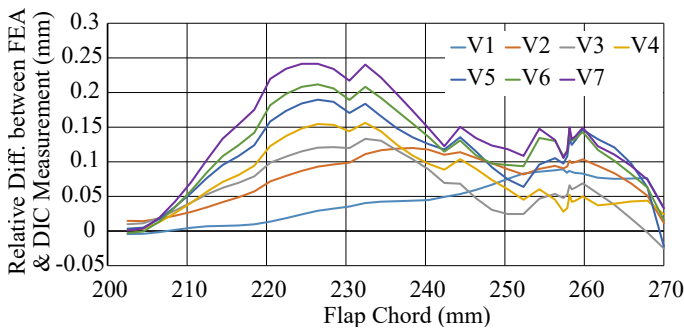
Table 7.1: Validation of aerodynamic analysis.

	Measured Stroke (mm)		Force Exp. (N)		Force FEA (N)
	Bottom	Top	Bottom	Top	-
Without Aero Load	1.74	1.36	20.3	33.7	20.2
With Aero Load	1.70	1.31	21.6	35.3	21.63
Increase in Force (N)			1.3	1.6	1.43

To compare the deformed shapes numerically and experimentally, points are obtained from the DIC analysis approximately at the mid-span of the demonstrator. The corresponding curves obtained using these points are plotted for different supplied voltages, as shown in Fig. 7.4a. The results show that the deformed shapes obtained numerically and experimentally correlate very well, especially near the tip. The difference between the experimental and FEA data is relatively higher for the cases where the magnitude of deflection is high, as shown in Fig. 7.4b.



(a) Comparison of deformed shapes - FEA vs DIC.



(b) Relative difference at various strokes.

Figure 7.4: Comparison of deformed shapes - FEA vs DIC.

7.1.2. DYNAMIC TESTING

The dynamic testing is performed during the wind tunnel test mainly to observe the dynamic behaviour of the actuation system under aerodynamic loads with a longer flap. The flap is actuated at various frequencies, reaching up to a maximum frequency of 7 Hz, which is close to 1/rev for a rotorcraft such as Bo105. The flap is actuated at various magnitudes, each with frequencies of 1, 3, 5 and 7 Hz corresponding to the different AOA. Since the peak to peak voltage range for the actuators lies between -20 V to +150 V, the input signal is generated in the form of a sine wave accordingly. Equation 7.1 shows how the input signal is generated, changing the frequency, amplitude, and voltage offset.

$$V_i = V_s + U \sin(\omega t) \quad (7.1)$$

where V_i is the input voltage signal, V_s is the voltage offset, U is the amplitude and ω is the frequency. Using Eq. 7.1, typical signals corresponding to different voltage amplitudes are shown in Fig. 7.5. The amplitude and voltage offset are set according to the maximum allowable voltage recommended for the actuators.

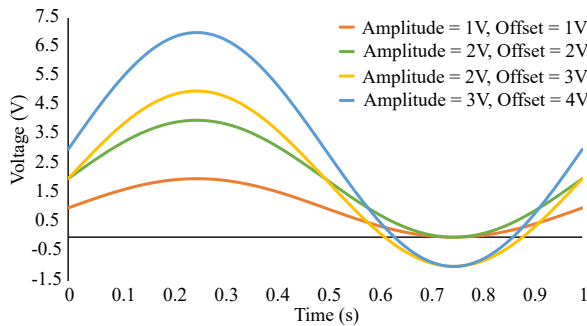
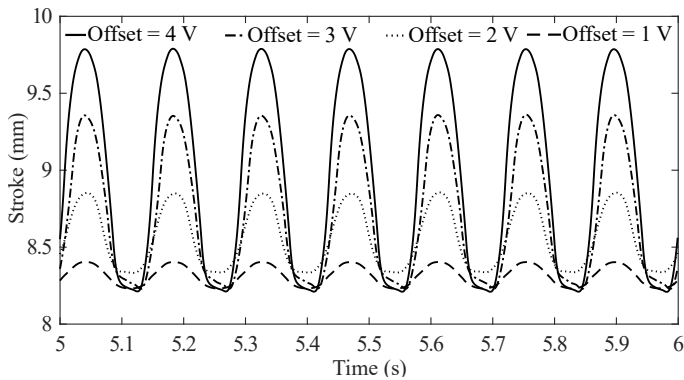


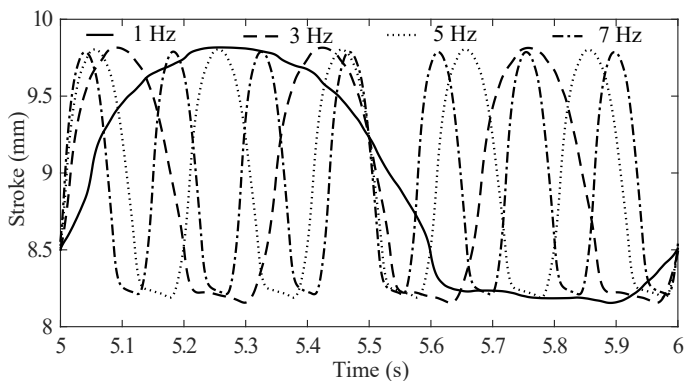
Figure 7.5: Example of input signal at 1 Hz.

Figure 7.6 shows the dynamic response of the top actuator under the maximum aerodynamic loading. Figure 7.6a shows the response of the top actuator when the flap is operated at 7 Hz with different amplitudes. A consistent actuation behaviour is observed at all the amplitudes. The stroke achieved with different voltage amplitudes corresponds to the strokes obtained in the quasi-static tests shown in Fig. 7.2. Fig. 7.6b shows the response of the top actuator at maximum amplitude corresponding to an offset of 4 V and with different operating frequencies ranging from 1 Hz to 7 Hz. It can be seen that there is no reduction in the stroke even if the flap is operated at a frequency of 7 Hz.

Based on the static and dynamic wind tunnel testing, it can be concluded that the amplified piezo actuators can be used to actuate a morphing flap with a span of approximately 1 m. The quasi-static test revealed a difference between the measurements of the two sets of actuators used for the flap deflection. The difference occurred in manufacturing and integration processes. Nevertheless, such a difference can be avoided by using the active system in a closed-loop configuration. In the case of the dynamic testing, the flap actuation is achieved at 7 Hz, which corresponds to 1/rev for the Bo105 helicopter.



(a) Actuator response at 7 Hz with different amplitudes.



(b) Actuator response at different frequencies with maximum amplitude.

Figure 7.6: Dynamic response of the top actuator.

7.2. ACTIVE SYSTEM WHIRL TOWER TESTING

The whirl tower testing of the active morphing system is carried out on the whirl tower setup described in Chap. 6. Since the location of the DT indicated in Fig. 6.6 makes it farthest in the actuation chain, it is used for the correlation with the numerical studies. However, before conducting the testing, a comparison between the response of the strain gauge mounted on the piezoelectric actuator to the DT is carried out. This is important as it serves the purpose of validating the measurements obtained using DT. Figure 7.7 shows the correlation of the two sensors at no load. There is a small variation in the two outcomes mainly because of the difference in types and functionality of the two sensors.

As mentioned in Chap. 4, two blades are used to support the bending of the actuators under centrifugal forces. The ideal case in Fig. 7.8 represents the stroke obtained by using the appropriate values in Eq. 4.1 and compared to the stroke from DT. When the results of the plots in Fig. 7.7 and Fig. 7.8 are compared for the maximum stroke, the force consumed by the blades is estimated to be approximately 4% of the available blocked

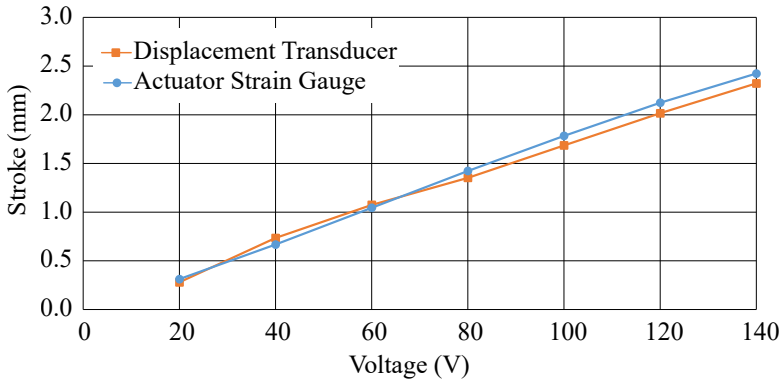


Figure 7.7: Comparison of strokes at no-load.

force as mentioned in Chap. 4. Once the flap is integrated and the actuation mecha-

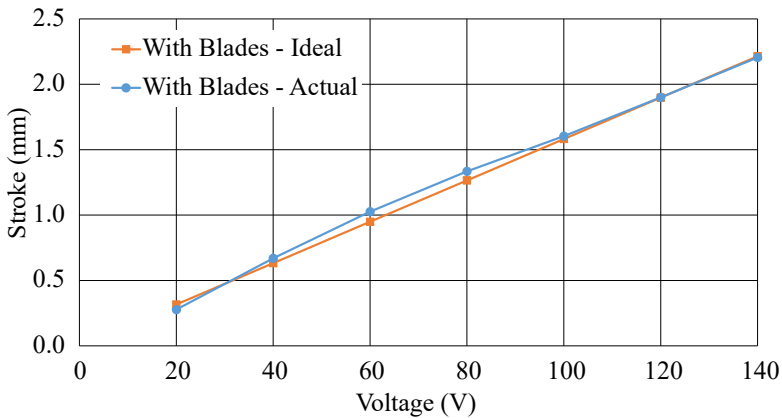


Figure 7.8: Stroke of actuators with blades.

nism is complete, the response of the ideal case and the actual case are compared. For the ideal case (based on Eq. 4.1), the force/stroke is obtained from FEA and turns out to be 6.14 N/mm. The results in Fig. 7.9 show that the response of the DT is approximately linear, and the two curves show a good match. This outcome also emphasizes the importance of flap length with respect to controlling the fabrication and integration processes. A shorter flap length with one set of actuators for the whirl tower test does not indicate the issues encountered by the longer flap for the wind tunnel test with two sets of actuators. Consequently, the correlation between the numerical and experimental results is also improved.

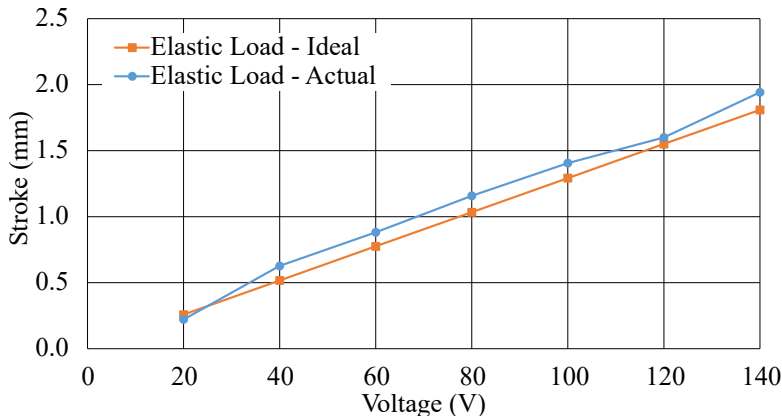


Figure 7.9: Stroke of actuators with flap.

7.2.1. QUASI-STATIC TESTING

During the quasi-static testing, the demonstrator is rotated at a maximum allowable speed of 240 RPM. However, this is done sequentially in four steps starting from 60 RPM and then testing at 120 RPM, 180 RPM, and 240 RPM. The sequential process is adopted to avoid any potential issues with the whirl tower setup. At every RPM, the flap is deflected by varying the voltage applied to the actuators from 20 V to 140 V. At each test point, the data is recorded using the DAQ system, and the tip deflections are recorded using the high-speed camera. A typical signal given to the actuators is shown in Fig. 7.10.

The response of the actuators, in terms of displacement measured by DT, is shown in Fig. 7.11. This response corresponds to the input signals in Fig. 7.10. As indicated, the actuator response is quite consistent in terms of achieving the desired stroke against the applied voltage. Figure 7.12 shows the effect of the RPM on the actuator stroke recorded in Fig. 7.11. The expected stroke based on Fig. 7.9 is also indicated as dashed lines. From Fig. 7.12, it is observed that the maximum degradation in the stroke is only around 3.5% against a centrifugal force of approximately 50 g's experienced by the actuation system. The average degradation in stroke for the applied voltage between 80 V and 140 V is about 2.5% with a standard deviation of 0.94.

The numerical strain on the top skin for the maximum stroke of 2.4 mm is shown in Fig. 7.13. The overall strain levels are quite low, and the strain in the vicinity of the location of the strain gauge is in the range of 600 to 650 microstrain.

The strain due to skin bending is measured by a strain gauge attached to the top skin in the chordwise direction. Figure 7.14 shows the response of the strain gauge at 0 RPM and 240 RPM. It indicates that the strains predicted by the numerical model are quite close to the actual strains measured by the strain gauge. It also indicates that the centrifugal force has no effect on the strain value. The strain gauge bonded on the skin to measure the influence of the spanwise component of the centrifugal force does not present any significant strains indicating that the effect of the centrifugal force is not evident in the morphing skin used in this demonstrator. The strain due to centrifugal

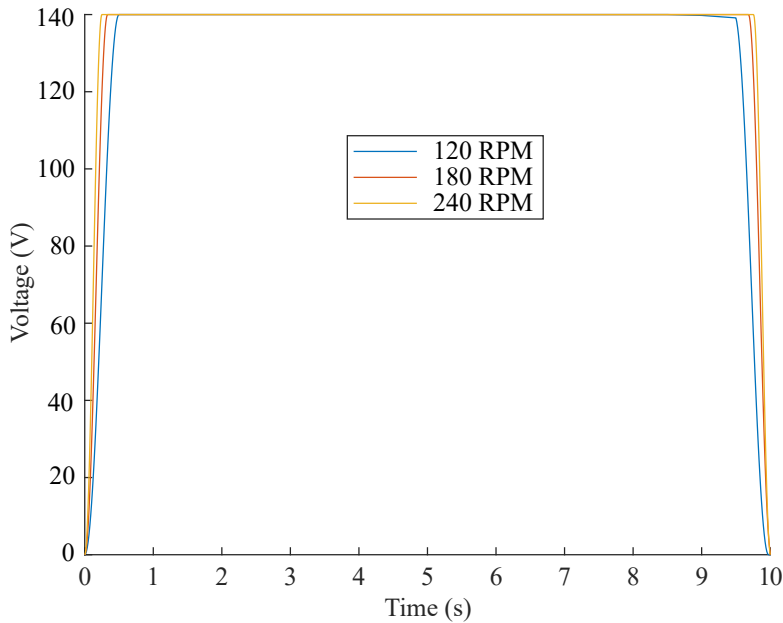


Figure 7.10: Input signal (140 V) at different RPM.

force is not present because the skin is very lightweight, and it is fixed at the top of the aluminium frame.

Throughout the testing, the response of the triaxial accelerometer is monitored, and no significant levels of vibrations are observed [1] as shown in Fig. 7.15 which indicates that the whole test setup is balanced properly. In Fig. 7.15, z-axis considered normal to the ground.

As mentioned earlier, a high-speed camera is used to capture the tip deflections. Figure 7.16 shows two images captured using the high-speed camera at the undeformed position and maximum deflected position when the rotor blade is rotated at 240 RPM.

After post-processing of the images, the tip deflection with respect to the fixed point (FP) indicated in the test setup in Chap. 6 are obtained. Figure 7.17 shows the tip deflection obtained at 240 RPM and compares the results to the tip deflection obtained in FEA. The results show quite a good correlation between the two sets of data points corresponding to various strokes when voltage is varied from 20 V to 140 V.

7.2.2. DYNAMIC TESTING

The purpose of the dynamic testing is to show the consistency of the movement of the actuator and the corresponding flap tip deflection. Keeping in view a maximum RPM of 240 in perspective, the testing is carried out by gradually increasing the RPM from 60 to 240 with an interval of 60 RPM. The actuation frequencies are selected as 1/rev, 2/rev, and 3/rev. Consequently, the flap actuation is carried out for all the selected frequencies at 60, 120, 180 and 240 RPM. Input signals are generated using Eq. 7.1 for frequencies

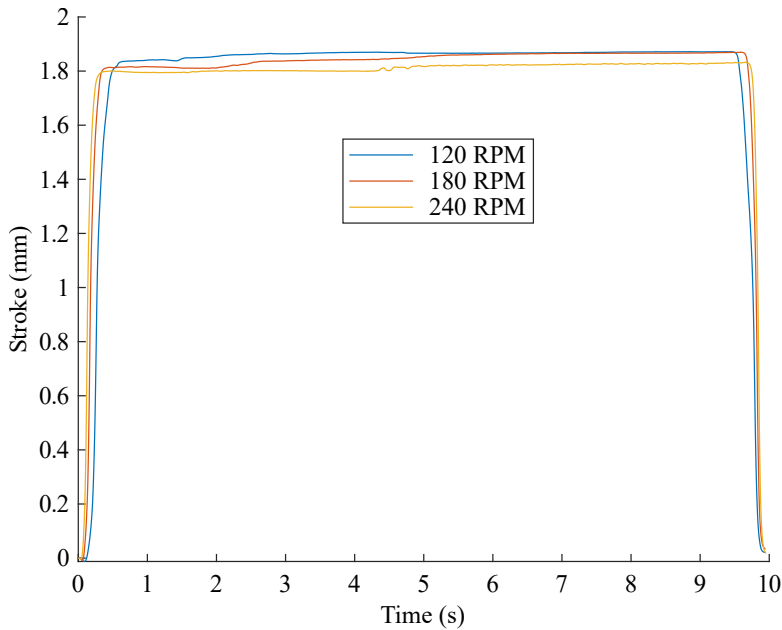


Figure 7.11: Response (140 V) at different RPM.

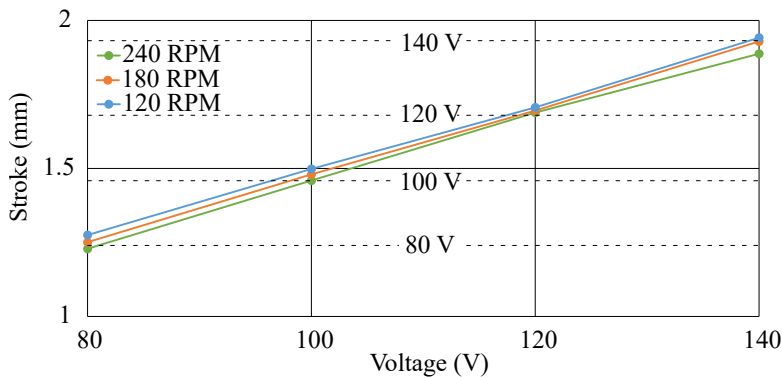


Figure 7.12: Effect of RPM on stroke.

up to 12 Hz, corresponding to 3/rev for a rotational speed of 240 RPM. In addition, the videos are recorded using the high-speed camera to validate the tip deflection during the cyclic operation of the flap.

The response of the actuators is noted by recording the displacement of the DT. Figure 7.18 shows the actuator response at 3 Hz and 6 Hz for a period of 1 s when the blade is rotated at 180 RPM. Similarly, Fig. 7.19 shows the response of the actuators at 240 RPM when the flap is actuated at a frequency of 4 Hz, 8 Hz, and 12 Hz. The input cycle in

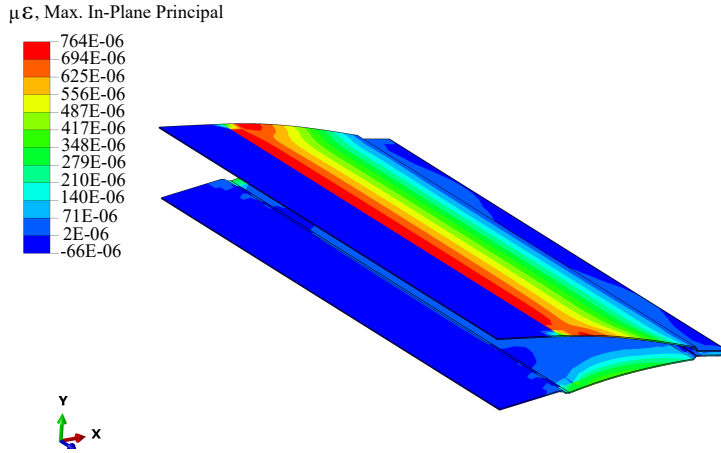


Figure 7.13: Strain in top skin at maximum deflection.

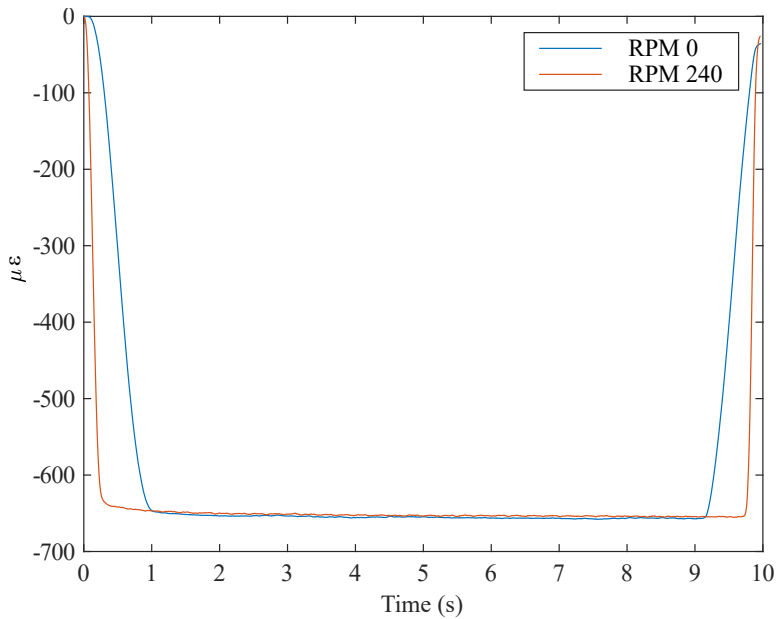


Figure 7.14: Strain top skin at 0 and 240 RPM.

all the aforementioned cases corresponds to an amplitude of 3 V and an offset of 2 V, as shown in Fig. 7.5. The results of actuator stroke indicate that the actuators responded consistently to the input signal under dynamic conditions. More importantly, the results demonstrate that the morphing flap is capable of operating at higher frequencies

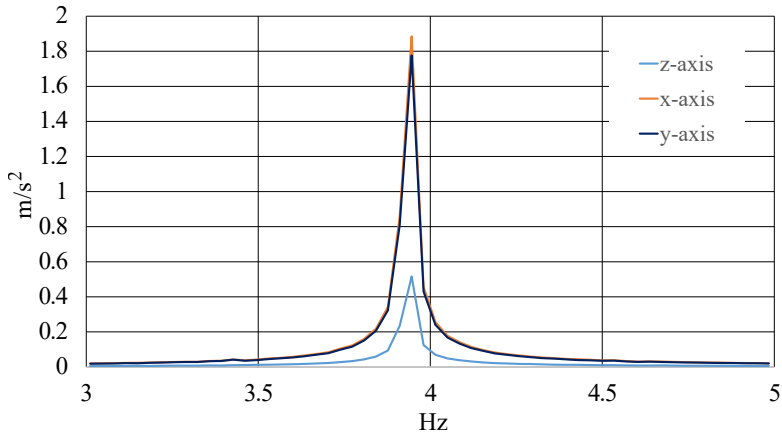


Figure 7.15: Triaxial accelerometer response.

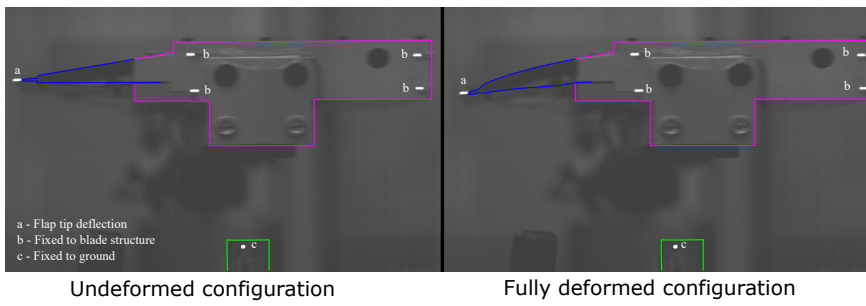


Figure 7.16: Images obtained from high speed camera at 240 RPM.

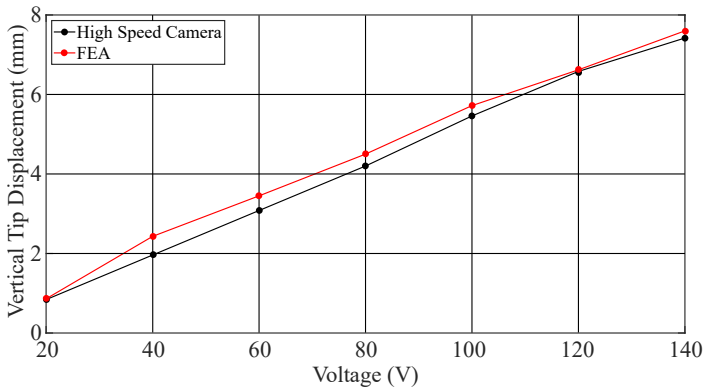


Figure 7.17: Tip deflection comparison at 240 RPM.

repeatedly. Although the testing is not carried out to determine the fatigue life, this encouraging outcome is of extreme importance for the potential applicability of the TRIC morphing concept in a rotorcraft application. Further insight regarding the relationship of the input and output signal can be obtained in future testing by using the input signal as a reference signal in Testlab during the test and obtaining an FRF.

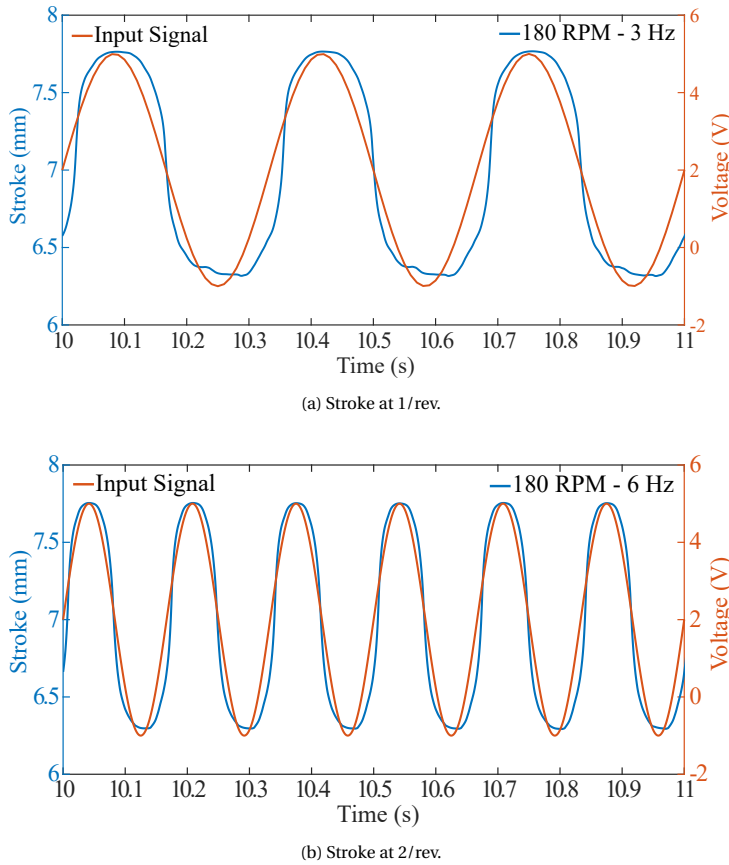
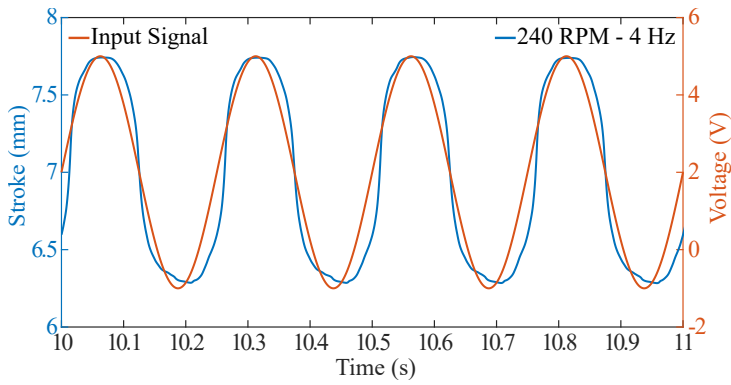


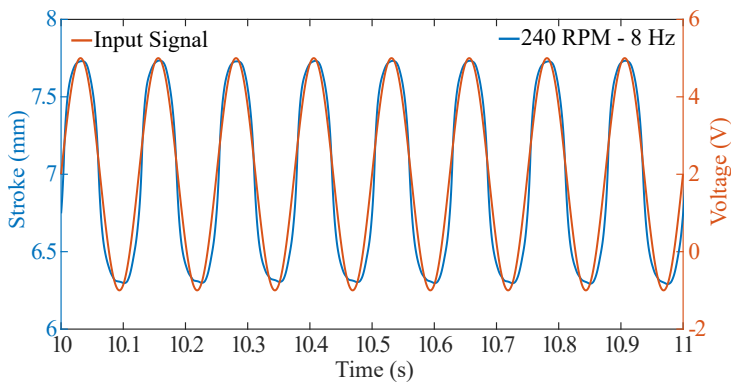
Figure 7.18: Measurement of actuator stroke at 180 RPM.

To validate the flap deflection during dynamic testing, the images are processed from the videos captured using the high-speed camera. Due to the slight difference in the rotational frequency of the demonstrator and the operating frequency of the flap, each revolution (rev) resulted in recording a different tip deflection. It is ensured that at least one cycle is captured during the whole recording phase to capture the flap response. For each case shown in Fig. 7.18 and Fig. 7.19, the corresponding tip deflection is shown in Fig. 7.20 and Fig. 7.21. In addition, the vertical axis in each plot indicates the actual position of the flap from the FP.

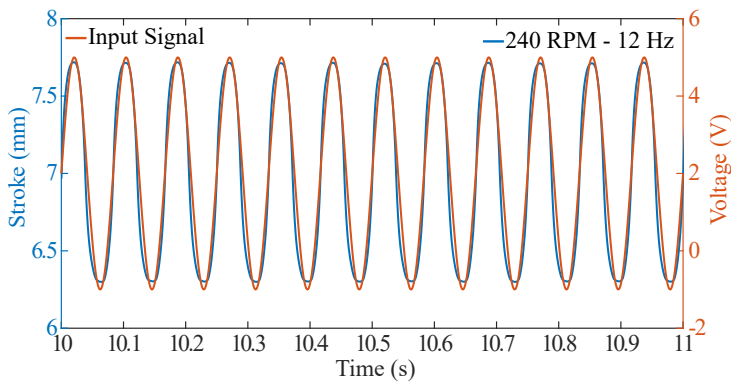
Figure 7.20 and Fig. 7.21 show the data indicating the response of the flap when it is operated at different frequencies and RPM. A summary of the flap deflections obtained



(a) Stroke at 1/rev.



(b) Stroke at 2/rev.



(c) Stroke at 3/rev.

Figure 7.19: Measurement of actuator stroke at 240 RPM.

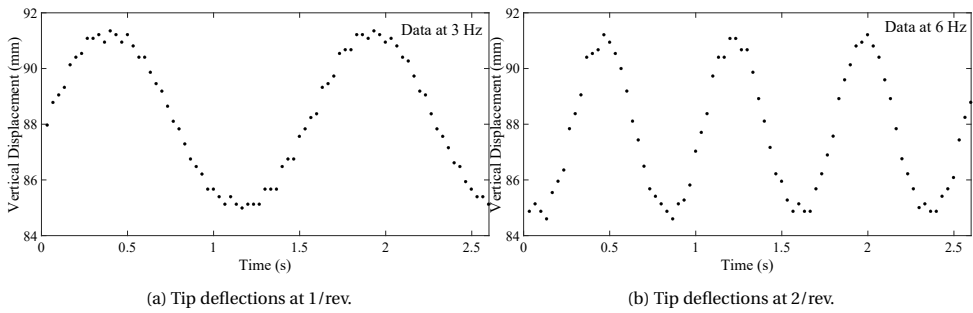


Figure 7.20: Measurement dynamic response through high speed camera at 180 RPM.

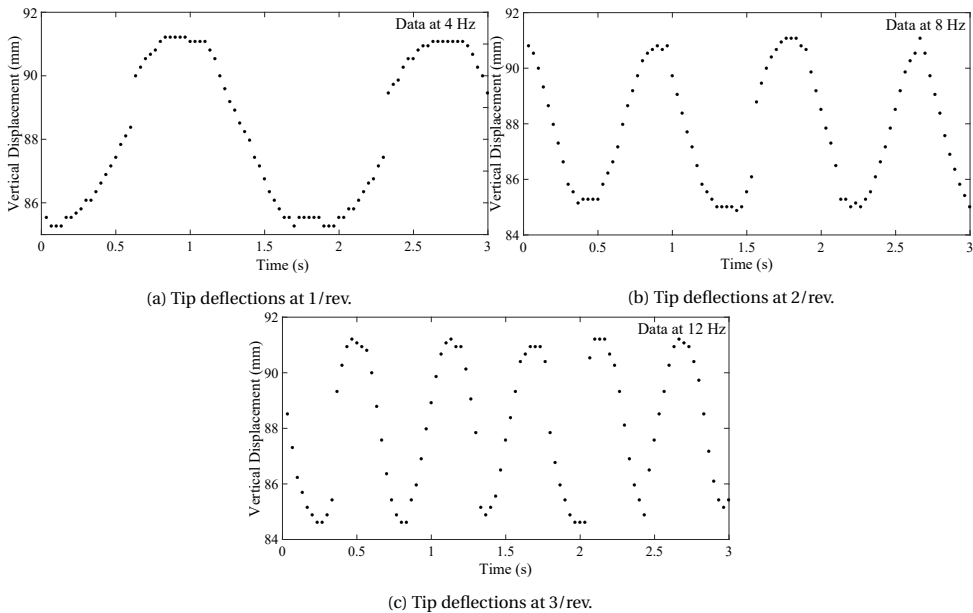


Figure 7.21: Measurement dynamic response through high speed camera at 240 RPM.

from this data is shown in Tab. 7.2. It is evident from Tab. 7.2 that the tip displacement of 6.6 mm observed in Fig. 7.17 for the quasi-static case corresponds to the dynamic case under consideration with a maximum variation of about 7%. This variation mainly results from the freeplay present in the system. The plots can not be directly linked to the actual frequency of the flap because of the way the data is acquired. Nevertheless, it serves to validate the input signal given for the actuation by presenting a shape in the form of a sine wave. The missing points in Fig. 7.20 and Fig. 7.21 represent those frames that missed one or two stationary points and are excluded from the post-processing due to this reason.

Based on the whirl tower testing of the active morphing system, it can be concluded that the active system is able to operate under the influence of the apparent centrifugal

Table 7.2: Summary of flap deflection at 180 and 240 RPM.

Rotor RPM	Flap Frequency	Flap Deflection (mm)
180	1/rev	6.36
180	2/rev	6.61
240	1/rev	6.61
240	2/rev	6.19
240	3/rev	6.12

forces. This is demonstrated using a whirl tower setup that is able to test the active system to a maximum value of 50 g's. One set of APA is used for this system which has a flap span equal to 200 mm. The actuation frequencies achieved during the dynamic testing range from 1/rev to 3/rev. During the quasi-static test and dynamic test, the kinematics of the active system is able to consistently provide the required stroke with minimal degradation. This is validated by acquiring the tip deflections of the flap using a high-speed camera.

7.3. PASSIVE SYSTEM WHIRL TOWER TESTING

The passive morphing experiment is conducted mainly to validate the concept presented in Chap. 5. As mentioned in Chap. 6, five springs are selected based on the maximum allowable RPM permitted on the whirl tower setup. The experiment is conducted with all the springs having some variation in preload and the spring constant K_s . The main objective of this test campaign is to develop an understanding of the behaviour of the passive system and to monitor the spring deflections and the corresponding flap tip deflections. By using different springs in the process, the consistency of the passive system can be demonstrated.

Before using the springs in the passive system, all the springs are tested for the preload and K_s using a tensile test machine. The deflection of each spring against the applied force is shown in Fig. 7.22. From the deflection curves shown in Fig. 7.22, the consolidated data is provided in Tab. 7.3 including the specification of each spring provided by the original equipment manufacturer (OEM).

Table 7.3: Specification of springs.

ID	Mass (g)	Measured		OEM	
		preload (N)	K_s (N/mm)	preload (N)	K_s (N/mm)
T42602D	132.95	20	0.92	22.66	0.82
T32361F	80.97	25	1.1	25.66	1.22
T42361E	65.38	22.7	1.31	22	1.18
T42361F	71.58	18	1.14	22	1.05
T42361G	80.65	10	1.13	22	0.94

It can be observed from Fig. 7.22 that all the springs show a non-linear region till the

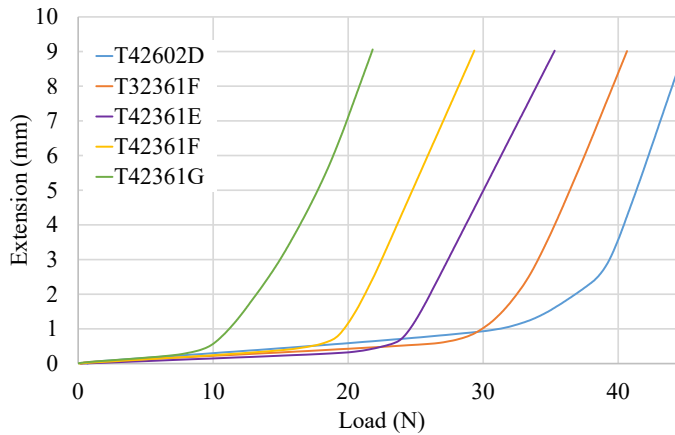


Figure 7.22: Measurement of spring extension for different springs.

spring preload is overcome. This behaviour can be attributed to the deflection of the end loops [2]. The spring exhibits a linear response once the preload is completely overcome.⁹ The spring constants shown in Tab. 7.3 are obtained by taking the linear portion of the curves in Fig. 7.22 between the extensions of 3 mm and 9 mm and then taking the slope of these curves. Figure 7.22 also shows that for all the springs, it is not possible to precisely specify the value of preload. The reason for not having a specific value of preload is because the deflection is not exactly zero for a particular value of force; rather, it has an approximate value of 0.5 mm, after which the linear portion of the curve starts. The measured preload mentioned in Tab. 7.3 is calculated against the deflection of 0.5 mm for all the cases. It must be noted that T42602D shows more non-linear behaviour at the beginning, and the linear part of the curve starts at 2 mm of deflection approximately. The aforementioned discussion concerning the spring data is important as the passive system is also expected to behave in a similar way. For instance, let us consider that two identical springs are selected on the basis of preload and spring stiffness. The first spring shows a higher nonlinearity in terms of its stiffness than the second spring at the beginning of its extension. This would mean achieving the required deflection with the first spring; more force would be required to overcome the spring force. On the other hand, the spring which shows a relatively linear stiffness from the start would attain the desired deflection with a lesser applied force. For a passive system, this means employing a different maximum RPM value in both the aforementioned cases to have a similar flap deflection.

Another critical aspect of passive morphing testing is the amount of friction observed in the manufactured prototype. During the initial bench tests of the setup mentioned in Chap. 6, it is observed that the amount of static and kinetic friction present in the system is so high that no flap movement is observed in the region of interest where the RPM is dropped from 100% to 90% as discussed in Chap. 5. This behaviour is shown in Fig. 7.23 where the loading and unloading cycles are plotted for the case when the system is integrated with T42361E spring, and no mechanical refinement is carried out. The plots

represent the movement of the spanwise shaft against the applied load. The spanwise movement of the shaft is measured by having a displacement transducer (DT) attached underneath in a similar way as in the case of the active morphing system. It can be seen in Fig. 7.23 that even after removing the load below the 90% RPM mark, the applied force exerted by the spring is less than the maximum static force of friction. Similar behaviour is seen at the start of the loading curve, where the onset of deflection is delayed considerably. After observing the issue, considerable effort is put to reduce the excessive amount of friction by using suitable lubricants and adjusting the bearing supports of the two shafts by using very thin shims to improve the shaft alignment. Although the friction is not completely removed from the system in the end, the mechanical refinements improved the functionality of the passive system considerably, as shown in Fig. 7.23. After the mechanical refinements, the unloading cycle caused the flap to deflect downwards within the range of interest, indicating the working of the passive concept.

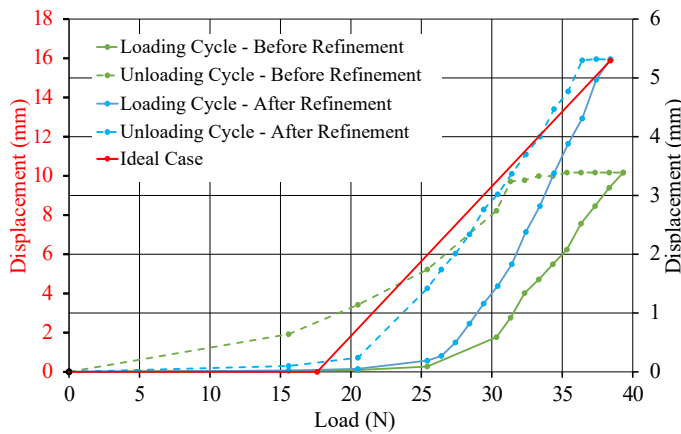


Figure 7.23: Effect of mechanical refinement on kinetic friction.

To demonstrate the role of friction and for the sake of comparison, the ideal response of a passive system is also shown in Fig. 7.23 where the preload of T42361E is considered at zero deflection, and no friction is assumed in the system. Based on the formulations presented in Chap. 5, the ideal response of the system shows considerable deflection of the spring in the region of interest for the same force range as shown in Fig. 7.23. However, it must be noted that practically, the current passive system would behave in a region between the two extremes discussed thus far as neither friction can be ignored in a system nor is it expected to be too high in an industrialized manufacturing scenario. The geometrical discrepancies and shaft misalignment are issues that are expected in a proof-of-concept demonstrator and can be improved in future models.

Before carrying out the experiments of the complete passive system on the whirl tower setup, tests with each spring are performed on the setup with flap disengaged.

The results corresponding to each spring are plotted in Fig. 7.24 and show a similar trend for each spring when compared to the curves in Fig. 7.22. In Fig. 7.24, however, the influence of friction in the system even with a single shaft is prominent in all the cases,

emphasizing the importance of location, alignment, concentricity, surface finish, bearing selection, and geometrical tolerances. All these factors have to be addressed during the future design, manufacturing, and integration of the passive system to improve its performance.

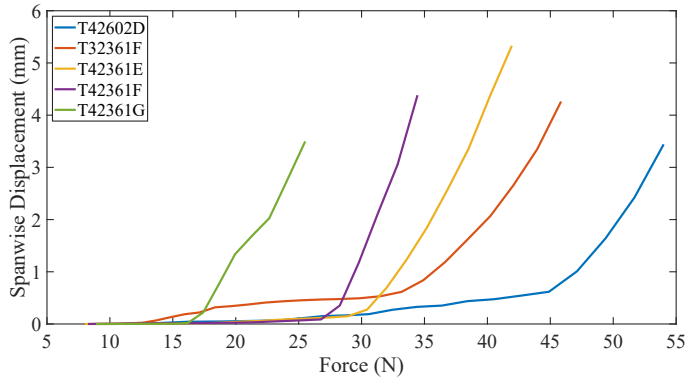


Figure 7.24: Measurement of spanwise displacement without flap under centrifugal load.

With reference to the plots in Fig. 7.24, spring T32361F shows slightly different behaviour at the onset of deflection. This behaviour is attributed to the small freeplay present at the point of connection of the spring and the spanwise shaft Fig. 7.25. The corresponding load extension curve shows a slightly larger offset at the beginning, which is due to the small displacement that occurs between 15 N and 20 N due to the freeplay. Afterwards, the curve is flattened due to the preload of the spring till the point where the spring starts to deflect. This indicates that any freeplay present in the system can affect the behaviour of the passive system.

7

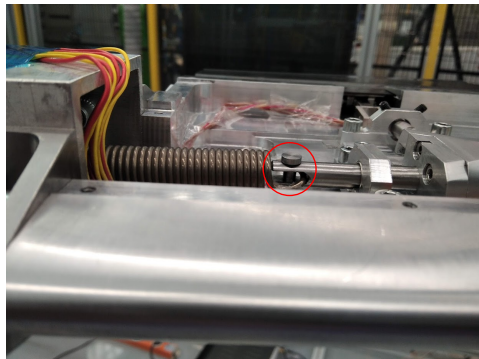


Figure 7.25: Closeup of the freeplay in the spring and connecting pin.

Also, for the case of spring T42602D shown in Fig. 7.24, the system under centrifugal loads shows a similar behaviour as shown in Fig. 7.22. The onset of the linear portion of

the load deflection curve is delayed more due to the higher non-linear region at the start. The relatively linear portion of the loading cycle is observed around 2 mm of deflection.

After doing the initial tests, the complete passive system is tested with all the springs on the whirl tower test setup. The 100% RPM mark is varied based on the preload of each individual spring till a spring extension of approximately 6 mm is achieved for each case. As a sixth case, a small trimming mass is attached in front of the spanwise shaft, and the test is performed with one spring, i.e., T32361F to observe the effect of added mass in the system. Based on the space and attachment constraints, the weight of the resulting mass turned out to be 57 g. Since the whirl tower is operated independently of the data acquisition system, it is not possible to automatically synchronize the spring deflection and the RPM. For this reason, tests are performed initially for all the spring cases, and the region of the desired flap deflection is observed. This resulted in determining the particular RPM value, which brought the springs to their mean positions and enabled establishing the 90% and 100% RPM mark for each case. Afterwards, the data is recorded for this RPM range, where the overall deflection of the spring is captured using the DT, and the tip deflection of the flap is recorded using the high-speed camera.

Figure 7.26 shows the overall response of the system with the first spring T32361F, including the tip deflection. The centrifugal force plotted on the x-axis, corresponds to a particular RPM value, and it is calculated using $F = mr\omega^2$, where m is the total mass of the spring and the shaft, and r is the distance of the centre of gravity of m from the centre of rotation and accounts for the deflection of the spring while calculating the centrifugal force. The value of r is estimated from the CAD model of the passive system for each case. In Fig. 7.26a, the spanwise movement of the system is plotted for the four phases of the movement of the spanwise shaft connected to the extension spring. This division in four phases is important to establish since it is related to the operational scenario of the passive system and serves to show its complete functional cycle. In the first phase (shown as black curve), the RPM is increased from 150 to 240, and the corresponding displacement is recorded at steps of 5 RPM. The increase in RPM is accomplished manually with steps of 1 RPM due to the limitation of the whirl tower setup. In the second phase (shown as dark blue curve), the speed is reduced gradually to 216 RPM, which is the 90% mark. In the third phase, the speed is again increased to 100% RPM (shown as the green curve) and then dropped to 150 RPM (shown as the cyan curve) in the fourth phase. At the beginning and end of each phase, the flap tip deflection is captured using a high-speed camera, giving in total five stages to capture based on the four phases mentioned above. The recorded images are post-processed to show the position of the flap tip with reference to the LED, which is fixed to the ground. The four points attached to the aluminium structure are also plotted for each case to capture any torsional deformations of the demonstrator, as shown in Fig. 7.26b. The vertical axis in Fig. 7.26b shows the position of the flap with respect to the FP for each stage of the operation. The horizontal axis shows the position of the LEDs in the chordwise direction. Similar tests are performed for the remaining springs and shown in Fig. 7.27 to Fig. 7.30.

Due to the difference in specifications, the RPM limits are different for each spring, and thus the operating range is also different. However, having an approximately similar displacement of the spanwise shaft, the data plotted in Fig. 7.26 to Fig. 7.30 gives some important insight into the response of the passive system. From the measurements pre-

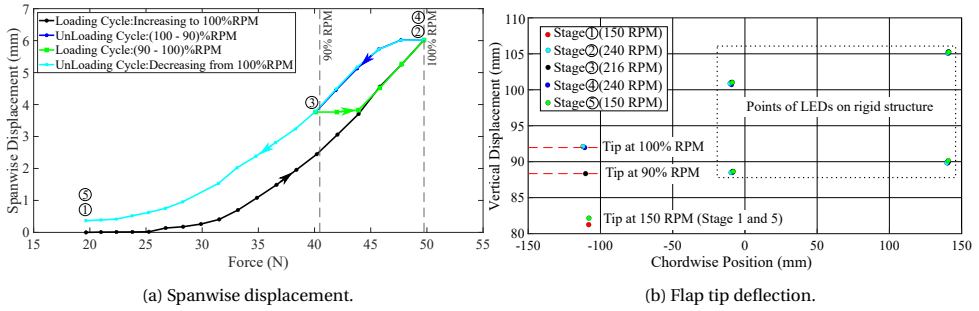


Figure 7.26: Measurements with T32361F with RPM variation from 150 to 240.

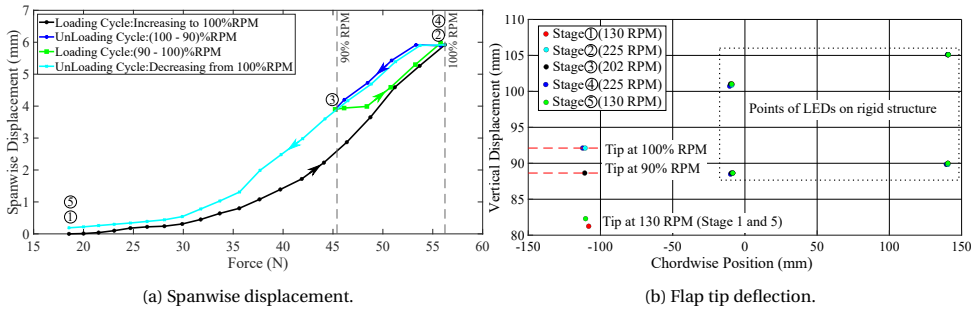


Figure 7.27: Measurements with T42602D with RPM variation from 130 to 225.

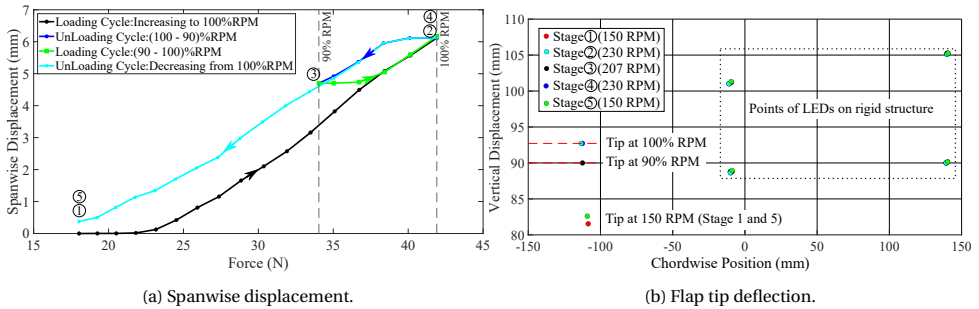


Figure 7.28: Measurements with T42361E with RPM variation from 150 to 230.

sented for each spring, it can be observed that the response of the passive system is directly linked to the preload and stiffness of the individual springs. Furthermore, the available force in the window of operation defined by the 90% RPM and 100% RPM is critical for the desired flap deflection, and it is influenced by the combined mass of the spanwise shaft and the spring. In addition, it can also be observed from the plots that more net force is available to the spring between 90% RPM and 100% RPM window if the maximum value of RPM is higher.

Figure. 7.26a indicates that the spring T32361F, which has the highest value of the

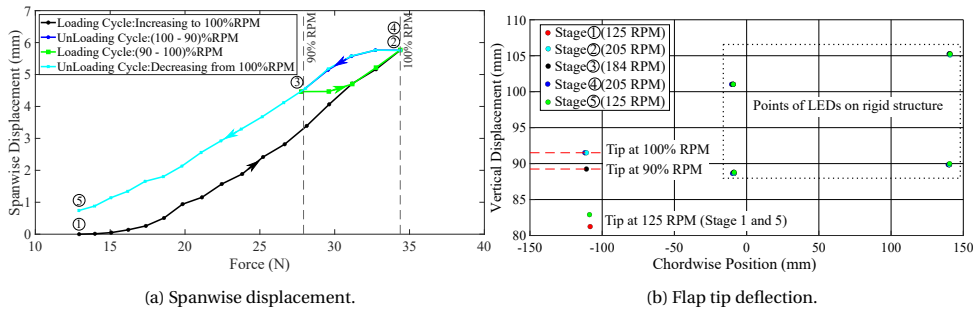


Figure 7.29: Measurements with T42361F with RPM variation from 125 to 205.

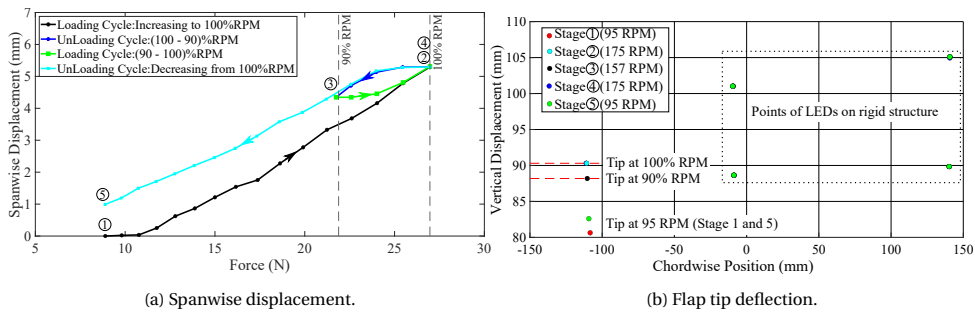


Figure 7.30: Measurements with T42361G with RPM variation from 95 to 175.

preload, shows the highest value of extension in the 90% RPM to 100% RPM range. Consequently the flap tip deflection shown in Fig. 7.26b is also the highest. The delay in the onset of the linear portion of the unloading cycle shown in Fig. 7.26a indicates the amount of static friction present in the system that must be overcome before the movement starts.

In the case of spring T42602D, the maximum value of RPM is observed, which subsequently gives rise to the maximum centrifugal force. The main reason for the higher centrifugal force in the case of spring T42602D observed in Fig. 7.27a is due to the nonlinearity of the spring discussed earlier. Due to the higher stiffness value at the initial stage, more force is required to extend the spring to the desired value, resulting in a higher RPM value in the end. The deflection measured for the spring T42602D is very close to the spring T32361E, as shown in Fig. 7.27b.

For the remaining springs, the response of the system is mainly dictated by the preload as shown in Fig. 7.28, Fig. 7.29 and Fig. 7.30. It can be observed from Fig. 7.30a that spring T42361G has the least amount of net force available within the 10% RPM range to deflect. This is because this particular spring has the lowest preload. Consequently, the amount of tip deflection is also minimum, as shown in Fig. 7.30b. The role of preload is noticeable in all the cases due to the difference in values mentioned in Tab. 7.3. On the contrary, the effect of stiffness cannot be detected in this study due to approximately similar values of stiffness of all the springs.

For the last case, the effect of increasing the weight of the spanwise shaft is estimated by attaching a trimming weight resulting in an increase of 35% in the effective mass. The trimming weight is attached in the form of a rod which is screwed at the end of the spanwise shaft. The corresponding result of the passive system with the new configuration is shown in Fig. 7.31. It can be seen that the RPM for similar deflection is reduced considerably by the addition of the trimming mass. The net force between 90% and 100% for spring T32361F is approximately the same with and without the trimming mass. However, the RPM range for the two cases is considerably different. Due to this reason, reduction in the 100% RPM by 5 RPM accounts for a greater force with the trimming mass than for the same amount of RPM reduction without the trimming mass. The aforementioned trend is noticeable in the unloading curves for both the cases shown in Fig. 7.26a and Fig. 7.31a. Any other conclusion with the additional mass is hard to determine because the difference in the flap deflections is very small between the two cases (0.32 mm), and such a test is performed with only one spring. The tip deflections corresponding to all the cases are shown in Fig. 7.32.

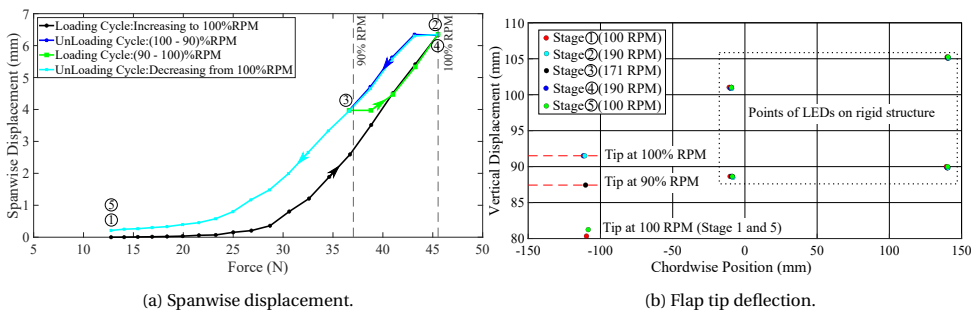


Figure 7.31: Measurements with T32361F & trimming weight and with RPM variation from 100 to 190.

As discussed in Chap. 5, the contribution of the flap is also apparent in all the measurements when compared to Fig. 7.24. This is also important since the aerodynamic loads on the flap are expected to be considerably low because of the size of the flap, the radius of the demonstrator and the maximum allowable RPM. It can be noticed that, effectively, spring preload reduces with the introduction of the flap for all the cases. This indicates that the net force on the flap acts in the direction of the centrifugal force.

From the measurements for each spring, the maximum spanwise displacement is converted to the chordwise displacement by using Eq. 5.18 mentioned in Chap. 5. This chordwise movement is then used in the FEA to note the corresponding tip deflections for each case. The data for the two cases is plotted in Fig. 7.32.

The difference in the two curves is approximately constant and is larger than the active case presented in Fig. 7.17. The reason for the higher difference is due to the fact that more mechanical parts and links are present in the system as compared to the active system, which can potentially reduce the mechanical efficiency of the system. Secondly, the shaft angle φ is taken as precisely 20° for calculating the chordwise movement, and the shafts are assumed completely orthogonal to each other. Any change due to the integration and actual value of φ in the system can affect the chordwise movement resulting

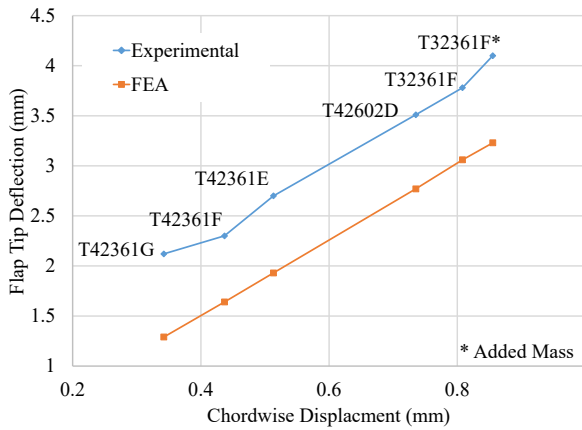


Figure 7.32: Comparison of experimental and numerical tip deflection.

in a different tip deflection. Nevertheless, the test campaign with the passive concept demonstrates the working of the passive morphing concept satisfactorily. The testing has shown that even with manufacturing and integration complexities in the prototype, the demonstrator has shown the operation of the passive concept in the desired range of RPM.

Based on the whirl tower testing of the passive morphing system, it can be concluded that the novel passive system is able to actuate within the prescribed RPM range of 10%. The mechanical efficiency of the system is lower because of the friction observed in the mechanical parts. The experiment is repeated with various springs having different preloads and stiffness values.

7.4. SUMMARY

In this chapter, the results of the experiments are presented related to both the active and passive morphing systems. Three test campaigns are conducted, each with its own test setup and objectives.

The first test campaign was conducted in a low-speed wind tunnel facility to observe the response of the active system by measuring the actuator strokes and the morphed shapes. The test was performed by changing the angle of attack to a maximum value of 10° with the aerodynamic loads corresponding to 15 m/s. The results indicated a good comparison for morphed shapes. The measurements of the actuators at the top and bottom represented deviations due to the non-uniform bending stiffness of the skin potentially caused by the manufacturing issues. In the end, a validation of the FSI scheme was also presented.

In the second test campaign, the active concept was tested in a whirl tower setup, and the system was subjected to a maximum centrifugal load of approximately 50 g's. A high-speed camera was used to capture the tip deflections of the flap both in the quasi-static case and also in the dynamic case. It was shown that the response of the active system

was consistent, and the potential degradation in the actuator stroke was also minimal up to the maximum allowable RPM imposed by the whirl tower setup. The results of the tip deflection and the actuator stroke presented a good correlation with the numerical prediction.

In the final test campaign, the novel passive concept was tested under the centrifugal loads using the same whirl tower setup as that used for the active system. The passive system was tested with the five different springs and a configuration where additional mass is attached to see its effect. Overall, the demonstrator showed that the passive concept operated within the bounds of the 10% RPM set by the operational requirements. The effect of friction was obvious in the demonstrator being the first prototype, due to which the deflections in the region of interest are limited. However, the testing had indicated that the passive system operated under the given operating conditions as conceived.

8

CONCLUSIONS AND RECOMMENDATIONS

It's more fun to arrive at a conclusion than to justify it.

Malcolm Forbes

Before discussing the conclusions, it is important to reemphasize the main objectives of the present work. The present research aimed to design and explore the feasibility of a camber morphing flap for rotorcraft. The design process looked at the possibilities of morphing the trailing edge flap with active means. Moreover, ideas to morph the flap passively by using centrifugal force were also explored. The research focused on the feasibility study of the overall morphing system(s) by developing and testing specific demonstrators. The main research question of the thesis was:

How can an active and passive morphing system be envisaged with a camber morphing technique for rotorcraft blades?

Answers to the following sub-questions were required to answer the global research question mentioned above

- What are the design considerations and requirements for developing a morphing flap and the requisite actuation system?
- How can the feasibility study of active and passive morphing systems be carried out to show the potential of both systems for rotorcraft?

The dissertation discussed two morphing systems based on the (Translation Induced Camber) TRIC morphing concept. The focus of the present work was to use conventional structures and components to achieve morphing capability in rotorcraft and demonstrated the functionality of both concepts by experiments. The active concept utilized piezoelectric actuators for actuation, while the novel passive system operated under the influence of centrifugal forces by varying the rotor revolution per minute (RPM).

The conclusions based on this dissertation are summarized in the following two main sections. In the first section, the observations based on the design, manufacturing, integration, and experiments are summarized in relation to the active and passive morphing systems. In the second section, future developments are proposed for the two systems that can take the present work to the next level.

8.1. CONCLUSIONS

Morphing solutions for aircraft are aimed at increasing the overall performance by providing better flow quality and potentially lesser weight. However, the physical realization and testing of a morphing concept have remained limited, especially for rotorcraft. This is mainly because morphing is generally linked to the development of new materials for flexible skins and actuation methods and fulfilling the requirements of light-weight, strength, and flexibility becomes quite challenging. In this context, the camber morphing technique has shown to be more feasible for morphing, especially when applied to rotorcraft, where the volume available inside the blade structure is minimal because of the small thickness to chord ratio. For this reason, trailing edge morphing flaps have been a popular choice for rotorcraft as the proposed changes are primarily local and do not affect the whole blade structure. The idea of using the TRIC morphing concept for rotorcraft brings the possibility of utilizing conventional materials in the morphing perspective, which can potentially reduce the complexities of a morphing system. However,

the challenge remains to use a proper actuation scheme to provide the required flap deflections at frequencies ranging from 1/rev for primary flight control and from 2/rev to 3/rev and more for noise and vibration mitigation.

The review of state of the art has provided an overview of the earlier work related to the actuation of a morphing system based on the centrifugal forces. Such passive systems have been conceptualized and tested mainly for chord morphing and span morphing. However, the author was unable to find any concept in the past that utilized centrifugal forces for camber morphing. The development of such a morphing system is important as it has shown the potential to increase the performance of a rotorcraft mainly by reducing the collective pitch requirements and increasing the pilot control authority.

8.1.1. MORPHING SKIN

In the present study, a design and analysis approach is presented for the characterization of the morphing skin. The morphing skin design goal includes capturing the skin deformation and estimating the required actuation forces. For this purpose, a Fluid Structure Interaction (FSI) scheme is developed that translates the aerodynamic forces from Computational Fluid Dynamics (CFD) to Finite Element Analysis (FEA). Consequently, the aeroelastic deformations of the TRIC morphing flap are captured accurately by the implementation of this FSI scheme. In addition, it also enables actuator selection by determining the reaction forces at the point of application of force.

In the morphing skin design, the choice of material plays a critical role in saving the weight of the actuation system. It is shown during the present study that composite materials with a carefully selected layup scheme tend to provide more weight savings as compared to isotropic materials such as aluminium. More specifically, a carbon fibre prepreg material like Thinpreg NTPT, which offers thin plies having a thickness of 0.05 mm, is a good choice for a morphing skin as it provides more freedom in terms of the number of plies.

Another factor that influences the required actuation force is the flap chord length. A 25% chord length increases the aerodynamic efficiency and, at the same time, provides enough volume to house the mechanics. In some cases, however, the volume available to house the actuation mechanism can become a deciding factor for the flap chord length as sufficient volume must be available to house the mechanics properly.

8.1.2. ACTIVE CAMBER MORPHING SYSTEM

The challenges in actuator selection for a rotor application increase due to volume constraints, centrifugal forces, and higher frequency requirements. Amplified Piezoelectric Actuators (APA) provides an attractive option for the actuation of control surfaces in rotor blades due to their compact size, rigidity, and relatively high operating frequencies when compared to other off-the-shelf options. The limited stroke length associated with the piezoelectric actuators is compensated to some extent by using APA in series. The proposed actuation system is able to provide sufficient stroke for flap deflections ranging from 5° to 8°.

A wind tunnel experiment is performed in a low-speed open jet wind tunnel with an exit section of 60 cm x 60 cm, having a velocity of 15 m/s. The aims of this test included the measurement of the stroke of the actuators and the tip displacement of the flap at

various aerodynamic conditions. In addition, the deformed shapes of the flap are also recorded. To actuate the flap having a length of 990 mm, two sets of actuators are used and placed farthest apart. When the required actuation forces for the deflection of the flap are measured at these two points, a difference is observed. The main reason for this difference is the warping issue observed during the manufacturing of the skin. In addition, the absence of jigs and fixtures to join the upper and lower halves and to integrate the actuators with the skin contributed to this behaviour. This results in a non-uniform bending stiffness of the skin throughout the span, resulting in different strokes measured by the two sets of actuators placed at a particular distance from each other. It is evident that manufacturing of the skin and integration process can significantly affect the overall stiffness of the end product, especially if the flap requires two actuators to achieve the desired deflection angles. In any case, to achieve a consistent behaviour, these actuators should be used in closed-loop configurations to ensure consistent actuation strokes.

To validate the numerical model, the difference in the required actuation forces obtained from the numerical model and the experiment is also observed. It is shown through the wind tunnel test that the overall FSI scheme works well and predicts the effect of aerodynamic load on the flap actuation force with a difference of 10% compared to the experimental results. Moreover, the deformed shapes obtained using the digital image correlation and finite element analysis also present a close correlation where the maximum deviation between two remains within 0.25 mm throughout the measured range.

The second test is conducted on a whirl tower setup which provides the opportunity to test the demonstrator under a centrifugal force of 50 g's approximately. This test is conducted mainly to observe the response of the actuation system under the influence of centrifugal forces. The actuator stroke and tip deflections are recorded both for the quasi-static testing and also for the dynamic testing, where the flap is actuated at different frequencies corresponding to 1/rev to 3/rev. The results present a good comparison between the numerical study and the experimental campaign and show that the active system with piezoelectric actuators performs as expected under centrifugal forces. The degradation in the stroke is less than 4% for the maximum flap deflection at 240 RPM. The measured strains in the top skin are also observed using a strain gauge and compared to the numerical result. The levels of the strain are found to be relatively low and match the numerical strains. For the dynamic case, the response of the flap at different frequencies is also consistent and shows that the flap provides the required deflection at the desired frequencies. The effectiveness of support blades is prominent, which adds rigidity to the system without a significant penalty in stroke. The results indicate that the TRIC concept initially envisaged for the fixed-wing aircraft has the potential to be used for the rotorcraft applications demanding operating frequencies of 1/rev to 3/rev as shown in the present study. The images captured using a high-speed camera serve as a good validation method to show that the flap actually moves to the required position when operated quasi-statically or dynamically.

8.1.3. PASSIVE CAMBER MORPHING SYSTEM

For a variable speed rotorcraft (VSR), trailing edge camber morphing without an external energy source can potentially increase the overall flight performance. To achieve this, a novel passive system is envisaged for VSR and introduced in this dissertation. The

concept is designed by having an extension spring to store the energy when the RPM is increased to 100% and which is able to release it when the flap is required to deflect downwards by a 10% reduction in RPM. In this context, an analytical tool is developed, which can determine the required spring stiffness and preload. This is achieved by estimating the force required to deflect the flap under the influence of both the elastic force of the flap and hinge moment. For the estimation of the elastic force, it is shown that based on FEA, a simple shape can be used to predict the elastic forces of the flap by utilizing beam theory. However, the difference in actual boundary conditions and the use of composite materials bring additional complexities. To overcome both these issues, it is shown that individual correction factors can be obtained through correlation studies in FEA that can result in reasonable accuracy of the elastic force. Similarly, the aerodynamic loads can also be predicted based on the blade element momentum theory. Consequently, such a tool can quickly predict the required spring stiffness and preload for a given set of requirement specifications. The final selection can be made by doing a high fidelity analysis in which the aerodynamic loads are estimated from CFD.

The role of the net force on the morphing flap is also dominant in the passive system. The net force on the flap takes into account both the elastic load and the aerodynamic loads. It is shown that a component of the net force works in the direction of the applied centrifugal force. This results in effectively reducing the preload of the spring by an amount equal to the component of the elastic force working in the spanwise direction.

The experiments conducted with the passive system indicate that the concept works in the desired RPM range despite excessive friction and offers opportunities for further investigations. The friction in the demonstrator signifies the importance of careful considerations during the design, manufacturing, and integration stages. These considerations include geometrical tolerances, design of jigs and fixtures for manufacturing and integration, selection of proper bearings, surface finish, and choice of lubricants to reduce the amount of friction as much as possible. The importance of these considerations is highlighted during the experiments, where it is noted that friction consumed a significant amount of energy during the operation of the flap.

8.2. RECOMMENDATIONS FOR FUTURE WORK

The active and passive camber morphing systems presented in this dissertation are aimed to improve the flight performance of rotorcraft. The active system has the potential to increase flight quality by operating at frequencies required to mitigate noise and vibration. Furthermore, its applicability for primary control can also be explored. However, in terms of power reduction, overall weight plays a critical role. At present, the electronics (amplifier and strain gauge conditioner) associated with the piezoelectric actuators is heavy and sizeable. To effectively use it in rotorcraft applications, the accompanied electronics should be optimized in terms of weight and size so that the benefits of introducing a morphing flap can be achieved.

Based on the work carried out for active and passive camber morphing, several areas for potential future work are highlighted. The recommended future work can be undertaken to improve the analysis framework for flexible skin. At present, the FSI scheme mentioned in the dissertation takes into account simulations in CFD carried out for specific steady-state shapes generated in FEA. A Matlab code is used to translate the forces

from the CFD to the FEA. This whole process can be automated by bridging the required software and analysis methods, enabling a more robust and efficient method for overall analysis. By adopting this strategy, more cases can be analyzed in a given amount of time. In the end, a summary of morphed shapes in the form of point data, the actuation forces for each load case, and the aerodynamic coefficients including C_l , C_d , and C_m can be obtained. During this process, the possibilities of using a dynamic mesh in CFD can also be explored that can take into account the required morphing shape within the CFD environment. This approach works to avoid re-meshing the computational domain every time the airfoil geometry changes.

During the manufacturing of the flap for the wind tunnel demonstrator, warping of the skin was noted because of the process adopted for the manufacturing of the skins and joining upper and lower halves. The longer length of the flap contributed to the complexities of joining the two halves properly. The issue can be addressed by having proper jigs and fixtures for joining the skins and also for the integration of flap with the actuators.

For the active concept, the signal to the actuators is provided through the data acquisition system, which also gives the option for customization of the input signals. This gives the opportunity to study the frequency response function of the response obtained from the displacement transducer to various input signals. In this way, the actuators can be given different types of input signals with higher frequencies than studied during the present work. The said testing can be performed at the bench level first and later at a whirl tower setup. The resulting measurements can help in better characterization of the whole system and would also establish the operational limits of the APA.

The promising results obtained during the whirl tower test campaign of the active morphing system encourage the design of a Mach-scaled rotor that has a similar actuation system and is subjected to higher centrifugal loads coupled with aerodynamic loads. This is possible with a whirl tower setup that has higher limits of RPM and which also allows the integration of a longer span blade. Such a test would be useful in establishing the performance of the active morphing system in actual flight. In addition, the natural frequency and mode shapes of the system can also be determined during such experiments. This is important as it would help to set the limits on the actuator frequencies keeping in view the rotor blade natural frequency. After proper assessment of control power requirements, it can also be established whether the present concept is more suited for primary control, vibration and noise mitigation, or both. For the assessment of the primary control, a flight dynamics model should be created with a model of the active morphing system.

The novel passive system presented in this dissertation also opens up new avenues for further research. For further understanding of the applicability and limitation of this system, it is highly recommended to use a multibody dynamics tool to model and analyze the motion of the passive system. This would help to predict the effects of different factors such as stiffness, friction, preload, and geometrical inaccuracies on the dynamics of the overall system. In the present work, the stiffness of the springs used for the experiments has relatively similar values while the preload varies. In future experiments, springs with higher variation in preload and stiffness can be used, and the response of the passive system can be investigated. Similarly, the effect of increasing and decreasing

the spanwise shaft mass can also be explored. Another opportunity for characterization of the passive system comes in the form of using a longer flap length. It is pertinent to mention here that a longer flap length can introduce the requirement of connecting the flap at two points of actuation, as in the case of the active system wind tunnel demonstrator. It would be interesting to find a solution that can provide the necessary stroke and rigidity with a single point of actuation for a particular flap length. On the contrary, if two sets of passive actuation systems are used for a single flap, the overall system can become more complex due to the dependence on the centrifugal force for actuation. The two sets shall not be identical if uniform deflection is desired throughout the flap span. However, if the need to twist the flap provides some benefits in performance, the two sets can be made identical by careful considerations of centrifugal force.

In the current passive system, a simple tapered surface of the spanwise shaft is used for the movement of the chordwise shaft resulting in the deflection of the flap. Options of using different shapes of this spanwise shaft at various RPM can be explored in future. In addition, extension springs in the passive system can also be replaced by a compliant mechanism that acts in the same way as a spring but provides an opportunity for a uniform response during the loading and unloading cycle and possibly more control on its design with respect to specific requirements. Such a compliant mechanism would also be an alternative for a friction-free mechanism, avoiding the use of mechanical components like shafts, bearings, and sleeves. Furthermore, this mechanism could be entirely implemented in the flap itself without requiring any space in the main part of the blade structure.

In the end, the passive morphing concept presented in the present research work also gives the opportunity to look at the option of multiple morphing concepts with a single actuation system. As shown in the experiments, the spanwise shaft is extended when the system is at 100% RPM. This gives the possibility of increasing the span of the blade when the RPM reaches the 100% mark, and the flap is deformed to its mean position. If such a requirement is properly assessed and proved advantageous for the rotorcraft operation, two morphing techniques could be coupled with one actuation system.

ACKNOWLEDGEMENTS

Once I completed my Master's from the Aerospace Engineering faculty in 2009, I always wished to come back to the Netherlands and do PhD in the same faculty. I waited long for an opportunity, and when it arrived, it marked the beginning of a fascinating journey. This time, however, I had the company of my wife and my son. Coming to TU Delft once again and accepting a seemingly daunting task would never have been possible unless I had the full and unconditional support of my supervisors, my family, friends, and colleagues in the Netherlands and Pakistan.

To begin with, I would like to thank Dr. Roeland De Breuker for providing me with this opportunity to work on an exciting topic that involved a lot of experimental work. Although I doubted my skills on numerous occasions over the last four years, he never showed a lack of confidence in my capabilities, even once. This was one thing that kept me going even when things started getting hard. His understanding of my job situation in Pakistan with respect to time constraints, offering timely support, giving total freedom to work and opportunities to gain exposure are just a few aspects that made me accomplish my tasks in time. Whenever I look back, I never find an occasion where I looked towards him, and he did not respond positively. It was an honour and a pleasure working with you, sir!.

I am also grateful to Dr. Jurij Sodja and Prof. Mark Voskuijl for continuous support throughout this journey. I am so lucky to have worked and shared the same office with Dr. Jurij Sodja. He has a very methodological and interesting approach to problems, which is always inspiring. His inputs in the experimental work and feedback to improve the dissertation helped to improve the quality of the research outcome. I have learned a lot from him, for which I can't thank him enough. I also always enjoyed his company whenever we travelled together. This provided an opportunity to hear his interesting thoughts on various aspects of life. Similarly, Prof. Mark Voskuijl, although not physically at the faculty, never gave an impression that accessing him or discussing something was an issue. His open-mindedness and pertinent feedback impacted how this dissertation looks at the moment. I always admired him for his polite nature, which made me really comfortable talking to him. His appreciation and encouragement meant a lot to me.

This journey would have been extremely difficult if I had not gotten support from my fellow colleagues and friends. I feel lucky to have enjoyed the office environment before the Covid pandemic. I am really glad that I was able to get valuable inputs and guidance from Paul Lancelot in the first two years. It was really impressive to see his enthusiasm towards aviation and how he was always willing to help and support his colleagues. I always found him available for discussions, and his feedback and inputs had a significant impact on my research work. I would also like to thank my other colleagues including, Hammad, Osama, Tigran, Sherry, Darwin, Javier, Ines, Dr. Humayoun and Sonell, for their help and support whenever I needed it. I would also like to thank and appreciate Ms Laura Chant for guiding, supporting and resolving various non-technical matters during

the four years. In Pakistan, I always turned to Dr. Haroon Awais Baluch for valuable insight on various issues, including technical and non-technical. I am really thankful to him for being an elder brother, a friend and a mentor.

Living abroad and away from one's family is not easy, especially for someone like us, who were used to having huge family support back home. We were lucky to have found friends who always treated us as family members and helped us settle in the Netherlands. Specially thanks to Mr Riasat Gul and his family for all the support, love and help extended at every moment. I would also like to thank Mr Wasim Iqbal and his family for their affection and kindness.

Finally, I would like to thank my entire family for their encouragement, support, and prayers that made this seemingly impossible task achievable. My parents always prayed for me and actually encouraged me to come to the Netherlands to spend four years, knowing the difficulties they would face. My sister and nephew supported this tough decision and stood by my side. My brothers helped me and took care of the family matters in my absence. I am also grateful to my extended family, including my father-in-law, mother-in-law, Meryum, Hifza and Rafay, who provided their wholehearted support and always prayed for my success. I am also thankful to all my friends, relatives, colleagues and well-wishers who I didn't mention specifically but have always supported me and prayed for me.

Last but not least, I would like to thank my lovely wife Momena and my charming son Rayyan who joined me in this journey. I am really impressed by how they adopted the new conditions and culture. My wife took the domestic matters into her hand and worked out of her comfort zone for me to work well. At times, I felt demotivated and weak, but she always provided me strength with her love and support. I am really thankful to Rayyan for making things easier for me and helping me. He adjusted to the new school system and performed very well, for which I really feel proud of him. I can't thank both enough as this dream would not have turned to reality without them.